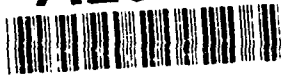


AD-A260 203



AFOSR-TR- 93 0025

2

MODELING OF CLOUD/RADIATION PROCESSES FOR TROPICAL ANVILS

Q. Fu
K.N. Liou
S.K. Krueger

Department of Meteorology/CARSS
University of Utah
Salt Lake City, Utah 84112

DTIC
SELECTE
FEB 03 1993
S B D

Interim Report
1 November 1991 - 31 October 1992

30 November 1992

DISTRIBUTION STATEMENT A
Approved for public release;
Distribution Unlimited

93

93-01982



10808

FEB 1993

MODELING OF CLOUD/RADIATION PROCESSES FOR TROPICAL ANVILS

Q. Fu
K.N. Liou
S.K. Krueger

Department of Meteorology/CARSS
University of Utah
Salt Lake City, Utah 84112

Interim Report
1 November 1991 - 31 October 1992

30 November 1992

NOV 1992

REPORT DOCUMENTATION PAGE

1a. REPORT SECURITY CLASSIFICATION unclassified		1b. RESTRICTIVE MARKINGS	
SECURITY CLASSIFICATION AUTHORITY		3. DISTRIBUTION / AVAILABILITY OF REPORT Approval for public release; distribution unlimited	
2b. DECLASSIFICATION / DOWNGRADING SCHEDULE		5. MONITORING ORGANIZATION REPORT NUMBER(S)	
4. PERFORMING ORGANIZATION REPORT NUMBER(S)		7a. NAME OF MONITORING ORGANIZATION Air Force Office of Scientific Research	
6a. NAME OF PERFORMING ORGANIZATION Center for Atmospheric and Remote Sounding Studies	6b. OFFICE SYMBOL (if applicable) CARSS	7b. ADDRESS (City, State, and ZIP Code) Bolling Air Force Base Washington, D.C. 20332	
6c. ADDRESS (City, State, and ZIP Code) Dept. of Meteorology University of Utah Salt Lake City, Utah 84112		9. PROCUREMENT INSTRUMENT IDENTIFICATION NUMBER AFOSR-91-0039	
8a. NAME OF FUNDING / SPONSORING ORGANIZATION AFOSR	8b. OFFICE SYMBOL (if applicable) NL	10. SOURCE OF FUNDING NUMBERS	
8c. ADDRESS (City, State, and ZIP Code) Building 410 Bolling AFB, DC 20332-6448		PROGRAM ELEMENT NO. 61102F	PROJECT NO. 2310
		TASK NO. CS	WORK UNIT ACCESSION NO.
11. TITLE (Include Security Classification) Modeling of Cloud/Radiation Processes for Tropical Anvils			
12. PERSONAL AUTHOR(S) Q. Fu, K.N. Liou, and S. Krueger			
13a. TYPE OF REPORT Interim Annual	13b. TIME COVERED FROM 11/1/91 TO 10/31/92	14. DATE OF REPORT (Year, Month, Day) 1992 November 30	15. PAGE COUNT
16. SUPPLEMENTARY NOTATION			
17. COSATI CODES		18. SUBJECT TERMS (Continue on reverse if necessary and identify by block number)	
FIELD	GROUP	Radiation Parameterization, Radiative Transfer, Cloud Model, Cumulus Ensemble Model, Cloud Microphysics Parameterization	
	SUB-GROUP		
19. ABSTRACT (Continue on reverse if necessary and identify by block number) This interim report presents some preliminary results simulated from the integration of the radiation parameterization scheme, which has been specifically developed and designed for mesoscale models, and a cumulus ensemble model (CEM). The structure of the CEM, parameterizations of cloud microphysical processes, and parameterizations of scattering and absorption processes and radiative transfer in nonhomogeneous cloud layers are outlined.			
20. DISTRIBUTION / AVAILABILITY OF ABSTRACT <input checked="" type="checkbox"/> UNCLASSIFIED/UNLIMITED <input type="checkbox"/> SAME AS RPT. <input type="checkbox"/> DTIC USERS		21. ABSTRACT SECURITY CLASSIFICATION LU2	
22a. NAME OF RESPONSIBLE INDIVIDUAL Lt. Col. James Stobie		22b. TELEPHONE (Include Area Code) 202-767-5021	22c. OFFICE SYMBOL AFOSR / NL

TABLE OF CONTENTS

	<u>Page</u>
Section 1 INTRODUCTION	1
Section 2 MODEL DESCRIPTION	
2.1 Cumulus Ensemble Model	3
2.2 Microphysical Parameterization	6
2.3 Radiative Transfer Scheme	10
2.3.1 Parameterization of the Single-Scattering Properties of Hydrometeors	10
2.3.2 Parameterization of Nongray Gaseous Absorption	15
2.3.3 Parameterization of Radiative Transfer	17
2.3.4 Comparison with ICRCM Results	17
Section 3 SIMULATION OF TROPICAL CONVECTION	
3.1 Boundary and Initial Conditions	21
3.2 Thermodynamic and Cloud Microphysical Fields	22
3.3 Radiation Budget Diagnosis	31
3.3.1 Heating Rate Fields	33
3.3.2 Cloud Radiative Forcing	36
Section 4 SUMMARY	44
REFERENCES	47
Appendix Parameterization of the radiative properties of cirrus clouds	50

DTIC QUALITY INSPECTED 3

Accession For	
NTIS GRA&I	<input checked="" type="checkbox"/>
DTIC TAB	<input type="checkbox"/>
Unannounced	<input type="checkbox"/>
Justification	
By	
Distribution/	
Availability Codes	
Dist	Avail and/or Special
A-1	

Section 1

INTRODUCTION

Satellite imagery suggests that large portions of the tropics are covered by extensive cirrus cloud systems (Liou, 1986). Tropical cirrus clouds evolve during the life cycle of the mesoscale convective systems and are modulated by large-scale disturbances. Outflow cirrus clouds from tropical cumulonimbi appear to be maintained in a convectively active state by radiative flux gradients within the clouds, as suggested by Danielson (1982). Extensive anvils are likely to become radiatively destabilized by cooling at tops and warming at bases. This would drive convective fluxes which in turn would provide an upward flux of water vapor within the cloud. The additional moisture at cloud top levels would promote rapid ice crystal growth and fallout. Ackerman et al. (1988) have computed radiative heating rates in typical tropical anvils. The heating rate differences between the cloud bottom and top ranges from 30 to 200 K/day. Lilly (1988) has analyzed the dynamic mechanism of the formation of cirrus anvils using a mixed layer model, and has shown that destabilization of the layer could be produced by strong radiative heating gradients. The importance of radiative processes in the life cycle of tropical anvils and convective systems has also been illustrated by Chen and Cotton (1988) and Dudhia (1989).

Clearly, strong radiative heating gradients generated by tropical cirrus anvils would have a significant impact on tropical dynamic and thermodynamic processes on a variety of scales as well as on cloud microphysical processes. Those processes in turn modulate the cloud evolution and the associated radiative heating profiles. Understanding the intricate interactions among radiation, cloud microphysics, and dynamics requires a mesoscale cloud model that includes an interactive radiation code. We are in the process of merging the new and comprehensive radiation parameterization developed by Fu and Liou (1992a,

Appendix), specifically designed for mesoscale models, with the cumulus ensemble model developed by Krueger (1985 and 1988). This report presents some preliminary results from the integration of the radiation and cloud models.

In Section 2, we first briefly describe the cumulus ensemble model (CEM) and the parameterization of three-phase microphysics processes. Next, we outline the parameterizations of scattering and absorption processes involving absorbing gases and particulates and the radiative transfer scheme. In Section 3, we describe the initial and boundary conditions for the CEM and present the microphysical and thermodynamic fields of a squall line system simulated by the CEM. Subsequently, the radiative heating rate fields and cloud radiative forcings associated with this squall line system are presented. Finally, a summary is given in Section 4.

Section 2

MODEL DESCRIPTION

2.1 Cumulus Ensemble Model

A *cumulus ensemble model* (CEM) is a numerical model that covers a large area and at the same time resolves individual cumulus clouds. The CEM differs from the more familiar isolated cloud models in that it can be used to simulate the response of a cumulus ensemble to a prescribed large-scale condition. It can also simulate the mesoscale organization of convection. According to observations (e.g., those made during GATE), a three-dimensional (3D) CEM is required to completely describe the evolution of mesoscale motions as well as the behavior of individual cumulus clouds. Since a tropical anvil cloud associated with a mesoscale convective system may be several hundred kilometers wide and last for several hours, the CEM should cover a region of at least 500 km and should be integrated for more than ten hours to simulate the life cycle of an anvil complex. Because of the computational effort involved, a 3D CEM simulation is not feasible at present, especially when an interactive radiation program is included. For this reason, we shall confine our presentation to a two-dimensional (2D) CEM. Many pioneering studies have demonstrated that a significant physical understanding regarding the mesoscale convective system can be derived from simulations using a 2D CEM model (Lipps and Hemler, 1986; Tao et al. 1987; Rotunno et al. 1988; Krueger, 1988; Xu and Krueger, 1991).

In the present study we use the 2D CEM developed by Krueger (1988). In the following, we present the dynamic structure of the model, which is based on the anelastic set of equations. In Cartesian coordinates for the case of a slab symmetry, the basic equations for momentum, continuity, thermodynamics, and water mixing ratios may be written as follows:

$$\frac{d}{dt}\langle u \rangle = -\frac{\partial}{\partial x}(C_p \theta_{v0} \langle \pi_1 \rangle) - \frac{\partial}{\partial x} \langle u'' u'' \rangle - \frac{1}{\rho_0} \frac{\partial}{\partial z} (\rho_0 \langle u'' w'' \rangle) + f \langle v \rangle, \quad (2.1)$$

$$\frac{d}{dt}\langle v \rangle = -\frac{\partial}{\partial x} \langle u'' v'' \rangle - \frac{1}{\rho_0} \frac{\partial}{\partial z} (\rho_0 \langle v'' w'' \rangle) - f[\langle u \rangle - u_g(z)], \quad (2.2)$$

$$\begin{aligned} \frac{d}{dt}\langle w \rangle = & -\frac{\partial}{\partial z}(C_p \theta_{v0} \langle \pi_1 \rangle) - \frac{\partial}{\partial x} \langle u'' w'' \rangle - \frac{1}{\rho_0} \frac{\partial}{\partial z} (\rho_0 \langle w'' w'' \rangle) \\ & + g \left[\frac{\langle \theta_1 \rangle}{\theta_0} + 0.61 \langle q_{v1} \rangle - \langle q_c \rangle - \langle q_r \rangle - \langle q_i \rangle - \langle q_s \rangle - \langle q_g \rangle \right], \end{aligned} \quad (2.3)$$

$$\frac{\partial}{\partial x} (\rho_0 \langle u \rangle) + \frac{\partial}{\partial z} (\rho_0 \langle w \rangle) = 0, \quad (2.4)$$

$$\frac{d}{dt}\langle \theta \rangle = -\frac{1}{\rho_0} \frac{\partial}{\partial z} (\rho_0 \langle w'' \theta'' \rangle) - \frac{\partial}{\partial x} \langle u'' \theta'' \rangle - \bar{w}(z, t) \frac{\partial}{\partial z} \langle \theta \rangle + S_\theta + R_\theta, \quad (2.5)$$

$$\begin{aligned} \frac{d}{dt}\langle q_{v,c,i} \rangle = & -\frac{1}{\rho_0} \frac{\partial}{\partial z} (\rho_0 \langle w'' q_{v,c,i}'' \rangle) - \frac{\partial}{\partial x} \langle u'' q_{v,c,i}'' \rangle \\ & - \bar{w}(z, t) \frac{\partial}{\partial z} \langle q_{v,c,i} \rangle + S_{v,c,i}, \end{aligned} \quad (2.6)$$

$$\begin{aligned} \frac{d}{dt}\langle q_{r,s,g} \rangle = & -\frac{1}{\rho_0} \frac{\partial}{\partial z} (\rho_0 \langle w'' q_{r,s,g}'' \rangle) - \frac{\partial}{\partial x} \langle u'' q_{r,s,g}'' \rangle \\ & + \frac{1}{\rho_0} \frac{\partial}{\partial z} (\rho_0 v_{r,s,g} \langle q_{r,s,g} \rangle) + S_{r,s,g}, \end{aligned} \quad (2.7)$$

where the potential temperature is given by

$$\theta = T \left(\frac{p_{00}}{p} \right)^{R/C_p},$$

the virtual potential temperature is

$$\theta_v = \theta(1 + 0.61q_v),$$

the dimensionless pressure is

$$\pi = \left(\frac{p}{p_{00}} \right)^{R/C_p},$$

and the hydrostatic equation is

$$\frac{d\pi_0}{dz} = -\frac{g}{C_p \theta_{v0}}$$

In the preceding equations, the angle brackets denote the ensemble mean (equivalent to an average over the y-coordinate); the double primes represent the departure from the ensemble mean; the variables with subscript 0 refer to the reference state, which is hydrostatic and is a function of the height, z, only; the subscript 1 denotes the departure from the reference state; u, v, and w are the three-dimensional velocity components; t is the time; x and z are the horizontal and vertical coordinates; C_p is the specific heat at constant pressure; f is the Coriolis parameter; g is the acceleration of gravity; R is the gas constant for dry air; ρ is the air density; T is the air temperature; p is the pressure; p_{00} is a constant reference pressure; \bar{w} is the prescribed large-scale vertical velocity; u_g is the prescribed geostrophic wind; $q_{v,c,i,r,s,g}$ are the mixing ratios and $S_{v,c,i,r,s,g}$ represent the corresponding sources/sinks due to water phase changes, in which the subscripts v, c, i, r, s, and g denote water vapor, cloud water, cloud ice, rain, snow, and graupel, respectively; S_θ and R_θ represent the sources/sinks of heat due to water phase transitions and radiative processes, respectively, as expressed by changes in potential temperature; and $v_{r,s,g}$ are the mass-weighted mean terminal velocities of rain, snow or graupel (Strivastava, 1967). In the preceding equations, the effect of the large-scale vertical velocity is included only in the equations for potential temperature and suspended water. Although the direct effects of the large-scale vertical velocity on cumulus developments are negligible, it will influence cumulus convection through the temperature and water vapor fields.

Nineteen turbulent flux terms are required to close Eqs. (2.1)-(2.7). The turbulent fluxes for rain, snow, and graupel are set to zero, while $\langle u''v'' \rangle$ and $\langle w''v'' \rangle$ are determined by using the Mellor-Yamada (1974) level one equation as

presented by Xu and Krueger (1991). The remaining turbulent fluxes are predicted using third moment closure (Krueger, 1988). In the turbulence equations, the turbulent fluxes of the mixing ratio of suspended water, $q_w(-q_v + q_c + q_i)$, are calculated; fluxes of the individual components are not required. Similarly, turbulent fluxes of the liquid-ice water static energy, $S_t = C_p T + L_c q_v - L_f q_i - L_c q_c + gz$, where L_c and L_f are the condensation and freezing latent heats, are calculated; fluxes of θ are not required. The third-moment closure has a distinct advantage over simpler closures because it is more general and should therefore have a wider range of validity. In particular, it can be utilized to improve the simulation of boundary-layer turbulence and the treatment of in-cloud turbulence.

2.2 Microphysical Parameterization

The present model utilizes a bulk parameterization to represent cloud microphysical processes, in which the hydrometeors are categorized into five types: cloud droplets, ice crystals, raindrops, snow (or aggregates), and graupel (or hail). The cloud microphysics parameterizations follow the procedures developed by Lin et al. (1983) and Lord et al. (1984) and are briefly described in the following. The microphysics code was provided by Dr. Stephen Lord.

It is convenient to write the source-sink term in Eqs. (2.6) and (2.7) as

$$S_x = C_x + P_x, \quad (2.8)$$

where the subscript x denotes v , c , i , r , s , or g ; C is the source-sink term due to the various possible interactions among water vapor, cloud water, and cloud ice ($C_r = C_s = C_g = 0$); and P is the production terms due to a large number of individual microphysical processes, which are related to precipitating particles and are represented by using bulk parameterizations. These microphysical

Table 1. Microphysical processes represented by bulk parameterizations (after Lord et al., 1984).

Symbol	Meaning
R_{evp}	Evaporation of rain
R_{aut}	Autoconversion (collision-coalescence) of cloud water to form rain
R_{acw}	Accretion of cloud water by rain
R_{acs}	Accretion of snow by rain
S_{sub}	Sublimation of Snow
S_{dep}	Depositional growth of snow
S_{aut}	Autoconversion (aggregation) of cloud ice to form snow
S_{mlt}	Melting of snow
S_{fi}	Transfer rate of cloud ice to snow through depositional growth of Bergeron process embryos
S_{fw}	Transfer rate of cloud water to snow through Bergeron process (deposition and riming)
S_{acw}	Accretion of cloud water by snow
S_{aci}	Accretion of cloud ice by snow
S_{acr}	Accretion of rain by snow
G_{sub}	Sublimation of graupel
G_{aut}	Autoconversion (collision-aggregation) of snow to form graupel
G_{fr}	Probabilistic freezing of rain to form graupel
G_{mlt}	Melting of graupel to form rain
G_{wet}	Wet growth of graupel
G_{acw}	Accretion of cloud water by graupel
G_{aci}	Accretion of cloud ice by graupel
G_{acr}	Accretion of rain by graupel
G_{acs}	Accretion of snow by graupel

processes are described in Table 1. The bulk representation of the individual production terms can be found in Lin et al. (1983). The total production term for six types of water substance may be written as follows:

(i) If the temperature is below 0°C we have

$$P_v = -(1-\delta_1)R_{\text{evp}} - (1-\delta_1)S_{\text{sub}} - \delta_1 S_{\text{dep}} - (1-\delta_1)G_{\text{sub}}, \quad (2.9a)$$

$$P_c = -R_{\text{aut}} - R_{\text{acw}} - S_{\text{fw}} - S_{\text{acw}} - G_{\text{acw}}, \quad (2.9b)$$

$$P_i = -S_{\text{aut}} - S_{\text{fi}} - S_{\text{aci}} - G_{\text{aci}}, \quad (2.9c)$$

$$P_r = (1-\delta_1)R_{\text{evp}} + R_{\text{aut}} + R_{\text{acw}} - S_{\text{acr}} - G_{\text{fr}} - G_{\text{acr}}, \quad (2.9d)$$

$$P_s = -(1-\delta_2)R_{\text{acs}} + \delta_2 S_{\text{acr}} + (1-\delta_1)S_{\text{sub}} + \delta_1 S_{\text{dep}} \\ + S_{\text{aut}} + S_{\text{fw}} + S_{\text{fi}} + S_{\text{acw}} + S_{\text{aci}} - G_{\text{aut}} - G_{\text{acs}}, \quad (2.9e)$$

$$P_g = (1-\delta_2)R_{\text{acs}} + (1-\delta_2)S_{\text{acr}} + G_{\text{aut}} + (1-\delta_1)G_{\text{sub}} + G_{\text{fr}} \\ + \min(G_{\text{wet}}, G_{\text{acw}} + G_{\text{aci}} + G_{\text{acr}} + G_{\text{acs}}). \quad (2.9f)$$

(ii) If the temperature is above 0°C we have

$$P_v = -(1-\delta_1)R_{\text{evp}}, \quad (2.10a)$$

$$P_c = -R_{\text{aut}} - R_{\text{acw}} - S_{\text{acw}} - G_{\text{acw}}, \quad (2.10b)$$

$$P_i = 0, \quad (2.10c)$$

$$P_r = (1-\delta_1)R_{\text{evp}} + R_{\text{aut}} + R_{\text{acw}} + R_{\text{acs}} - S_{\text{mlt}} + S_{\text{acw}} - G_{\text{mlt}} + G_{\text{acw}}, \quad (2.10d)$$

$$P_s = S_{\text{mlt}} - G_{\text{acs}} - R_{\text{acs}}, \quad (2.10e)$$

$$P_g = G_{\text{mlt}} + G_{\text{acs}}. \quad (2.10f)$$

In Eqs. (2.9a) - (2.9f), $\delta_1 = 1$ within cloud ($q_c + q_i > 0$), $\delta_1 = 0$ otherwise; $\delta_2 = 1$ for q_r and $q_s < 0.1$ g/kg, and $\delta_2 = 0$ otherwise. In Eqs. (2.10a) - (2.10f) $\delta_1 = \delta_2 = 0$.

The determination of C terms follows Lord et al. (1984). The following basic assumptions are made. First, all supersaturated vapor condenses/deposits, and is partitioned between cloud water and cloud ice as a linear function of temperature. Second, no ice is produced at $T \geq 0^\circ\text{C}$, while no cloud water is produced for $T \leq -40^\circ\text{C}$, at which homogeneous nucleation is assumed to occur. Third, the saturation water vapor mixing ratio is defined as

$$q^* = \begin{cases} \frac{q_c q_i^* + q_i q_c^*}{q_c + q_i} & \text{for } q_c + q_i > 0 \\ q_i^* & \text{for } q_c = q_i = 0, \end{cases} \quad (2.11)$$

where q_i^* and q_c^* are saturation water vapor mixing ratios with respect to liquid water and ice, respectively. Fourth, the supersaturation is removed at the end of each time step; this is referred to as the saturation adjustment scheme. Fifth, the ice crystal nucleation process, I_{dw} , as described by Lin et al. (1983) is retained as one of the individual microphysical processes to account for the conversion of cloud water to cloud ice through the Bergeron process before the saturation adjustment.

Mass-weighted mean terminal velocities for rain (v_r), snow (v_s), and graupel (v_g) are derived by Lin et al. (1983). Typical values of these velocities are 5, 2, and 10 ms^{-1} for rain, snow, and graupel, respectively. The S_θ term in the thermodynamic equation can be written as

$$S_\theta = P_\theta + C_\theta, \quad (2.12)$$

where P_θ is the potential temperature change due to the microphysical processes listed in Table 1 and C_θ is due to the phase changes among water vapor, cloud droplets, and cloud ice. We have

$$P_\theta = \begin{cases} \frac{1}{C_p} \left[\frac{P_{00}}{P} \right]^\kappa [(1-\delta_1)L_c R_{evp} + L_f(S_{mlt} + G_{mlt} - R_{acs})] & \text{for } T \geq 0^\circ\text{C}, \\ \frac{1}{C_p} \left[\frac{P_{00}}{P} \right]^\kappa \left\{ (1-\delta_1)L_c R_{evp} + L_f(S_{fw} + S_{acw} + S_{acr} + G_{fr} \right. \\ \quad \left. + G_{acw} + G_{acr}) + L_s[(1-\delta_1)S_{sub} + \delta_1 S_{dep} \right. \\ \quad \left. + (1-\delta_1)G_{sub}] \right\} & \text{for } T < 0^\circ\text{C}, \end{cases} \quad (2.13)$$

where $\kappa = R/C_p$, and L_c , L_f , and L_s are the latent heats of condensation, freezing, and sublimation, respectively. C_θ can be expressed as

$$C_{\theta} = \begin{cases} \frac{1}{C_p} \left(\frac{P_{00}}{P} \right)^{\kappa} \frac{L_c \Delta q_c + L_s \Delta q_i}{\Delta t} & \text{for } T \geq 0^{\circ}\text{C} \\ \frac{1}{C_p} \left(\frac{P_{00}}{P} \right)^{\kappa} \left(\frac{L_c \Delta q_c + L_s \Delta q_i}{\Delta t} + L_f I_{dw} \right) & \text{for } T < 0^{\circ}\text{C}, \end{cases} \quad (2.14)$$

where Δq_c and Δq_i are the production of cloud water and ice calculated by the saturation adjustment scheme and Δt the time step.

2.3 Radiative Transfer Scheme

The R_{θ} term in Eq. (2.5) can be written as

$$R_{\theta} = \left(\frac{P_{00}}{P} \right)^{\kappa} \left(\frac{\partial T}{\partial t} \right)_R, \quad (2.15)$$

where $(\partial T/\partial t)_R$ represents the radiative heating rate, which can be computed from

$$\left(\frac{\partial T}{\partial t} \right)_R = -\frac{1}{\rho C_p} \frac{d(F^{\uparrow} - F^{\downarrow})}{dz}, \quad (2.16)$$

with F^{\uparrow} and F^{\downarrow} the net upward and downward fluxes covering both solar and thermal infrared spectra. Radiative fields in the cloud are strongly modulated by the cloud microphysical structure. We have developed a numerically stable and computationally efficient scheme for the calculation of upward and downward fluxes. This radiation scheme is formulated in such a manner that absorption and scattering by both molecules and hydrometeors can be treated consistently.

2.3.1 Parameterization of the Single-Scattering Properties of Hydrometeors

The single-scattering properties, including the extinction coefficient, β , the single scattering albedo, $\bar{\omega}$, and the scattering phase function, $P(\cos\theta)$, must be known before radiative transfer calculations can be performed. The single-scattering properties of hydrometeors are related to the thermodynamic phase (ice or water), shape, and size distribution.

a. *Ice Crystals*

In this study, ice crystals are assumed to be hexagonal columns and plates with length, L , and width, D . To the extent that the scattering of light is proportional to the cross section area of randomly oriented hexagonal ice crystals, we may define a mean effective size to represent ice crystal size distribution, $n(L)$, in the form

$$D_e = \int D \cdot DL n(L) dL / \int DL n(L) dL. \quad (2.17)$$

Based on physical principles, as discussed by Fu and Liou (1992a), the extinction coefficient and single-scattering albedo for ice crystals can be parameterized by the following:

$$\beta = \text{IWC} \sum_{n=0}^2 a_n / D_e^n, \quad (2.18)$$

$$\bar{\omega} = \sum_{n=0}^3 b_n D_e^n, \quad (2.19)$$

where IWC is the ice water content, and a_n and b_n are certain coefficients. The phase function is usually expanded in terms of Legendre polynomials P_l in the form $P(\cos\theta) = \sum_{l=0}^M \bar{\omega}_l P_l(\cos\theta)$, where the expansion coefficients, $\bar{\omega}_l$, can be expressed by

$$\bar{\omega}_l = \begin{cases} (1-f_\delta)\bar{\omega}_l^* + f_\delta(2l+1) & \text{for solar} \\ (2l+1)g^l & \text{for IR,} \end{cases} \quad (2.20)$$

where $\bar{\omega}_l^*$ represent the expansion coefficients without the incorporation of the δ -function transmission through parallel planes at $\theta = 0$ (Takano and Liou, 1989), f_δ denotes the forward contribution due to the δ -function transmission, and g is the asymmetry factor. $\bar{\omega}_l^*$, f_δ , and g can be parameterized by

Table 2. Characteristics of the 11 ice crystal size distributions.

Particle Size Distribution	Ice Water Content (g m ⁻³)	Mean Effective Size (μm)
Cs*	4.765 e-3	41.5
Ci* Uncinus	1.116 e-1	123.6
Ci** (cold)	1.110 e-3	23.9
Ci** (warm)	9.240 e-3	47.6
Ci** (T=-20°C)	8.613 e-3	57.9
Ci** (T=-40°C)	9.177 e-3	64.1
Ci** (T=-60°C)	6.598 e-4	30.4
Ci*** (Oct. 22)	1.609 e-2	104.1
Ci*** (Oct. 25)	2.923 e-2	110.4
Ci*** (Nov. 1)	4.968 e-3	75.1
Ci*** (Nov. 2)	1.406 e-2	93.0

*Heymsfield (1975); **Heymsfield and Platt (1984); ***FIRE (1986).

$$\bar{\omega}_t^* = \sum_{n=0}^3 c_{n,t} D_e^n, \quad f_\delta = \sum_{n=0}^3 d_n D_e^n, \quad (2.21)$$

$$g(\text{IR}) = \sum_{n=0}^3 c'_n D_e^n, \quad (2.22)$$

where $c_{n,t}$, d_n , and c'_n are certain coefficients. In the thermal infrared wavelengths, it suffices to use the asymmetry factor via the Henyey-Greenstein function to represent the phase function because the halo and δ -transmission peak features in the $P(\cos\theta)$ are largely suppressed due to strong absorption.

The extinction coefficient, single-scattering albedo, and expansion coefficients of the phase function for the 11 observed ice crystal size distributions (Table 2) have been computed from a geometric ray-tracing method for hexagonal ice crystals (size parameter > 30) and from a Mie-type solution for spheroids (size parameter < 30). The coefficients, a_n , b_n , c'_n , $c_{n,t}$ and d_n are obtained by numerical fitting to the data computed from the "exact" computations.

Table 3. Characteristics of the eight droplet size distributions.

Cloud Type*	Liquid Water Content (g m^{-3})	Mean Effective Radius (μm)
St I	0.22	5.89
St II	0.05	4.18
Sc I	0.14	5.36
Sc II	0.47	9.84
Ns	0.50	9.27
As	0.28	6.16
Cu	1.00	12.10
Cb	2.50	31.23

*Stephens (1978)

The preceding parameterizations have relative accuracies within $\pm 1\%$.

For radiative transfer calculations, nonspherical ice crystals have been frequently approximated by ice spheres with equivalent areas (see e.g. Stackhouse and Stephens, 1991). Equivalent-area spheres scatter more light in forward directions and have smaller single-scattering albedos than nonspherical ice crystals. As a result, the assumption that ice crystals are spheres leads to a significant underestimation for the solar albedo of cirrus clouds. As shown by Fu and Liou (1992a), the present parameterization can be used to reasonably interpret the observed IR emissivities and solar albedo involving ice clouds.

b. *Water Droplets*

For water clouds, we may define a mean effective radius, r_e , to represent the water droplet size distribution, $n(r)$, with respect to radiative calculations as follows:

$$r_e = \frac{\int r^3 n(r) dr}{\int r^2 n(r) dr}. \quad (2.23)$$

The single-scattering properties of water droplets can be calculated exactly by using the Mie theory. Eight water cloud types presented by Stephens (1978) are used in the present study and are listed in Table 3. By using the single-scattering properties of the eight water clouds, the following parameterizations have been developed (Fu, 1991):

$$\beta = \text{LWC} \left[\frac{\beta_1}{\text{LWC}_1} + \frac{\beta_2/\text{LWC}_2 - \beta_1/\text{LWC}_1}{1/r_{e2} - 1/r_{e1}} \times \left(\frac{1}{r_e} - \frac{1}{r_{e1}} \right) \right], \quad (2.24)$$

$$\bar{\omega} = \bar{\omega}_1 + \frac{\bar{\omega}_2 - \bar{\omega}_1}{r_{e2} - r_{e1}} (r_e - r_{e1}), \quad (2.25)$$

$$g = g_1 + \frac{g_2 - g_1}{r_{e2} - r_{e1}} (r_e - r_{e1}), \quad (2.26)$$

where LWC is the liquid water content. The terms $(\beta_1, \bar{\omega}_1, g_1)$ and $(\beta_2, \bar{\omega}_2, g_2)$ denote the single-scattering properties for two cloud types listed in Table 3 with (LWC_1, r_{e1}) and (LWC_2, r_{e2}) , respectively, so that r_{e1} and r_{e2} are the pair of mean effective radii closest to r_e and $r_{e1} \leq r_e < r_{e2}$. The scattering phase functions for water clouds are approximated by the Henyey-Greenstein function through the asymmetry factor.

c. Raindrops, Snow, and Graupel

The size distributions for these hydrometeors used in the bulk parameterization are in the forms

$$n_x(D) = n_{0x} \exp(-\lambda_x D_x), \quad (2.27)$$

where the subscript x denotes r , s , or g ; n_0 is the intercept parameter; λ is the slope parameter; and D is the diameter of the hydrometeors. The intercept parameters, as given by Lord et al. (1984), are $n_{0r} = 0.22$, $n_{0s} = 0.03$, and $n_{0g} = 4 \times 10^{-4} \text{cm}^{-4}$. The slope parameter is given by

$$\lambda_x = \left(\frac{\pi \rho_x n_{0x}}{\rho q_x} \right)^{0.25},$$

where $\rho_r = 1$, $\rho_s = 0.1$, and $\rho_g = 0.3$ g/cm³; and ρq_x is the rain, snow, or graupel water content (g/cm³). Setting $\rho q_x = 0.5 \times 10^{-6}$ g/cm³, we have $\lambda_r = 34.3$, $\lambda_s = 11.7$, and $\lambda_g = 5.24$ cm⁻¹. The corresponding mean effective radii from Eq. (2.27) are 0.044, 0.128, and 0.286 cm for rain, snow, and graupel, respectively. These mean effective radii are determined from

$$r_e = \frac{3}{2\lambda}.$$

The single-scattering properties β'_x , $\tilde{\omega}'_x$ and g'_x for rain, snow, and graupel with the size distributions defined in Eq. (2.27) for the given λ_x above are calculated by the Mie theory. For a water content, ρq_x , from the cloud model, we have

$$\beta_r = \frac{\rho q_r \lambda_r}{1.72 \times 10^{-5}} \beta'_r, \quad (2.28)$$

$$\beta_s = \frac{\rho q_s \lambda_s}{0.585 \times 10^{-5}} \beta'_s, \quad (2.29)$$

$$\beta_g = \frac{\rho q_g \lambda_g}{0.262 \times 10^{-5}} \beta'_g, \quad (2.30)$$

where ρq_x and λ_x are in units of g cm⁻³ and cm⁻¹, respectively. The single-scattering albedo and asymmetry factor are assumed to be equal to $\tilde{\omega}'$ and g' computed from Mie calculations regardless of the size distribution dependence.

2.3.2 Parameterization of Nongray Gaseous Absorption

The solar and thermal infrared spectra are divided into a number of bands depicted in Table 4. Mean values for the scattering properties of hydrometeors,

Table 4. Spectral division used in the parameterization.

Solar Spectrum			Infrared Spectrum		
Band (i)	Central λ (μm)	Band Limit (μm)	Band (i)	Central λ (μm)	Band Limit (cm^{-1})
1	0.55	0.2-0.7	7	4.9	2200-1900
2	1.0	0.7-1.3	8	5.6	1900-1700
3	1.6	1.3-1.9	9	6.5	1700-1400
4	2.2	1.9-2.5	10	7.6	1400-1250
5	3.0	2.5-3.5	11	8.5	1250-1100
6	3.7	3.5-4.0	12	9.6	1100-980
			13	11.3	980-800
			14	13.7	800-670
			15	16.6	670-540
			16	21.5	540-400
			17	30.0	400-280
			18	70.0	280-10

solar irradiances, and Planck functions are used in each band. In the solar spectrum, absorption due to H_2O (2500-14500 cm^{-1}), O_3 (in the ultraviolet and visible), CO_2 (2850-5250 cm^{-1}), and O_2 (A, B, and γ bands) is accounted for in the radiation scheme. In the infrared spectrum, we include the major absorption bands of H_2O (0-2200 cm^{-1}), CO_2 (540-800 cm^{-1}), O_3 (980-1100 cm^{-1}), CH_4 (1100-1400 cm^{-1}), and N_2O (1100-1400 cm^{-1}). The continuum absorption of H_2O is incorporated in the spectral region 280-1250 cm^{-1} .

Nongray gaseous absorption is parameterized based on the correlated k-distribution method developed by Fu and Liou (1992b). In this method, the cumulative probability, g , of the absorption coefficient, k_ν , in a spectral interval, $\Delta\nu$, is used to replace the frequency, ν , as an independent variable. This leads to an immense numerical simplification, in which about ten thousand frequency intervals can be replaced by a few g intervals. Using a minimum number of g intervals to represent the gaseous absorption and to treat overlap within

each spectral interval, 121 spectral calculations are required for each vertical profile. Compared with results from a LBL program, the parameterizations achieve an accuracy within 0.1 k/day for heating rates and 0.5% for fluxes.

2.3.3 Parameterization of Radiative Transfer

For parameterizations of radiative fluxes, we use the δ -four-stream approximation developed by Liou et al. (1988). For a homogeneous layer, an analytic solution can be derived explicitly for this approximation so that the computer time involved is minimal. In order to apply this approach to the thermal infrared radiative transfer, the Planck function is expressed in terms of optical depth, τ , in the form $a \cdot \exp(b\tau)$, where a and b are coefficients determined from the top- and bottom-layer temperatures. Since the direct solar radiation source also has exponential function form in terms of optical depth, the solution of the δ -four-stream approximation for IR wavelengths is the same as that for solar wavelengths. For application to a nonhomogeneous atmosphere we divide this atmosphere into N layers within which the δ -four-stream scheme can be applied. The unknown coefficients in the analytic solution for the radiative transfer equation are determined following the procedure described in Liou (1975). The total single-scattering properties due to the combined contributions of Rayleigh scattering, nongray gaseous absorption, and scattering and absorption by hydrometeors can be evaluated following the procedures described by Fu and Liou (1992a).

2.3.4 Comparison with ICRCCM Results

Results computed from the present radiation scheme are compared with those presented from the Intercomparison of Radiation Codes in Climate Models (ICRCCM) program for cloudy conditions. In the ICRCCM, six sets of radiation calculations

Table 5. Statistics* on the downward IR surface flux calculations under overcast cloudy conditions. Results computed from the present radiation scheme are depicted in the parentheses.

Cloud Type	Top Height (km)	LWP (g m^{-2})	Number of Model	Median $F_{\text{surface}}^{\downarrow}$ (W m^{-2})	Range (%)	rms Diff. (%)
CS	2	10	10	399 (395)	7.0	2.1
CL	2	10	7	387 (368)	9.0	2.9
CL	2	200	14	413 (411)	1.9	0.6
CS	13	10	11	360 (361)	6.4	1.9
CL	13	10	6	358 (353)	5.6	2.0
CL	13	200	13	361 (362)	6.7	2.0

*After Ellingson and Fouquart (1990).

were performed for overcast conditions with the aim of testing the sensitivity of the radiation program to the drop size distribution, the location of the cloud top, and the cloud LWC. The cloud thickness was assumed to be 1 km, with the cloud tops set at 2 and 13 km for low and high clouds, respectively. Two droplet size distributions were selected; one with small droplets (CS, $r_0 = 5.36 \mu\text{m}$), while the other with large droplets (CL, $r_0 = 31.23 \mu\text{m}$). The LWC was specified to be either 10 g m^{-2} (nonblack clouds for both CS and CL) or 200 gm^{-2} (near-black clouds for CL). The calculations were performed with one cloud layer present in a midlatitude atmosphere. For solar radiation computations, the solar zenith angle and the surface albedo are set at 30° and 0.2, respectively.

Table 5 presents the statistics determined from the ICRCM for downward IR surface fluxes. Results from the present radiation scheme are included in the

parentheses. For atmospheres containing near-black clouds, the fluxes computed from the present scheme agree with the median values provided by the ICRCCM within 2 W/m^2 . The present results also agree well with those of ICRCCM in the case of CS. Differences of up to 19 W/m^2 in the surface flux are seen for the case of CL with IWP of 10 g m^{-2} and cloud top of 2 km. The downward surface flux from the ICRCCM is not sensitive to r_0 , because some models have not explicitly considered the dependence of the cloud radiative properties on r_0 (see, e.g. Liou and Wittman, 1979; Stephens, 1978).

Table 6 shows the results for solar radiation. The rms differences and total ranges from ICRCCM are quite large, indicating the difficulty of adequately modeling the effects of multiple scattering. Differences between the present results and the medians from ICRCCM are much smaller than the rms differences, especially for total atmospheric absorption.

Table 6. Statistical results* of the ICRCCM test cases performed for solar radiation in cloudy conditions. The solar zenith angle is 30° and surface albedo is 0.2. The results from the present radiation scheme are depicted in parentheses.

Case	Cloud Type	Top Height (km)	LWP (gm ⁻²)	No. of Models	Downward Flux at the Surface			Total Atmospheric Absorption		
					Median (Wm ⁻²)	Range (%)	rms Diff. (%)	Median (Wm ⁻²)	Range (%)	rms Diff. (%)
43	CS	13	10	17	778.8 (757.2)	15	4	203.4 (197.0)	37	10
45	CS	2	10	16	782.3 (758.6)	15	4	226.7 (230.7)	24	7
46	CL	13	10	14	919.5 (906.3)	8	2	207.6 (215.3)	18	6
47	CL	13	200	15	536.0 (515.9)	38	10	218.5 (234.0)	54	17
48	CL	2	10	15	921.2 (906.3)	8	2	210.8 (218.5)	19	6
49	CL	2	200	15	537.1 (516.1)	43	9	255.5 (287.1)	35	9

*After Fouquart et al. (1991).

Section 3

SIMULATION OF TROPICAL CONVECTION

3.1 Boundary and Initial Conditions

In the CEM simulation analyzed here, we use a horizontal domain of 1024 km and a horizontal grid size of 2 km. The vertical domain used is 19 km with a stretched grid consisting of 33 layers. Near the surface, the grid interval is 100 m, while it is 1 km near the model top. The lateral boundary condition is cyclic and the upper and lower boundaries are rigid. Numerical simulations are carried out over the ocean. The sea surface temperature is fixed at 299.9 K. All surface turbulent fluxes are diagnosed by using the flux-profile relationships given by Deardorff (1972).

In Eqs. (2.5) and (2.6), the terms that include the large-scale vertical velocity are prescribed. These terms are horizontally uniform. They vary with height and time according to

$$f(z,t) = f(z)[1 + \cos(2\pi t/T)]/2,$$

where T (≈ 27 h) is the period, and $f(z)$, representing typical GATE phase-III mean profiles, is described in Xu et al. (1992). The time-independent x-component of the geostrophic wind is prescribed; it is identical to that used by Xu and Krueger (1991) with shear. The sheared profile of the geostrophic wind is typical of the 11 September 1974 squall line environment observed during the GATE phase-III.

The initial thermodynamic conditions are horizontally uniform. Cloud fields are initiated by introducing small, random temperature perturbations into the lowest model layer after the first 30 minutes of integration. The initial thermodynamic state used in this simulation is identical to that used in Xu and

Krueger (1991). The numerical simulation, with a Coriolis parameter of 15°N , was run for 11 days with a time step of 10 seconds.

3.2 Thermodynamic and Cloud Microphysical Fields

Figure 1 shows the time evolution of the cloud top temperature from 3 to 7 days, indicated by a linear gray scale; white represents 200 k, while black denotes 300 k. Cirrus anvils associated with cumulonimbi appear white. From Fig. 1 we see that cumulus convection is organized into long-lived mesoscale systems. These systems have convective bands of small horizontal extent that are accompanied by cirrus anvils behind the bands. Some midlevel stratiform clouds also appear behind the bands. To study the effects of the tropical mesoscale convective system on the radiative fields, the simulated thermodynamic and bulk hydrometeor fields are obtained from a 6-hour average from 4.75 to 5 days. In the next section we will present the radiation budgets of the mesoscale convective system computed from these fields. The 6-hour average thermodynamic and microphysical fields are presented below.

Figure 2 shows the detailed cross sections (x-z) of the simulated cloud and precipitation fields. The leading convective-stratiform area has a large horizontal extent of ~ 320 km. The anvil cloud associated with the mesoscale convective system has a horizontal scale of ~ 250 km, which extends from the middle-front to the back of the system. The system moves westward (from right to left) and consists of significant precipitation that covers a region of ~ 100 km. To examine the spatial distribution of the radiation field associated with a mesoscale convective system, we shall confine our presentation to the horizontal domain from 120 to 620 km.

Figures 3, 4, and 5 show the x-z sections of the ice phase mixing ratio, water phase mixing ratio, and total hydrometeor mixing ratio, respectively. The

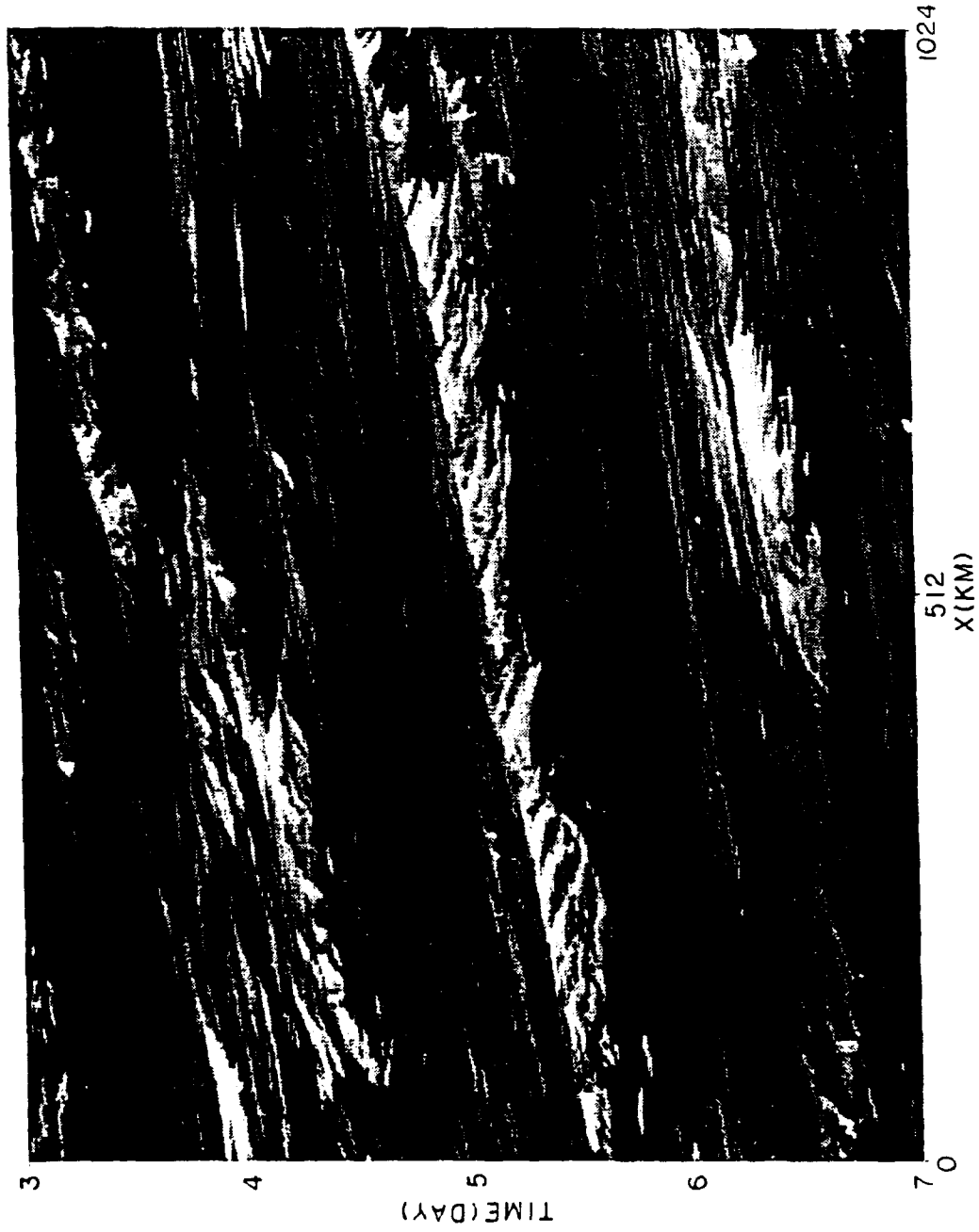


Fig. 1. Hovmöller diagram (x-t section) of the cloud top temperature, based on a 15-minute average. Cloud top temperature is denoted by a linear gray scale; white and black represent 200 and 300 K, respectively.

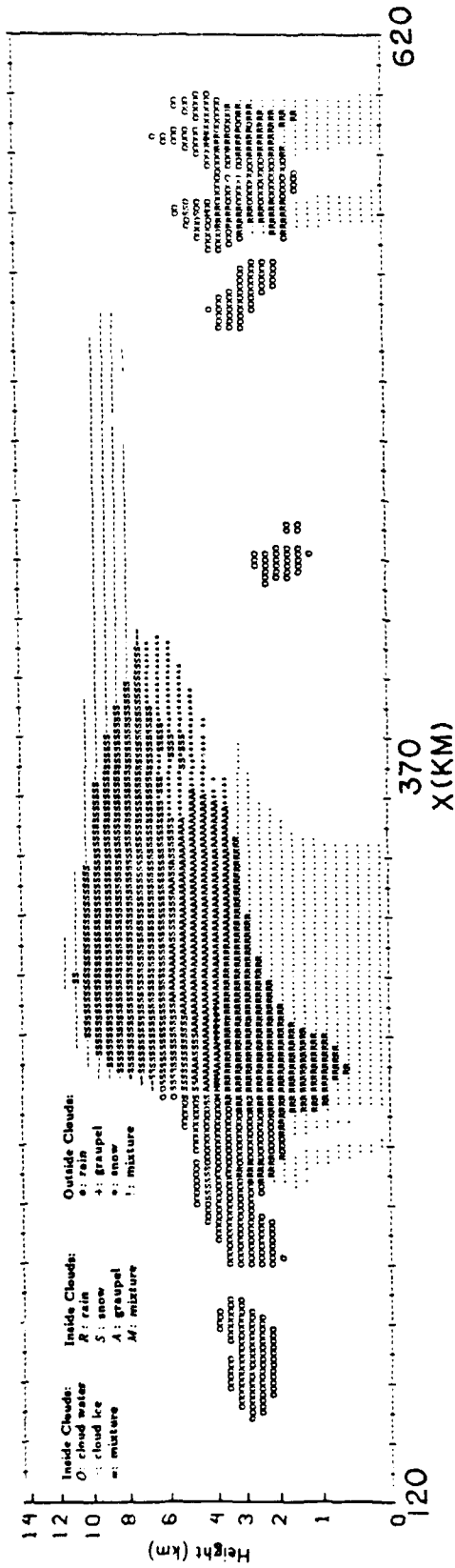


Fig. 2. Cross section (x-z) of the cloud and precipitation fields, based on a 6-hour average from 4.75 to 5 days. The sum of the cloud water and ice mixing ratios exceeds 1% of the saturation water-vapor mixing ratio inside clouds. The sum of rainwater, snow, and graupel mixing ratios exceeds 0.1 g/kg for the precipitation areas outside and inside the clouds.

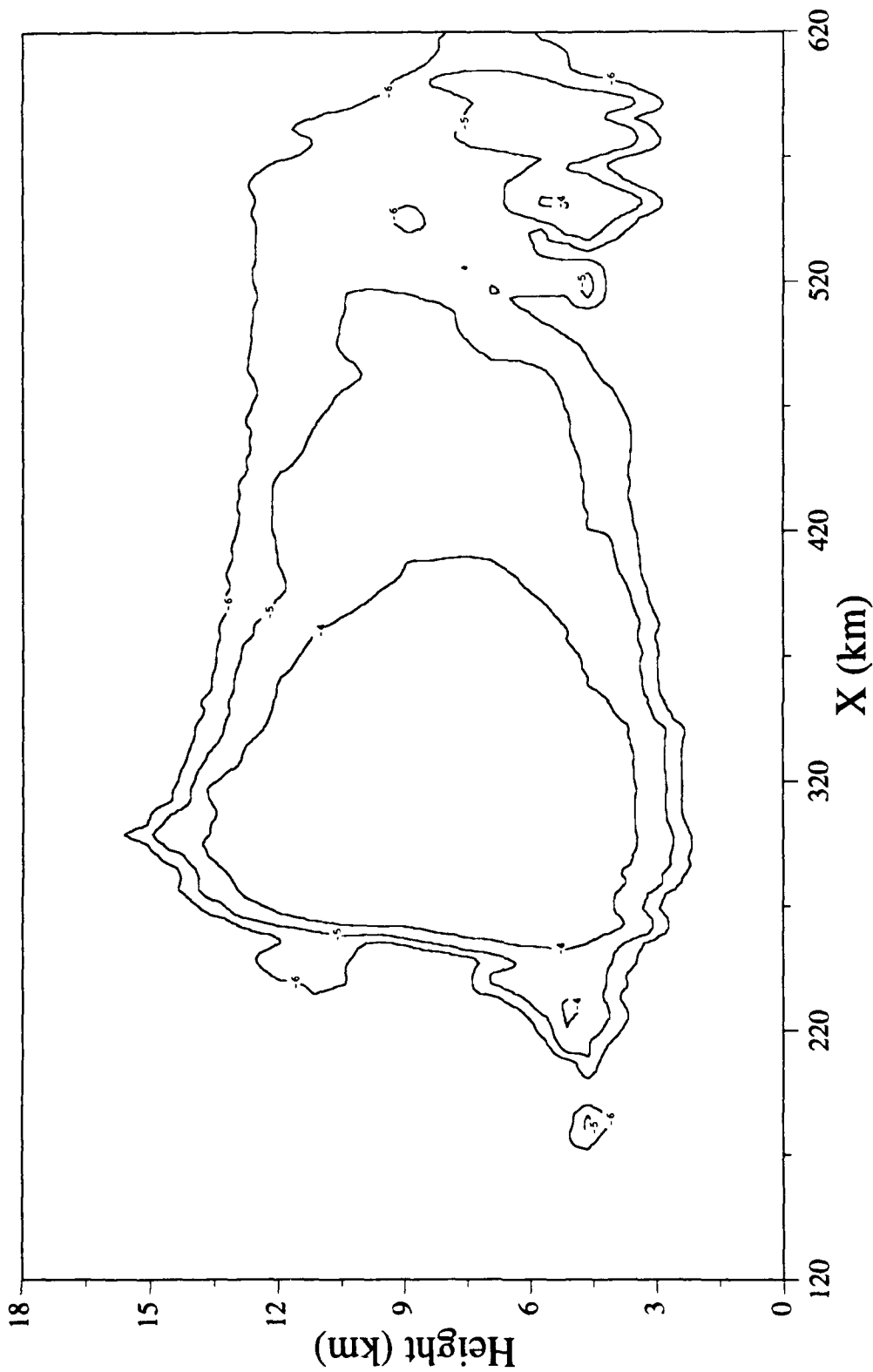


Fig. 3. Cross section (x - z) of the mixing ratio for total ice species (cloud ice, snow, and graupel). The contours are in logarithmic scale with an interval of 10^0 . The lowest contour corresponds to 10^{-6} .

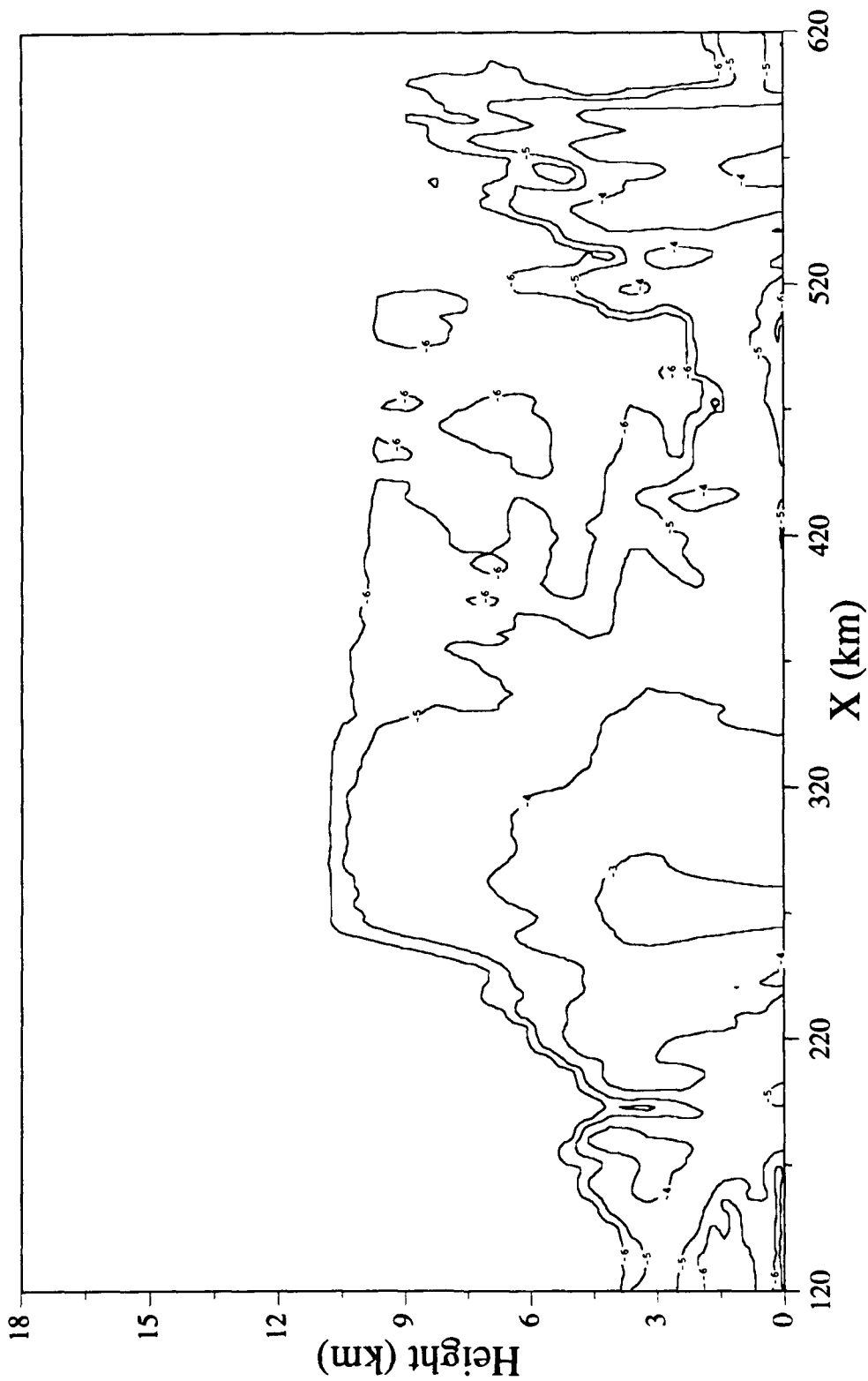


Fig. 4. Same as Fig. 3, except for total liquid water species (cloud water and rain).

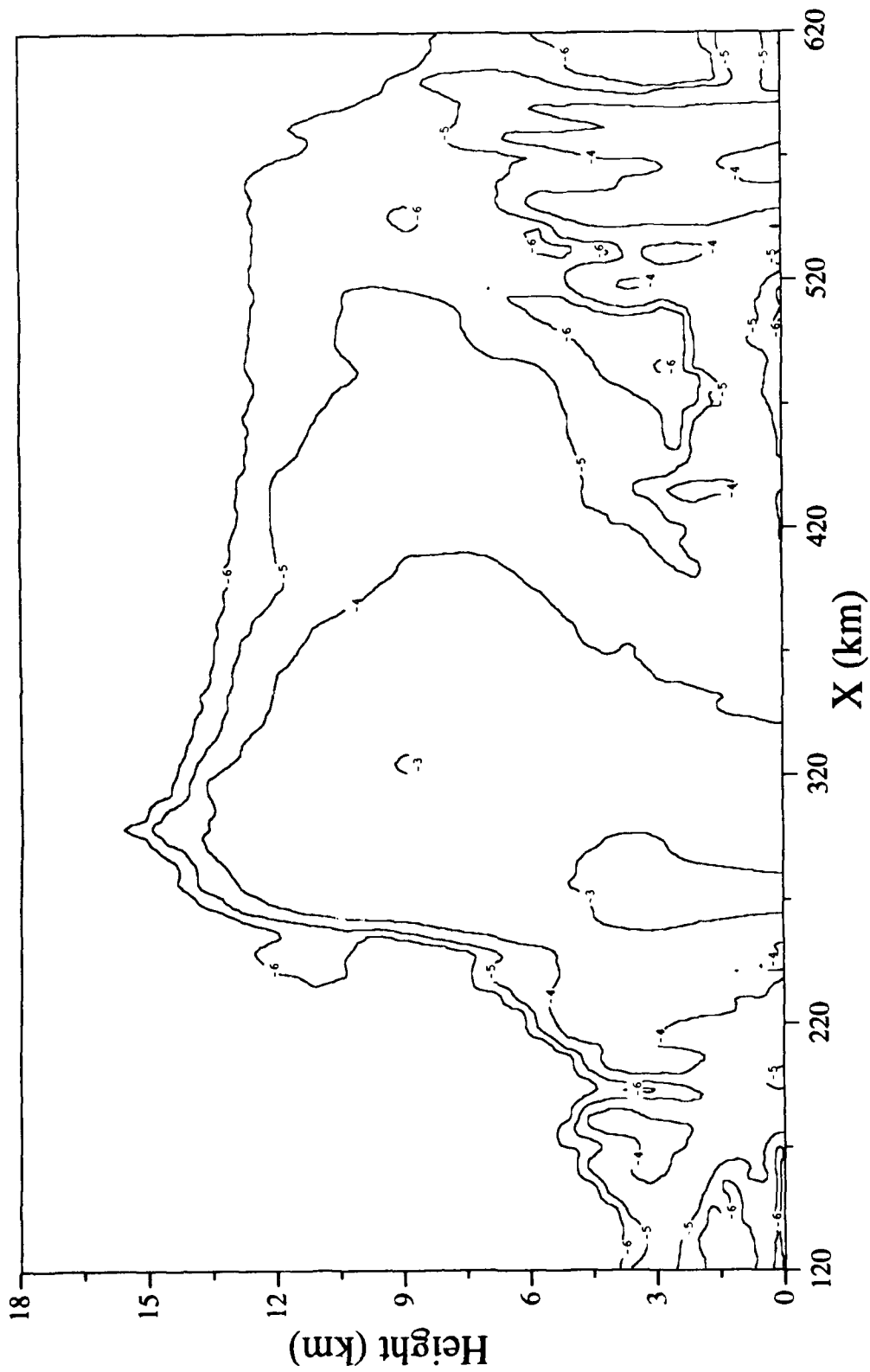


Fig. 5. Same as Fig. 3, except for total hydrometeors (cloud ice, snow, graupel, cloud water, and rain).

anvil base (Fig. 3) is estimated to be at about 3-7 km. The anvil base is not fixed because it consists of melting snow/graupel. The anvil as shown in Fig. 3 is extremely thick, ~4-12 km, with cloud tops located at ~10-15 km. The maximum total ice water mixing ratio is ~1 g/kg in this case. The maximum liquid water mixing ratio (Fig. 4) is ~2.4 g/kg, which is largely due to raindrops. Heavy rain occurs just behind the gust front (the left side of the deep cumulonimbi which form the squall line is the location where the principal updraft occurs), as seen from Fig. 5. The deep cumulonimbi continually propagate into the ambient air ahead where new growth occurs, while older towers successively join the main anvil mass (Zipser, 1977). The rain observed in the 310-350 km zone comes from the anvil base, where very few low clouds exist (See Fig. 2 and 5). Figure 6 shows the vertical distribution of the mixing ratios for total liquid water, ice water, and hydrometeor at 217, 317, and 417 km. The microphysical distributions at those three positions represent the pictures in front of the squall line, at the center of the cloud area, and in the rear of the system, respectively. At 217 km, the total hydrometeor mixing ratio is dominated by water phase, while at 417 km, ice phase prevails. At $x = 317$ km, the total liquid water is largely due to raindrops which fall from the anvil. The total liquid water mixing ratios at 217 and 417 km are largely due to cloud drops. From Fig. 6, it is seen that the mixing ratio of ice phase reaches its maximum in the middle of the anvil, while water phase shows a maximum mixing ratio near the cloud top.

Figure 7 shows the first model layer temperature above the surface ($z = 47$ m) as a function of the horizontal distance (solid line). Also shown are the sea surface temperature (dotted line) and initial temperature at $z = 47$ m (dashed line). The temperature drops rapidly as expected with the passage of the gust front, after which a more normal value is reached. Figure 7 indicates cooling

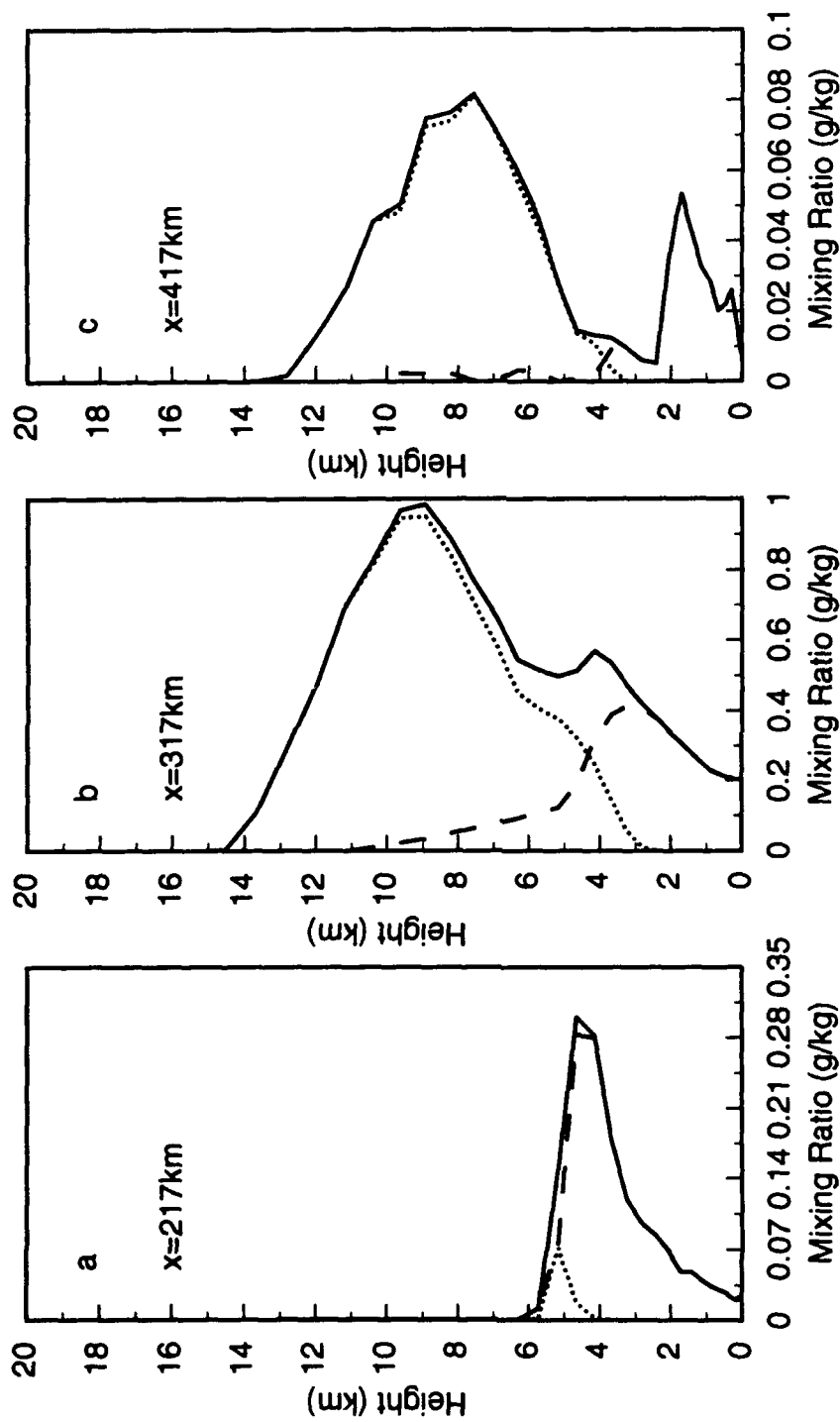


Fig. 6. Mixing ratios of total ice species (---), total liquid water species (---), and total hydrometeors (—), as functions of height at (a) $x = 217$ km, (b) $x = 317$ km, and (c) $x = 417$ km.

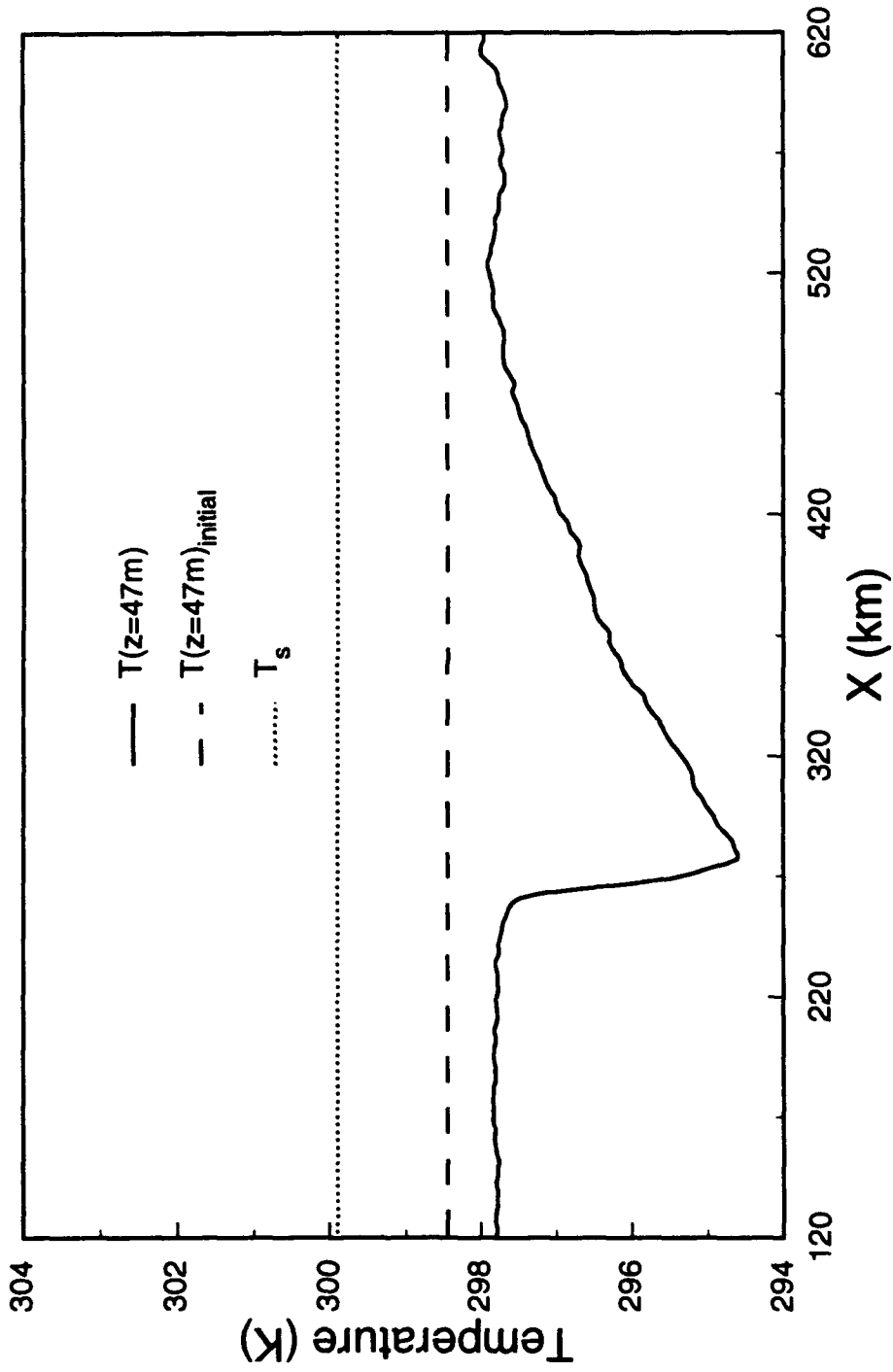


Fig. 7. Surface sea temperature (\cdots), initial first model layer temperature ($---$), and predicted first model layer temperature ($—$) as functions of the horizontal distance.

at the lowest level with respect to the initial field. Large differences between the sea surface temperature ($T_s = 299.9$ K) and the first model layer temperature will significantly affect the radiative fluxes at lower levels.

3.3 Radiation Budget Diagnosis

The cloud thermodynamic and microphysical fields simulated by the CEM are used by the radiation scheme to diagnose the radiative budget of the squall line system. For diagnosis of solar radiation transfer, a solar constant of 1365 W m^{-2} , a surface albedo of 0.05, and a solar zenith angle of 60° are used.

The model top for radiation calculations is set to be 60 km by adding two levels above the CEM domain. These two levels are located at 21 and 60 km. Temperature, water vapor, and ozone profiles at 21 km are assumed to be the same as those of the standard tropical atmosphere. The mixing ratios of H_2O and O_3 at 60 km are determined by equating the path lengths between 21 and 60 km and those obtained from the detailed tropical profile. The temperature at 60 km is set to 240 K, which is the average temperature between 21 and 60 km. The differences in heating rates below 19 km between the values obtained by using the detailed profiles above the cloud model domain and the simplified scheme are within 0.02 K/day.

The average IR heating rate of the first model layer (0-103.5 m) is extremely sensitive to the surface air temperature (T_o). For the initial atmospheric profiles, the IR heating rate of the first layer is -0.74 K/day, obtained by assuming that the surface potential temperature and water vapor mixing ratio are equal to those at 47 m. However, the heating rate is -3.53 K/day if the surface air temperature is assumed to be the same as the sea surface temperature and if the surface mixing ratio (q_{vo}) is assumed to be the saturated

mixing ratio. Thus, it is important to have correct T_0 and q_{v0} in radiative calculations.

Surface fluxes are determined from the flux-profile relationships developed by Businger et al. (1971) and Deardorff (1972). The surface potential temperature flux, $(\overline{w'\theta'})_0$, is given by

$$-(\overline{w'\theta'})_0 = u_*\theta_s = -(\theta_s - \theta_m)C(z_m)u_*, \quad (3.1)$$

where θ_s is the surface value of θ , $\theta_m = \theta(z_m)$, C is a similarity function given below, u_* is the friction velocity, and z_m is set at 47 m which is the first model level height above the surface. The similarity function for the unstable surface layer is

$$C^{-1}(z) = \frac{0.74}{k} \left[\ln \left(\frac{z}{z_0} \right) - 2 \ln \left(\frac{1+y}{2} \right) \right], \quad (3.2)$$

where $y = (1 - 9\xi)^{1/2}$, $\xi = z/L$, k is the Karman constant (0.35), z_0 is the roughness length, and L is the Monin-Obukhov length. From Eq. (3.1), we obtain

$$\theta_s = -(\theta_s - \theta_m)C(z_m). \quad (3.3)$$

A detailed profile of θ from surface to z_m may be constructed by noting that θ_s is independent of height. Thus, we have

$$\theta(z) = \theta_s - (\theta_s - \theta_m)C(z_m)/C(z). \quad (3.4)$$

Similarly, we may construct a detailed profile for the water vapor mixing ratio, q_v , as follows:

$$q_v(z) = q_{vs} - (q_{vs} - q_{vm})C(z_m)/C(z). \quad (3.5)$$

In the present case, θ_s is the potential temperature corresponding to a constant sea surface temperature of 299.9 K, while q_{vs} is the saturation mixing ratio corresponding to this temperature; θ_m and q_{vm} are obtained from CEM. From GATE

data, typical values for z_0 and L are 0.6×10^{-3} m and -5 m, respectively. For the initial atmospheric condition, the IR heating rate for the first model layer is -1.25 K/day obtained by using the detailed profiles from 0 to 47 m with a vertical resolution of 1 m in the radiation calculation. For different z_0 (0.2×10^{-3} - 0.6×10^{-2} m) and L (-1 - -20 m), the IR heating rate ranges from -1.2 to -1.3 K/day.

Based on numerical experimentation, by setting

$$\begin{aligned} \theta_0 &= \theta(z'), \\ q_{v0} &= q_v(z'), \end{aligned} \quad (3.6)$$

the IR heating rates computed from using the CEM model resolution agree with those from the detailed calculation within 0.1 K/day. The parameter z' is related to L by

$$z' = 0.2766 + 0.2324 \ln|L|. \quad (3.7)$$

For L ranging from -1 to -20 , z' ranges from 0.28 to 0.97 m.

3.3.1 Heating Rate Fields

In the following radiation calculations, we set $z_0 = 0.6 \times 10^{-3}$ m, and set $L = -5$ m. Figure 8 shows the detailed cross-section (x - z) of the computed solar heating rates. Solar radiation heats the upper portions of the clouds. The maximum heating rate is -16.7 K/day, which occurs at the top of the deep cumulonimbi. The solar heating penetrates through the anvil top for ~ 3 km. The solar heating rate field in a squall line system shows a significant vertical and horizontal variability.

Figure 9 shows the infrared heating rate field in the squall line system. Similar to solar heating, a significant spatial variability is evident. Strong infrared cooling occurs at the cloud top. The maximum cooling is -24.9 K/day.

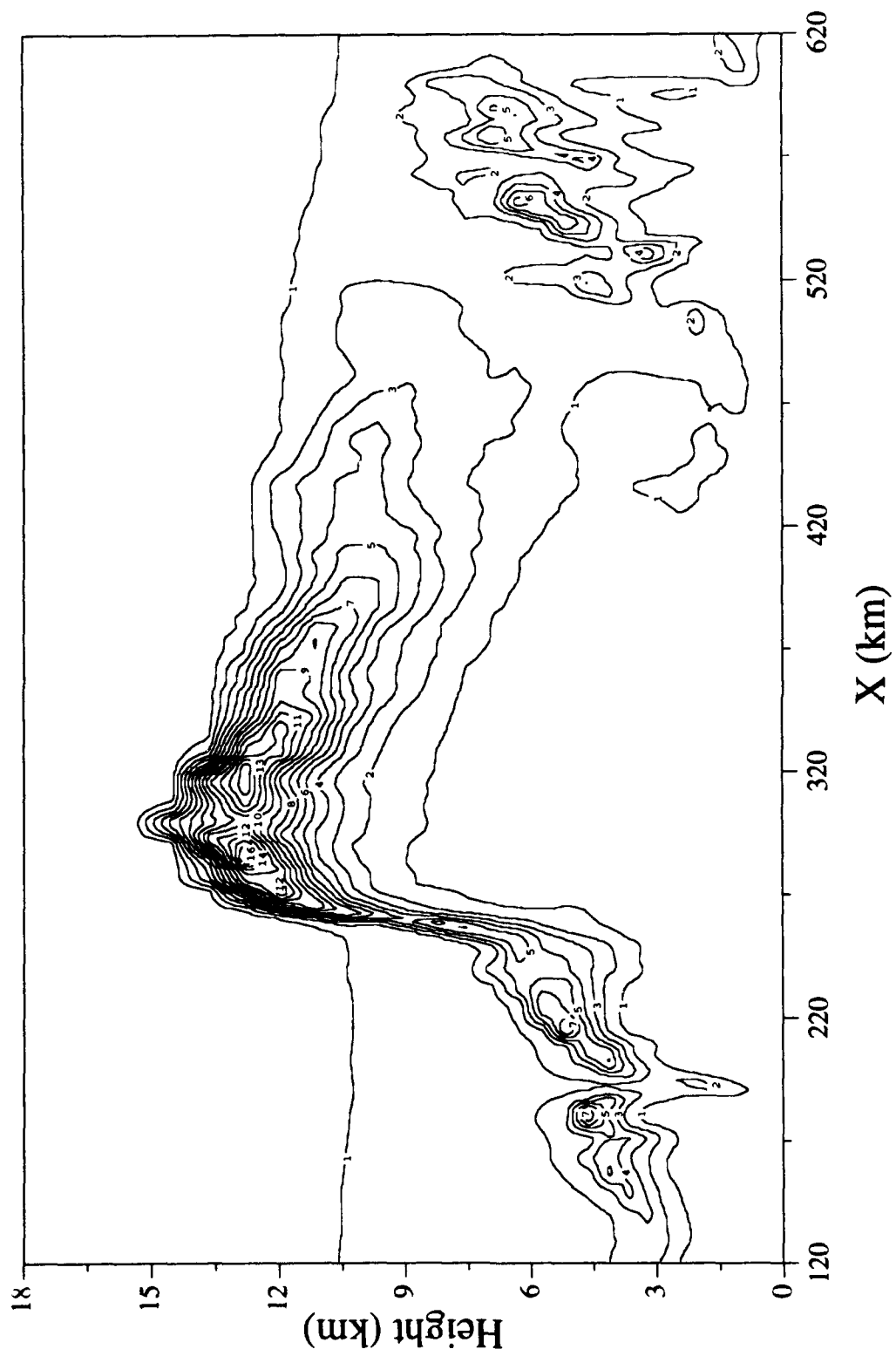


Fig. 8. Cross section (x - z) of the solar heating rate with a contour interval of 1 K/day.

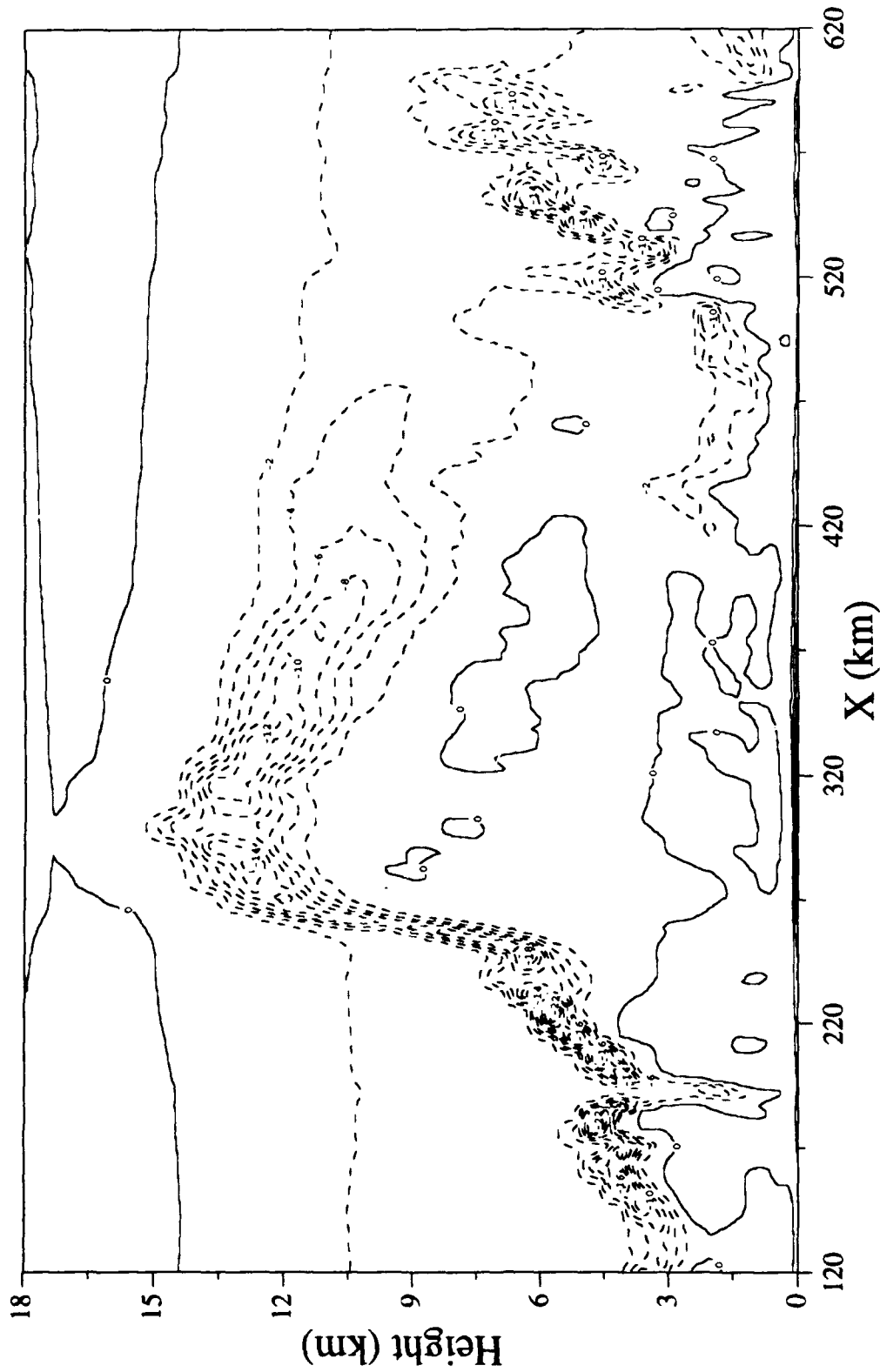


Fig. 9. Cross section (x-z) of the IR heating rate with a contour interval of 2 K/day. The dashed contours represent cooling.

Little infrared heating exists near the cloud base. The noticeable heating near the surface is primarily due to the warmer sea surface temperature, as shown in Fig. 7, and also due in part to strong absorption of rain. The maximum infrared heating is -15.9 K/day, which is smaller than the maximum cooling value. Like the solar heating rate field, the infrared heating rate pattern is closely related to the hydrometeor mixing ratio field. Comparing Fig. 8 with Fig. 9, we see that the maximum solar heating occurs below the maximum infrared cooling.

Shown in Fig. 10 is the net radiative heating rate. Since solar heating and IR cooling rates are comparable in the upper portion of the anvil, and since the maximum solar heating occurs below the maximum infrared cooling, the net heating rate shows a slight cooling at the cloud top and a slight heating immediately below. At the cloud top where water phase dominates, IR cooling is much higher than solar heating, resulting in strong net cooling. Generally, the net radiative heating rate field shows cooling at the cloud top and heating at the cloud base and inside clouds. The maximum heating and cooling rates are 16.0 and 18.0 K/day, respectively. Radiative cooling at the cloud top and heating near the cloud base would tend to generate convective mixing of the cloud layer.

The radiative heating rate profiles at 217, 317, and 417 km are shown in Fig. 11(a), (b), and (c), respectively. In these cases, since cumulus/cumulonimbus clouds are connected to the surface through falling rain, a strong IR heating occurs at the surface. The net radiative heating profiles at all three positions exhibit cooling near the upper portion and heating within the deeper levels. From these results, it is clear that both solar and IR radiation are important in determining the cloud radiative budget.

3.3.2 Cloud Radiative Forcing

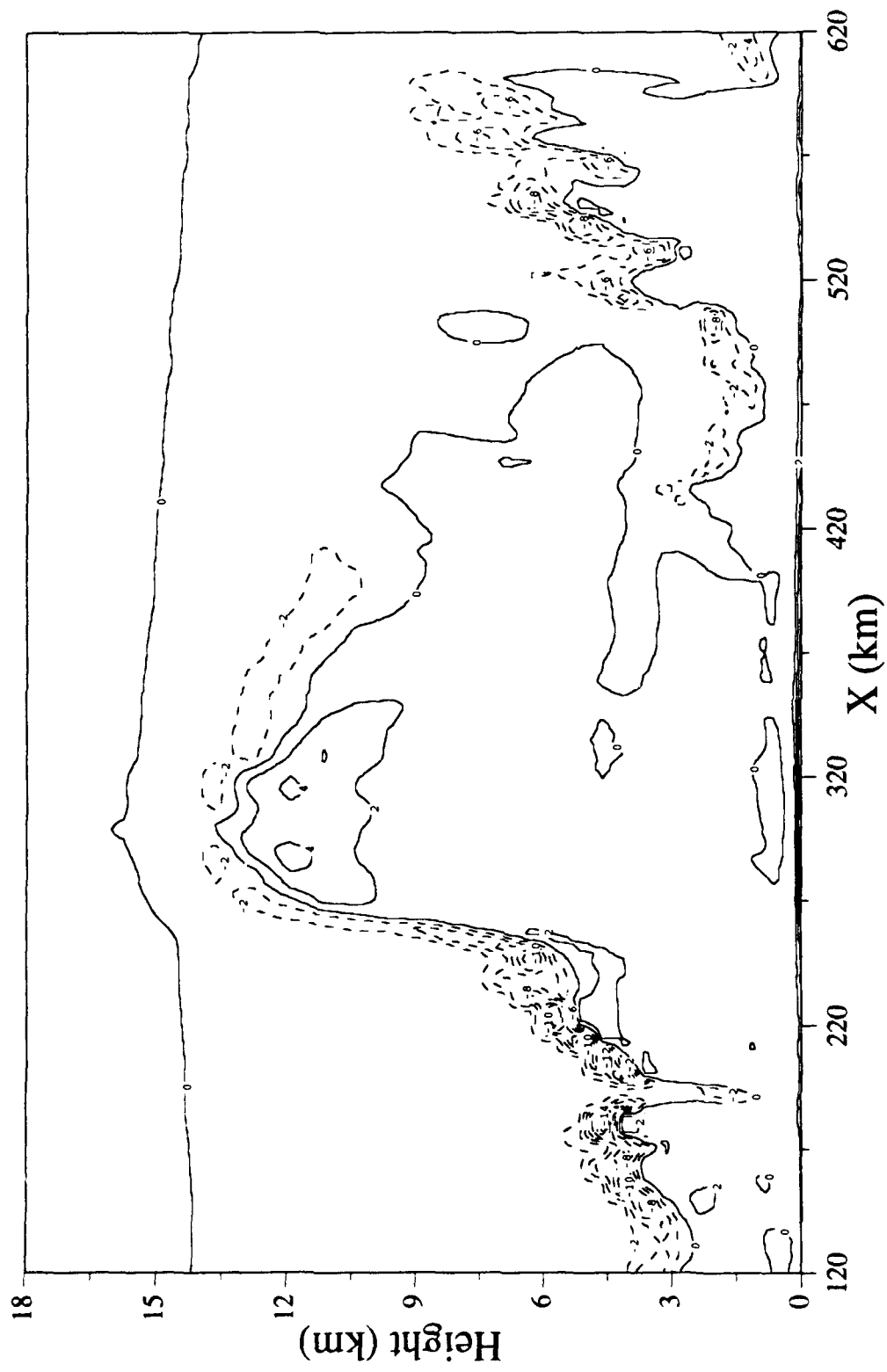


Fig. 10. Cross section (x-z) of the net (IR plus solar) heating rate with a contour interval of 2 K/day. The dashed contours represent cooling.

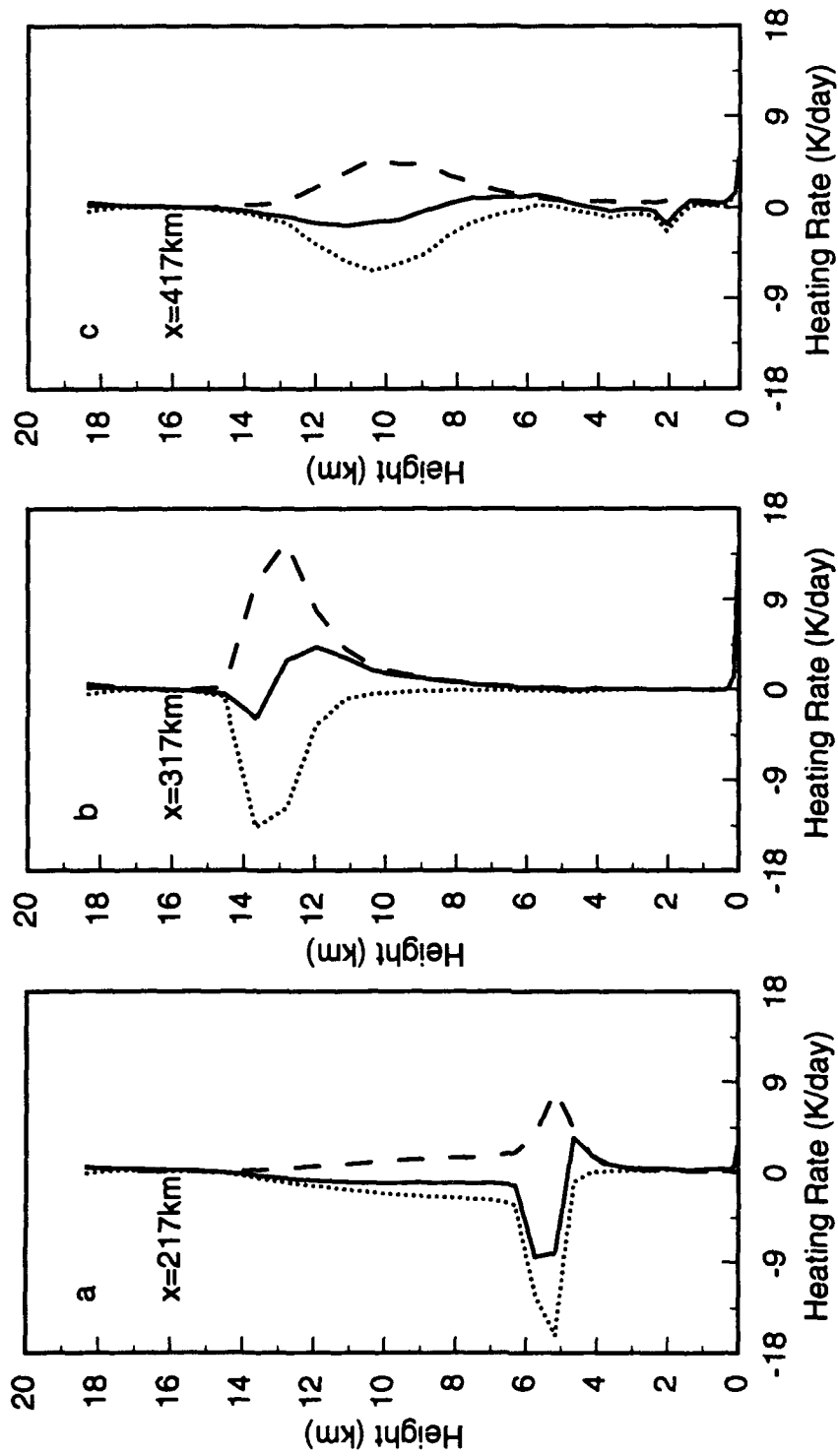


Fig. 11. Solar (—), IR (···), and net (---) heating rates as functions of height at (a) $x = 217$ km, (b) $x = 317$ km, and (c) $x = 417$ km.

For the earth-atmosphere system, the cloud solar radiative forcing is defined as the difference between the reflected solar fluxes at the top of the atmosphere for clear and cloudy skies. The cloud IR radiative forcing is defined as the difference between the outgoing IR fluxes for clear and cloudy skies. The net cloud radiative forcing is the sum of the two. The concept of cloud radiative forcing provides a means to indicate energy gain/loss of the earth-atmosphere system due to the presence of clouds. Cloud radiative forcing may be defined with reference to the surface and the atmosphere.

Figure 12 shows the cloud radiative forcing (for the earth-atmosphere system) due to the presence of a squall line. As noted previously, the cloud IR forcing at the cloud top is always positive, corresponding to the heating of the system due to the cloud greenhouse effect, while the cloud solar forcing is always negative, indicating the cooling of the system by the cloud albedo effect. The cloud IR forcing ranges from 14.7 to 162.4 W/m^2 , while the solar counterpart ranges from -129.3 to -418.7 W/m^2 . The net radiative effect of clouds leads to the cooling of the earth-atmosphere system. It is interesting to note that the maximum IR forcing is located in the areas of deep convection, with high cloud tops and large optical depth. The net cloud radiative forcing at the top of the atmosphere is between -109.0 and -360.7 W/m^2 in a squall line system.

Figure 13 shows the cloud radiative forcing at the surface. The IR forcing is always positive (23.4-50.2 W/m^2) because the cloud base emission is higher than the emission from a clear atmosphere at the cloud base height. From Fig. 13 it is noted that the negative surface cloud forcing values due to solar radiation (-134.4--443.8 W/m^2) are substantially similar to that presented in Fig. 12 (dashed line). This is because the atmosphere is largely transparent with respect to solar radiation. The net surface cloud forcing ranges between -111.0 and -397.9 W/m^2 .

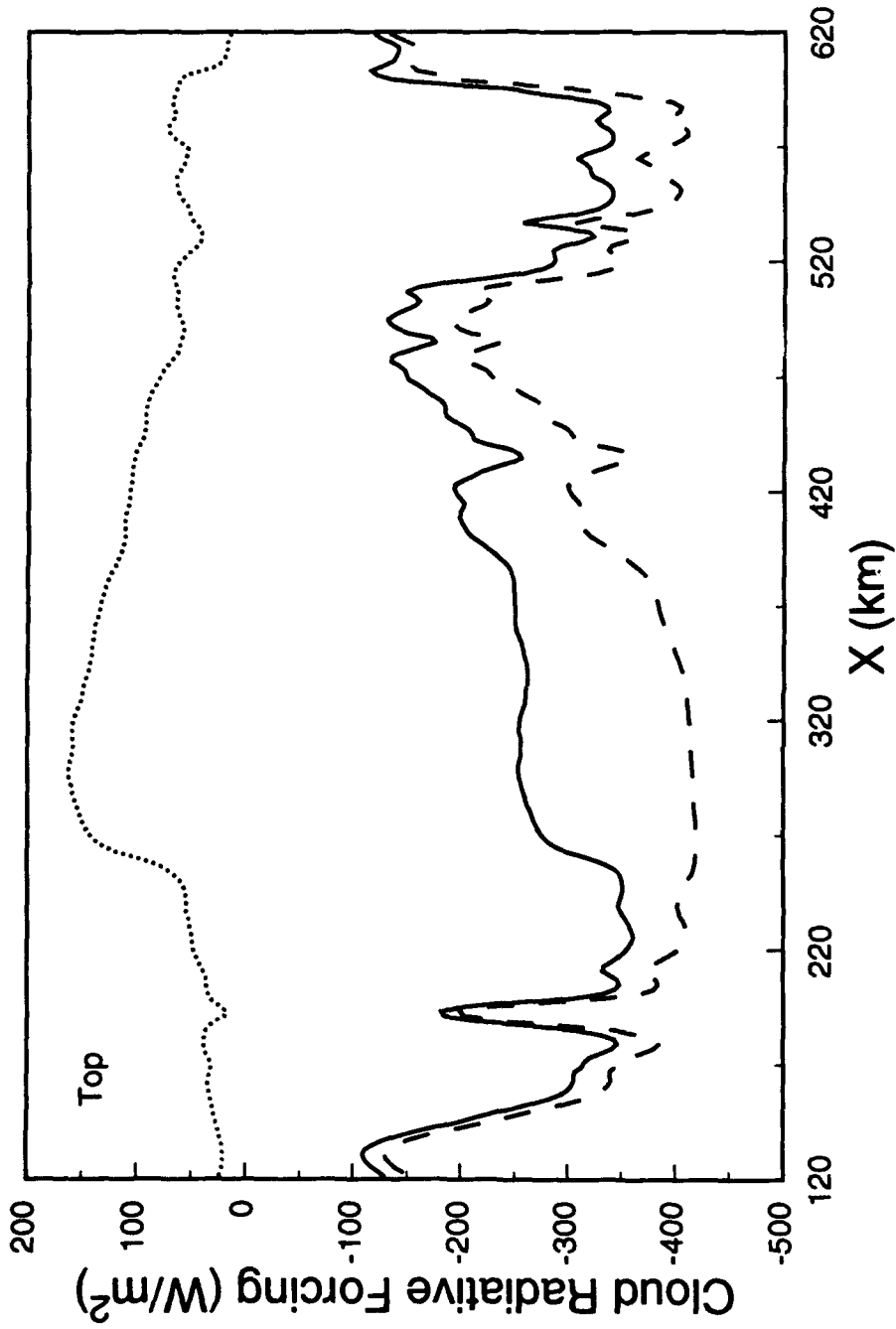


Fig. 12. Cloud radiative forcings at the top of the atmosphere for solar (---), IR (—), and net (· · ·) radiation as functions of the horizontal distance.

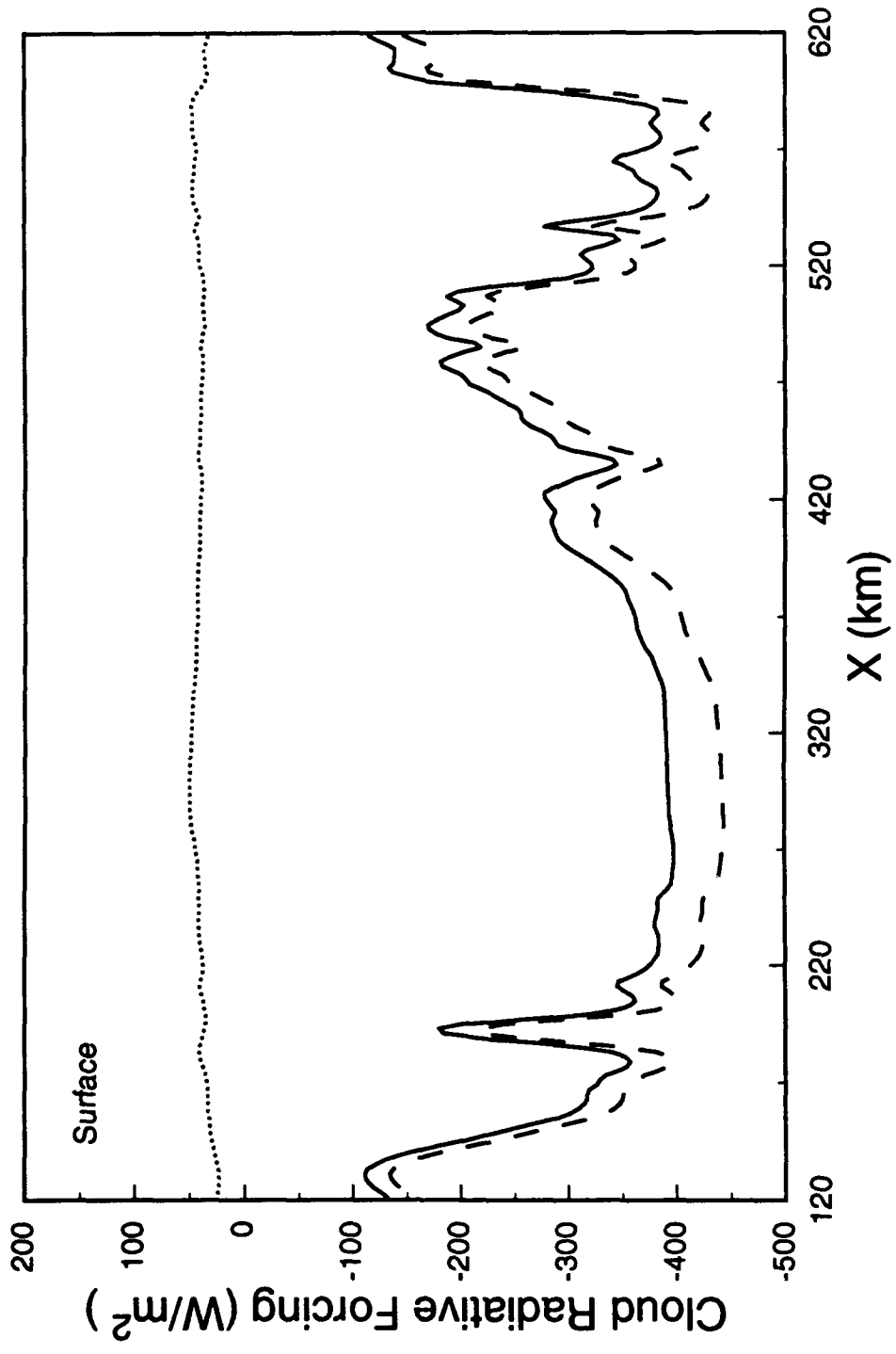


Fig. 13. Same as Fig. 12, except at the surface.

Figure 14 depicts the cloud radiative forcing for the atmosphere, which is the difference between the cloud radiative forcing at the top and that at the surface. The solar warming due to the presence of clouds is small, ranging from 3.4 to 30.9 W/m². The cloud IR forcing is also positive in the areas where high clouds are present: a large value of 112.2 W/m² in the case of deep cumulonimbi is shown. For low clouds, the cloud IR forcing is negative with values up to -18.9 W/m². The net atmospheric cloud radiative forcing is between -3.1 and 138.9 W/m² in the present study.

Referring to Figs. 12, 13, and 14, we conclude that in a squall line system (or tropical deep convective areas), the cloud solar forcing for the earth-atmosphere system is largely confined to the sea surface, while the cloud IR forcing is mainly confined within the atmosphere. The net radiation effect is cooling at the surface and heating within the atmosphere. Thus, the radiative effect of clouds is similar to the latent heat release in that both remove heat from the surface and deposit it into the atmosphere (Ramanathan, 1987). However, the surface cooling resulting from the reduction of solar radiation is significantly larger than the heating in the atmosphere produced by IR radiative exchanges. The presence of clouds significantly modifies the vertical distribution of radiative heating/cooling which would significantly affect atmospheric convection and dynamic processes.

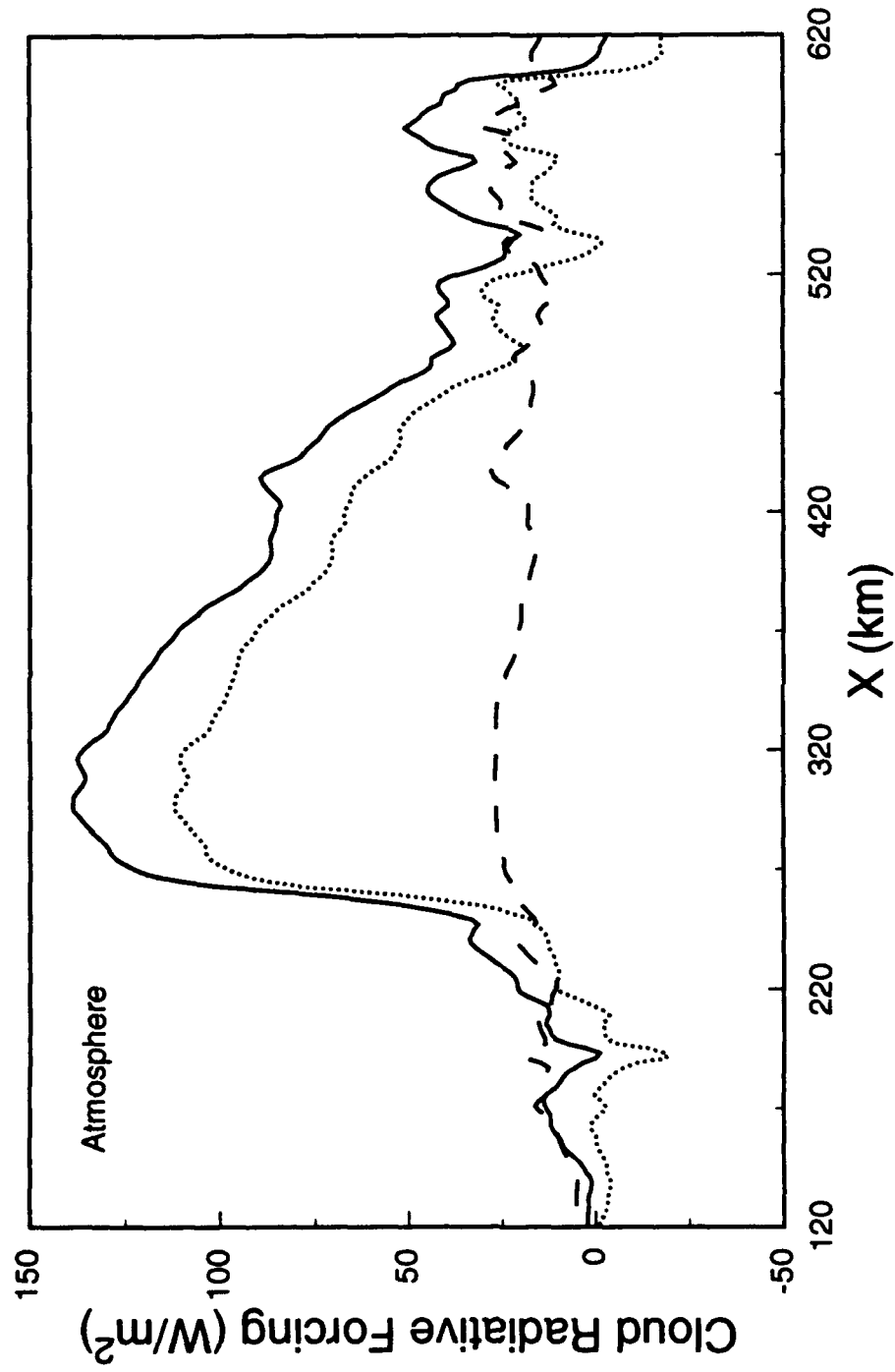


Fig. 14. Same as Fig. 12, except in the atmosphere.

Section 4

SUMMARY

We have interfaced the newly developed radiation scheme with a CEM to investigate the interactions between the radiation field and tropical convective systems. The thermodynamic, water vapor, and bulk hydrometeor fields provided by the CEM are used as diagnostic inputs for radiation calculations. The radiative properties of hydrometeors, including water droplets, ice crystals, rain, snow, and graupel have been treated explicitly. The single-scattering properties of ice crystals are parameterized as functions of mean effective size and ice water content, based on a light scattering program for hexagonal plates and columns. The scattering and absorption properties of water droplets are represented as functions of mean effective radius and liquid water content based on Mie scattering calculations. Moreover, the radiative properties of rain, snow, and graupel are calculated from Mie theory using Marshall-Palmer distributions that are employed in the bulk microphysical parameterization. A δ -four-stream radiative transfer scheme has been developed for flux calculations in both solar and infrared spectra. For nongray gaseous absorption due to H_2O , CO_2 , O_3 , CH_4 , and N_2O , the correlated k-distribution method is used, which can be readily incorporated into scattering models.

The initial thermodynamic state based on the GATE Phase-III mean sounding is used along with the present CEM to simulate a tropical squall line system. The CEM was able to simulate many characteristic features of tropical squall lines, such as the size and shape of the clouds associated with the tropical mesoscale convective system. The radiation budgets are calculated by using the CEM simulated thermodynamic and hydrometeor fields.

By examining the radiative heating rate fields, it is found that solar radiation heats the upper part of the cloud, which would stabilize the cloud

layer and evaporate the cloud particles. On the contrary, IR cooling occurs at the cloud top, which would enhance the convective instability. Significant heating at the cloud base does not take place in deep anvils because of the presence of low clouds and because of the high cloud-base temperature and large air density. Because the maximum solar heating occurs below the maximum IR cooling, the net radiative heating shows a pattern of cooling above heating in the upper part of the cloud layer. This pattern could result in convection at the cloud top and promote entrainment.

The tropical mesoscale system has a significant impact on the radiative budget of the earth atmosphere system. The system reduces the loss of IR fluxes emitted from the top of the atmosphere and increases IR emission to the surface. In the deep convective areas, the reduction of the loss of IR fluxes emitted from the top of the atmosphere can be as large as 160 W/m^2 , which is redistributed to the surface and the atmosphere by -50 and -110 W/m^2 , respectively. The tropical mesoscale system significantly increases the solar albedo. The deep convective clouds reflect -420 W/m^2 more flux than clear sky and largely reduce the solar fluxes available at the sea surface.

The radiative fields, including both heating rate and cloud radiative forcing, show significant vertical and horizontal variabilities in the presence of the tropical mesoscale systems. The circulation patterns can be profoundly modulated by these variabilities. It should be noted that the vertical grid used in the present study is stretched from $\sim 100 \text{ m}$ near the surface to $\sim 1000 \text{ m}$ at the top of the GEM. Thus, the vertical resolution at the deep convective cloud top for radiation calculations is $\sim 1 \text{ km}$. This is not sufficient to resolve the small-scale vertical structure involving the heating rate profile at the cloud top for the investigation of the interactions of radiation, microphysical

processes, and dynamic motions. The effects of vertical resolution on these interactions require further numerical studies.

REFERENCES

- Ackerman, T.P., K.N. Liou, F.P.J. Valero, and L. Pfister, 1988: Heating rates in tropical anvils. J. Atmos. Sci., 45, 1606-1623.
- Businger, J.A., J.C. Wyngaard, Y. Izumi, and E.F. Bradley, 1971: Flux-profile relationships in the atmospheric surface layer. J. Atmos. Sci., 28, 181-189.
- Chen, S., and W.R. Cotton, 1988: The sensitivity of a simulated extratropical mesoscale convective system to longwave radiation and ice-phase microphysics. J. Atmos. Sci., 45, 3897-3910.
- Danielson, E.F., 1982: A dehydration mechanism for the stratosphere. Geophys. Res. Lett., 9, 605-608.
- Deardorff, J.W., 1972: Parameterization of the planetary boundary layer for use in general circulation models. Mon. Wea. Rev., 100, 93-106.
- Dudhia, J., 1989: Numerical study of convection observed during the winter monsoon experiment using a mesoscale two-dimensional model. J. Atmos. Sci., 46, 3077-3107.
- Ellingson, R.G., and Y. Fouquart, 1990: The intercomparison of radiation codes in climate models (ICRCCM). WCRP-39, WMO/TD-No. 371.
- Fouquart, Y., B. Bonnel, and V. Ramaswamy, 1991: Intercomparing shortwave radiation codes for climate studies. J. Geophys. Res., 96, 8955-8968.
- Fu, Q., 1991: Parameterization of radiative processes in vertically non-homogeneous multiple scattering atmospheres. Ph.D. dissertation, University of Utah, 259 pp.
- Fu, Q., and K.N. Liou, 1992a: Parameterization of the radiative properties of cirrus clouds. Accepted by J. Atmos. Sci.
- Fu, Q., and K.N. Liou, 1992b: On the correlated k-distribution method for radiative transfer in nonhomogeneous atmospheres. J. Atmos. Sci., 49, (December).
- Heymsfield, A.J., 1975: Cirrus uncinus generating cells and the evolution of cirriform clouds. J. Atmos. Sci., 32, 799-808.
- Heymsfield, A.J., and C.M.R. Platt, 1984: A parameterization of the particle size spectrum of ice clouds in terms of the ambient temperature and the ice water content. J. Atmos. Sci., 41, 846-855.
- Krueger, S.K., 1985: Numerical simulation of tropical cumulus clouds and their interaction with the subcloud layer. Ph.D. dissertation, University of California, Los Angeles, 205 pp.
- Krueger, S.K., 1988: Numerical simulation of tropical cumulus clouds and their interaction with the subcloud layer. J. Atmos. Sci., 45, 2221-2250.

- Lilly, D.K., 1988: Cirrus outflow dynamics. J. Atmos. Sci., 45, 1594-1605.
- Lin, Y.-L., R.D. Farley, and H.D. Orville, 1983: Bulk parameterization of the snow field in a cloud model. J. Climate Appl. Meteor., 22, 1065-1092.
- Liou, K.N., 1975: Applications of the discrete-ordinate method for radiative transfer to inhomogeneous aerosol atmospheres. J. Geophys. Res., 80, 3434-3440.
- Liou, K.N., and G.D. Wittman, 1979: Parameterization of the radiative properties of clouds. J. Atmos. Sci., 36, 1261-1273.
- Liou, K.N., 1986: Influence of cirrus clouds on weather and climate processes: A global perspective. Mon. Wea. Rev., 114, 1167-1199.
- Liou, K.N., Q. Fu, and T.P. Ackerman, 1988: A simple formulation of the delta-four-stream approximation for radiative transfer parameterizations. J. Atmos. Sci., 45, 1940-1947.
- Lipps, F.B., and R.S. Hemler, 1986: Numerical simulation of deep tropical convection associated with large-scale convergence. J. Atmos. Sci., 43, 1796-1816.
- Lord, S.J., H.E. Willoughby, and J.M. Piotrowicz, 1984: Role of a parameterized ice-phase microphysics in an axisymmetric, nonhydrostatic tropical cyclone model. J. Atmos. Sci., 41, 2836-2848.
- Mellor, G.L., and T. Yamada, 1974: A hierarchy of turbulence closure models for planetary boundary layers. J. Atmos. Sci., 31, 1791-1806.
- Rotunno, R., J.B. Klemp, and M.L. Weisman, 1988: A theory for strong, long-lived squall lines. J. Atmos. Sci., 45, 463-485.
- Stackhouse, Jr., P.W., and G.L. Stephens, 1991: A theoretical and observational study of the radiative properties of cirrus: Results from FIRE 1986. J. Atmos. Sci., 48, 2044-2059.
- Stephens, G.L., 1978: Radiative properties of extended water clouds. Part I. J. Atmos. Sci., 35, 2111-2122.
- Strivastava, R.C., 1967: A study of the effects of precipitation on cumulus dynamics. J. Atmos. Sci., 24, 36-45.
- Takano, Y., and K.N. Liou, 1989: Radiative transfer in cirrus clouds. I. Single scattering and optical properties of hexagonal ice crystals. J. Atmos. Sci., 46, 3-19.
- Tao, W.-K., J. Simpson, and S.-T. Soong, 1987: Statistical properties of a cloud-ensemble: A numerical study. J. Atmos. Sci., 44, 3175-3187.
- Xu, K.-M., and S.K. Krueger, 1991: Evaluation of cloudiness parameterizations using a cumulus ensemble model. Mon. Wea. Rev., 119, 342-367.

Xu, K.-M., A. Arakawa, and S.K. Krueger, 1992: The macroscopic behavior of cumulus ensembles simulated by a cumulus ensemble model. J. Atmos. Sci., in press.

Zipser, E.J., 1977: Mesoscale and convective-scale downdrafts as distinct components of squall-line structure. Mon. Wea. Rev., 105, 1568-1589.

Appendix

PARAMETERIZATION OF THE RADIATIVE PROPERTIES
OF CIRRUS CLOUDS

Qiang Fu and K. N. Liou

Department of Meteorology/CARSS
University of Utah
Salt Lake City, Utah 84112To appear in Journal of the Atmospheric Sciences, May, 1993

ABSTRACT

A new approach for parameterization of the broadband solar and infrared radiative properties of ice clouds has been developed. This parameterization scheme integrates in a coherent manner the δ -four-stream approximation for radiative transfer, the correlated k-distribution method for nongray gaseous absorption, and the scattering and absorption properties of hexagonal ice crystals. We use a mean effective size, representing an area weighted mean crystal width, to account for the ice crystal size distribution with respect to radiative calculations. Based on physical principles, the basic single-scattering properties of ice crystals, including the extinction coefficient divided by ice water content, single-scattering albedo, and expansion coefficients of the phase function, can be parameterized using third-degree polynomials in terms of the mean effective size. In the development of this parameterization, we use the results computed from a light scattering program that includes a geometric ray-tracing program for size parameters larger than 30 and the exact spheroid solution for size parameters less than 30. The computations are carried out for 11 observed ice crystal size distributions and cover the entire solar and thermal infrared spectra. Parameterization of the single-scattering properties is shown to provide an accuracy within about 1%. Comparisons have been carried out between results computed from the model and those obtained during the 1986 cirrus FIRE IFO. We show that the model results can be used to reasonably interpret the observed IR emissivities and solar albedo involving cirrus clouds. The newly developed scheme has been employed to investigate the radiative effects of ice crystal size distributions. For a given ice water path, cirrus clouds with smaller mean effective sizes reflect more solar radiation, trap more infrared radiation, and produce stronger cloud-top cooling and cloud-base heating. The latter effect would enhance the in-cloud

heating rate gradients. Further, the effects of ice crystal size distribution in the context of IR greenhouse versus solar albedo effects involving cirrus clouds are presented with the aid of the upward flux at the top of the atmosphere. In most cirrus cases, the IR greenhouse effect outweighs the solar albedo effect. One exception occurs when a significant number of small ice crystals is present. The present scheme for radiative transfer in the atmosphere involving cirrus clouds is well suited for incorporation in numerical models to study the climatic effects of cirrus clouds, as well as to investigate interactions and feedbacks between cloud microphysics and radiation.

1. Introduction

Cirrus clouds are globally distributed, being present at all latitudes and without respect to land or sea or season of the year. They regularly cover about 20-30% of the globe and strongly influence weather and climate processes through their effects on the radiation budget of the earth and the atmosphere (Liou, 1986). The importance of cirrus clouds in weather and climate research can be recognized by the intensive field observations that have been conducted as a major component of the First ISCCP Regional Experiment in October-November 1986 (Starr, 1987) and more recently in November 1991.

Cirrus clouds possess a number of unique features. In addition to being global and located high in the troposphere and extending to the lower stratosphere on some occasions, they contain almost exclusively nonspherical ice crystals of various shapes, such as bullet rosettes, plates, and columns. There are significant computational and observational difficulties in determining the radiative properties of cirrus clouds. A reliable and efficient determination of the radiative properties of cirrus clouds requires the fundamental scattering and absorption data involving nonspherical ice crystals. In addition, appropriate incorporation of gaseous absorption in scattering cloudy atmospheres and an efficient radiative transfer methodology are also required.

Although parameterization of the broadband radiative properties for cirrus clouds has been presented by Liou and Wittman (1979) in terms of ice water content, such parameterization used the scattering and absorption properties of circular cylinders without accounting for the effects of the hexagonal structure of ice crystals. Moreover, the effects of ice crystal size distribution were not included in the parameterization. Using area-equivalent or volume-equivalent ice spheres to approximate hexagonal ice crystals for scattering and absorption properties has been shown to be inadequate, and frequently misleading. This is evident in interpreting the scattering and polarization patterns from ice clouds

(Takano and Liou, 1989) and the observed radiative properties of cirrus clouds, in particular, the cloud albedo (Stackhouse and Stephens, 1991).

In this paper, we wish to develop a new approach for the parameterization of the broadband solar and infrared radiative properties of ice crystal clouds. Three major components are integrated in this parameterization, including the scattering and absorption properties of hexagonal ice crystals, the δ -four-stream approximation for radiative transfer, and the correlated k-distribution method for nongray gaseous absorption. Compared with more sophisticated models and aircraft observations, the present parameterization has been shown to be accurate and efficient for flux and heating rate calculations. In Section 2, we present parameterization of the single-scattering properties of ice crystals. The manner in which the radiative flux transfer is parameterized using the δ -four-stream approximation and the correlated k-distribution is discussed in Section 3. Section 4 presents some comparisons between theoretical results and observed data involving cloud emissivity and albedo. In Section 5, we present the effect of ice crystal size distribution on cloud heating rates and on the question of cloud radiative forcing. Summary and conclusions are given in Section 6.

2. Parameterization of the Single-Scattering Properties of Ice Crystals

a. Physical Bases

The calculations of the single-scattering properties, including the phase function, single-scattering albedo and extinction coefficient, require a light scattering program and the detailed particle size distribution. The calculations are usually time consuming. If radiation calculations are to interact with an evolving cloud where particle size distribution varies as a function of time and/or space, the computer time needed for examining just this aspect of the radiation program would be formidable, even with a super computer. Thus, there is a practical need to simplify the computational procedure for the calculation

of the single-scattering properties of cloud particles. Since spheres scatter an amount of light proportionate to their cross-section area, a mean effective radius, which is defined as the mean radius that is weighted by the cross-section area of spheres, has been used in conjunction with radiation calculations (Hansen and Travis, 1974). Higher order definition, such as dispersion of the droplet size, may be required in order to more accurately represent the droplet size distribution.

Ice crystals are nonspherical and ice crystal size distributions are usually expressed in terms of the maximum dimension (or length). Representation of the size distribution for ice crystals is much more involved than that for water droplets. To the extent that scattering of light is proportional to the cross-section area of nonspherical particles, we may use a mean effective size analogous to the mean effective radius defined for spherical water droplets as follows:

$$D_e = \int_{L_{\min}}^{L_{\max}} D \cdot DLn(L) dL / \int_{L_{\min}}^{L_{\max}} DLn(L) dL, \quad (2.1)$$

where D is the width of an ice crystal, $n(L)$ denotes the ice crystal size distribution, and L_{\min} and L_{\max} are the minimum and maximum lengths of ice crystals, respectively. A similar definition for circular cylinders has also been proposed by Platt and Harshvardhan (1988). Based on aircraft observations by Ono (1969) and Auer and Veal (1970), the width may be related to the length L . It follows that the mean effective width (or size) can be defined solely in terms of ice crystal size distribution. The geometric cross section area for oriented hexagonal ice crystals generally deviates from DL [see Eq. (2.4) for the condition of random orientation]. To the extent that D is related to L , the definition of D_e in Eq. (2.1), which is an approach to represent ice crystal size distribution, should be applicable to ice crystals with hexagonal structure. The numerator in Eq. (2.1) is related to the ice water content (IWC) in the form

$$IWC = \frac{3\sqrt{3}}{8} \rho_i \int_{L_{\min}}^{L_{\max}} D \cdot D L n(L) dL, \quad (2.2)$$

where the volume of a hexagonal ice crystal, $3 \sqrt{3} D^2 L / 8$, is used and ρ_i is the density of ice. We shall confine our study to the use of the mean effective size to represent ice crystal size distribution in the single-scattering calculation for ice crystals.

The extinction coefficient is defined by

$$\beta = \int_{L_{\min}}^{L_{\max}} \sigma(D, L) n(L) dL, \quad (2.3)$$

where σ is the extinction cross section for a single crystal. In the limits of geometric optics and using hexagonal ice crystals that are randomly oriented in space, the extinction cross section may be expressed by (Takano and Liou, 1989)

$$\sigma = \frac{3}{2} D \left[\frac{\sqrt{3}}{4} D + L \right]. \quad (2.4)$$

Substituting Eq. (2.4) into Eq. (2.3) and using the definitions of D_0 and IWC, we have

$$\beta = IWC \cdot \left[\frac{1}{\rho_i} \int_{L_{\min}}^{L_{\max}} D^2 n(L) dL / \int_{L_{\min}}^{L_{\max}} D^2 L n(L) dL + \frac{4}{\sqrt{3} \rho_i} \frac{1}{D_0} \right]. \quad (2.5a)$$

The first term on the right cannot be defined in terms of D_0 directly. However, since $D < L$, this term should be much smaller than the second term, which also involves a factor $4/\sqrt{3}$. To the extent that D is related to L , the first term may be approximated by $a + b'/D_0$, where $b' \ll 4/\sqrt{3}\rho_i$ and a is a certain constant. Using this argument, we obtain the following relationship:

$$\beta \cong IWC(a + b/D_0), \quad (2.5b)$$

where $b = b' + 4/\sqrt{3}\rho_i$. Using the observed ice crystal size distributions described below, we also show that β/IWC and $1/D_0$ are linearly related in the

solar spectral region. Based on the preceding analysis, it is clear that the extinction coefficient is a function of both IWC and mean effective size.

Because cloud absorption is critically dependent on the variation of the single-scattering albedo, it must be accurately parameterized. For a given ice crystal size distribution, the single-scattering albedo, $\bar{\omega}$, is defined by

$$1 - \bar{\omega} = \frac{\int_{L_{\min}}^{L_{\max}} \sigma_a n(L) dL}{\int_{L_{\min}}^{L_{\max}} \sigma n(L) dL}, \quad (2.6)$$

where σ_a denotes the absorption cross section for a single crystal. When absorption is small, σ_a is approximately equal to the product of the imaginary part of the refractive index of ice, m_i , and the particle volume, viz.,

$$\sigma_a = \frac{3\sqrt{3} \pi m_i(\lambda)}{2\lambda} D^2 L, \quad (2.7)$$

where λ is the wavelength. Using the extinction and absorption cross sections defined in Eqs. (2.4) and (2.7) and noting that D is related to L , based on observations, we obtain

$$1 - \bar{\omega} \approx c + dD, \quad (2.8)$$

where c and d are certain coefficients.

In the preceding discussion, we have used the geometric optics limit to derive the expressions for the extinction coefficient and single-scattering albedo. In view of the observed ice crystal sizes in cirrus clouds (~ 20 - $2000 \mu\text{m}$), the simple linear relationships denoted in Eqs. (2.5b) and (2.8) should be valid for solar wavelengths (0.2 - $4 \mu\text{m}$). For thermal infrared wavelengths (e.g., $10 \mu\text{m}$), the geometric optics approximation may not be appropriate for small ice crystals. However, we note from aircraft observations that there is a good linear relationship between the extinction coefficient in the infrared spectrum and the extinction coefficient derived based upon the large-particle approximation (Foot, 1988).

b. A Generalized Parameterization

The linear relationship between β/IWC and $1/D_0$, shown in Eq. (2.5b) is derived based on the geometric optics approximation and the assumption that ice crystals are randomly oriented in space. The linear relationship between $\bar{\omega}$ and D_0 , shown in Eq. (2.8) is based on the assumption that ice crystal absorption is small and that ice crystals are randomly oriented. For general cases, we would expect that higher-order expansions may be needed to define more precisely the single-scattering properties of ice crystals in terms of the mean effective size. Thus we postulate that

$$\beta = \text{IWC} \cdot \sum_{n=0}^N a_n / D_0^n, \quad (2.9)$$

$$1 - \bar{\omega} = \sum_{n=0}^N b_n D_0^n, \quad (2.10)$$

where a_n and b_n are certain coefficients, which must be determined from numerical fitting, and N is the total number of terms required to achieve a prescribed accuracy. When $N=1$, Eqs. (2.9) and (2.10) are exactly the same as Eqs. (2.5b) and (2.8). When $N=2$, the term, $1/D_0^2$ is proportional to the variance of ice crystal size distribution. Based on numerical experimentation described in subsection c, we find $N=2$ is sufficient for the extinction coefficient expression to achieve an accuracy within 1%. For the single-scattering albedo, we find that $N=3$ is required.

For nonspherical particles randomly oriented in space, the phase function is a function of the scattering angle, θ . The phase function is usually expanded in a series of Legendre polynomials P_l in radiative transfer calculations in the form

$$P(\cos \theta) = \sum_{l=0}^M \bar{\omega}_l P_l(\cos \theta), \quad (2.11)$$

where we set $\bar{\omega}_0 = 1$. Since the phase function is dependent on ice crystal size distribution, the expansion coefficients must also be related to ice crystal size

distribution, which is represented by the mean effective size in the present study. In the case of hexagonal ice crystals, in addition to the diffraction, scattered energy is also produced by the δ -function transmission through parallel planes at $\theta = 0$ (Takano and Liou, 1989). Using the similarity principle for radiative transfer, the expansion coefficients in the context of four-stream approximation can be expressed by

$$\bar{\omega}_l = (1 - f_\delta) \bar{\omega}_l^* + f_\delta (2l + 1), \quad l = 1, 2, 3, 4, \quad (2.12)$$

where $\bar{\omega}_l^*$ represents the expansion coefficients for the phase function in which the forward δ -function peak has been removed, and f_δ is the contribution from the forward δ -function peak. In our notation, $\bar{\omega}_1 = 3g$, where g is the asymmetry factor. The δ -function peak contribution has been evaluated by Takano and Liou and is a function of ice crystal size. The f_δ value increases with increasing L/D value due to a greater probability for plane-parallel transmission. We may express $\bar{\omega}_l^*$ and f_δ in terms of the mean effective size as follows:

$$\bar{\omega}_l^* = \sum_{n=0}^N c_{n,l} D_e^n, \quad (2.13a)$$

$$f_\delta = \sum_{n=0}^N d_n D_e^n, \quad (2.13b)$$

where $c_{n,l}$ and d_n are certain coefficients. Based on numerical experimentation described in subsection c, we find $N=3$ is sufficient to achieve an accuracy within 1%.

In the thermal infrared wavelengths, halo and δ -transmission peak features in the phase function are largely suppressed due to strong absorption. For this reason and to a good approximation, we may use the asymmetry factor to represent the phase function via the Henyey-Greenstein function in the form

$$\bar{\omega}_l = (2l + 1) g^l. \quad (2.14)$$

The asymmetry factor may also be expressed in terms of the effective mean size as follows:

$$g(\text{IR}) = \sum_{n=0}^N c'_n D_e^n, \quad (2.15)$$

where c'_n again is a certain coefficient and $N=3$ is sufficient in the expansion.

c. Determination of the Coefficients in the Parameterization

The coefficients in Eqs. (2.9), (2.10), (2.13), and (2.15) are determined from numerical fitting to the data computed from "exact" light scattering and absorption programs that include the following. For size parameters larger than about 30, we use the results computed from a geometric ray-tracing program for hexagonal ice crystals developed by Takano and Liou (1989). Note that the parameterization coefficients may be updated if the results for other types of ice crystals, such as bullet rosettes and hollow columns, are available. For size parameters less than about 30, the laws of geometric optics are generally not applicable. Since the exact solution for hexagonal ice crystals based on either the wave equation approach or other integral methods for size parameters on the order of 20-30 has not been developed, we use the results computed from a light scattering program for spheroids developed by Asano and Sato (1980). We have tested and modified this program (Takano et al., 1992) and found that it can be applied to size parameters less than about 30. Naturally occurring ice crystals will have a hexagonal structure that cannot be approximated by spheroids. However, small size parameters are usually associated with infrared wavelengths, where ice is highly absorbing. It is likely that the detailed shape factor may not be critical in scattering and absorption calculations. Further inquiry into this problem appears necessary.

In the present "exact" computations, 11 ice crystal size distributions from in-situ aircraft observations were employed. Table 1 shows the number densities,

IWCs, and mean effective sizes for these 11 size distributions. The first two types are for the cirrostratus (Cs) and cirrus uncinus presented by Heymsfield (1975), while the next two types are modified distributions given by Heymsfield and Platt (1984) corresponding to warm and cold cirrus clouds. The size distributions of cirrus clouds at temperatures of -20 , -40 , and -60°C were obtained from the parameterization results presented by Heymsfield and Platt (1984). Other cirrus types, Ci (Oct. 22, Oct. 25, Nov. 1, and Nov. 2), were the ice crystal size distributions derived from the 1986 FIRE cirrus experiments (Heymsfield, personal communication). The 11 size distributions cover a reasonable range of cloud microphysical properties in terms of IWC (6.6×10^{-4} - 0.11 gm^{-3}) and mean effective size (23.9 - $123.6 \mu\text{m}$) as shown in Table 1. For scattering and absorption calculations, these size distributions have been discretized in five regions. The aspect ratios, L/D, used are 20/20, 50/40, 120/60, 300/100, and 750/160 in units of $\mu\text{m}/\mu\text{m}$, roughly corresponding to the observations reported by Ono (1969) and Auer and Veal (1970).

In the single-scattering calculations, the refractive indices for ice, compiled by Warren (1984), were used. In order to resolve the variation in the refractive index of ice and account for the gaseous absorption, six and 12 bands were selected for solar and thermal IR regions, respectively. The spectral division is shown in Table 2, where the index for the spectral band ($i = 1, 2, \dots, 18$) is defined. The complex indices of refraction at each wavelength are averaged values over the spectral band, weighted by the solar irradiance (Thekaekara, 1973) in solar spectrum and by the Planck function ($T = -40^{\circ}\text{C}$) in thermal IR spectrum. This temperature is a typical value for cirrus clouds. The single-scattering calculations were carried out at the central wavelength for each spectral band. The coefficients in Eqs. (2.9), (2.10), (2.13), and (2.15) determined by numerical fitting using the "exact" results are listed in Tables 3-5. In the solar spectrum where the law of geometric optics is valid, the

extinction coefficients β for a given size distribution are the same regardless of the wavelength, as shown in Table 3. The optical depth $\tau = \beta\Delta z$ can be obtained if the cloud thickness Δz is given. Figures 1-2 show the fitting for β/IWC , $\bar{\omega}$ and g in the spectral intervals 1.9-2.5 μm and 800-980 cm^{-1} , respectively. For the solar spectrum, we use band number four (1.9-2.5 μm) as an example, because the single-scattering properties in this band significantly depend on size distribution. The linear relationship between β/IWC and $1/D_0$ postulated in Eq. (2.5b) is clearly shown in Fig. 1a. This linear relationship is valid for all other solar bands, because the extinction cross sections for solar bands in the limit of the geometric optics approach are the same, as pointed out previously. The nonlinearity between $\bar{\omega}$ and D_0 becomes important for small $\bar{\omega}$. This is because the linear relationship developed in Eq. (2.8) is based on the weak absorption assumption. The band 800-980 cm^{-1} is located in the atmospheric window, where the greenhouse effect of clouds is most pronounced. It can be seen that very good fits for single-scattering properties in both solar and infrared spectra are obtained. The relative errors are less than ~1%. Other spectral bands also show similar accuracies.

It is known that the minimum ice crystal length that the present optical probe can measure is about 20 μm . To investigate the potential effects of small ice crystals that may exist in cirrus clouds on parameterizations of the single-scattering properties, we used the 11 observed ice crystal size distributions and extrapolated these distributions from 20 to 10 μm in the logarithmic scale. The resulting mean effective sizes range from 18.9 to 122.7 μm . Using these sizes, the numerical fitting coefficients vary only slightly and do not affect the accuracy of the preceding parameterized single-scattering properties. In the present study, ice crystals are assumed to be randomly oriented in space. In cases when cirrus clouds contain horizontally oriented ice crystals, parameterizations would require modifications. The extinction coefficient,

single-scattering albedo and phase function would depend on the incident direction. The radiative transfer scheme would also require adjustments to account for anisotropic properties. Since fluxes are involved in the parameterization, we anticipate that the modifications should not significantly affect the results and conclusions derived from this study. At any rate, this is an area requiring further research efforts.

3. Parameterization of Radiative Flux Transfer

a. Radiative Transfer Scheme

We follow the δ -four-stream model developed by Liou et al. (1988) for the calculations of solar radiative flux transfer in a single homogeneous layer. The solution, like various two-stream methods, is in analytic form so that the computational effort involved is minimal. As demonstrated in that paper, results from the δ -four-stream approximation can yield relative accuracies within -5%.

To obtain a single treatment of solar and infrared radiation, we extend the δ -four-stream approach to the transfer of infrared radiation, in which the optical depth dependence of the Planck function must be known. The Planck function can be approximately expressed in terms of the optical depth in the form

$$B(\tau) = B_0 \exp(\tau/\tau_1 \ln B_1/B_0), \quad (3.1)$$

where τ_1 is the optical depth of a layer, and B_0 and B_1 are the Planck functions corresponding to the temperature at the top and bottom of this layer, respectively. This exponential approximation for the Planck function in optical depth has an accuracy similar to the linear approximation for the Planck function developed by Wiscombe (1976). Since the direct solar radiation source has an exponential function form in terms of optical depth, the formulation of the δ -four-stream approximation for infrared wavelengths is the same as that for solar wavelengths. For this reason, the computer program is simplified and the computational speed is enhanced.

In the limit of pure molecular absorption at infrared wavelengths, τ_1 may approach zero for some bands. The major advantage of using Eq. (3.1) is that the solution of the transfer equation is numerically stable when $\tau_1 \rightarrow 0$. If the linear approximation in τ is used, the round-off error may lead to an unstable solution when τ_1 is very small. We note that the higher order polynomial approximation in τ for the Planck function can also lead to an unstable solution. As in the case of solar wavelengths, we perform relative accuracy checks for infrared wavelengths with respect to "exact" results computed from the adding method for radiative transfer (Liou, 1992). Numerical results reveal that the errors in the δ -four-stream scheme in computing IR cloud emissivity are typically less than 1%. Systematic equations for this scheme that are required in numerical calculations are given in the Appendix.

For applications of the δ -four-stream scheme to nonhomogeneous atmospheres, the atmosphere is divided into N homogeneous layers with respect to the single-scattering albedo and phase function. The $4 \times N$ unknown coefficients in the analytic solution for the transfer equation are determined following the procedure described in Liou (1975). A numerically stable program has been developed to solve the system of linear equations by utilizing the property that the coefficient matrix is a sparse matrix. While this method is similar to the Gaussian elimination method with back substitution, it is carefully optimized so as to minimize the mathematical operations. We perform partial pivoting (interchanging rows only) to guarantee that a solution always exists. In order to avoid a fatal overflow problem, we follow the scaling technique developed by Stammes and Conklin (1984) so that numerical solutions can be carried out for large optical depths. Numerical problems that may occur when the single-scattering albedo $\tilde{\omega} = 0$ or 1 are also resolved in the present program. Using results from the adding method as a reference, errors in the δ -four-stream scheme for the nonhomogeneous multilayer cases remain within $\sim 5\%$. Transfer of infrared

radiation has not been treated satisfactorily by the two-stream techniques, because they do not produce reliable results in the limit of no scattering. This problem is circumvented in the present algorithm by using the "double Gauss" quadrature (Sykes, 1951), which produces a correct relation between the flux and intensity from an isotropic source.

Using the δ -four-stream scheme along with the parameterized single-scattering properties reported in Section 2, we calculate the solar reflectance and transmittance properties for typical ice clouds with different thicknesses and solar zenith angles. These properties are defined by $r = \sum_i r_i w_i$ and $t = \sum_i t_i w_i$ where r_i and t_i denote the reflectance and transmittance (direct plus diffuse) for an individual band, and w_i is the fraction of solar flux in the band. The relative errors are examined with respect to the "exact" results computed from the adding method using the "exact" phase function. Using C_1 (Nov. 1) as an example, Figs. 3a and 3b show the "exact" reflectance and transmittance, respectively, and Figs. 3c and 3d show the corresponding percentage errors in the δ -four-stream scheme for reflectance and transmittance. The δ -four-stream results in most cases achieve relative accuracies within $\sim 5\%$. The errors shown in Figs. 3c and 3d contain not only errors due to the δ -four-stream approximation, but also errors produced by the parameterized single-scattering properties for ice clouds. Generally, errors produced by the latter effect are much smaller ($< 1\%$).

b. Parameterizations of Nongray Gaseous Absorption

In each band shown in Table 2, the scattering properties, solar irradiance, and Planck functions may be treated as constant. In the solar spectrum, absorption due to H_2O ($2500-14500 \text{ cm}^{-1}$), O_3 (in the ultraviolet and visible), CO_2 ($2850-5250 \text{ cm}^{-1}$), and O_2 (A, B, and γ bands) is accounted for in the parameterization. In the infrared spectrum, we include the major absorption bands of H_2O ($0-2200 \text{ cm}^{-1}$), CO_2 ($540-800 \text{ cm}^{-1}$), O_3 ($980-1100 \text{ cm}^{-1}$), CH_4 ($1100-1400$

cm^{-1}), and N_2O ($1100\text{-}1400\text{ cm}^{-1}$). The continuum absorption of H_2O is incorporated in the spectral region $280\text{-}1250\text{ cm}^{-1}$.

Nongray gaseous absorption is incorporated into the δ -four-stream scheme based on the correlated k-distribution method developed by Fu and Liou (1992). In this method, the cumulative probability, g , of the absorption coefficient, k_ν , in a spectral interval $\Delta\nu$ is used to replace frequency, ν , as an independent variable. This leads to an immense numerical simplification, in which about ten thousand frequency intervals can be replaced by a few g intervals. With the required accuracy of $\sim 1\%$, we find that the minimum number of quadrature points in the g space ranges from one to about ten for different absorbing gases in different spectral regions. In order to treat overlapping of CO_2 and H_2O absorption, the correlated k-distribution has been formulated for a single mixture gas to economize the computational time. Using a minimum number of g intervals to represent the gaseous absorption and to treat overlap within each spectral interval, 121 spectral calculations are required for each vertical profile.

In the correlated k-distribution method, the vertical nonhomogeneity of the atmosphere is accounted for by assuming a simple correlation of k-distribution at different temperatures and pressures. The accuracy of the δ -four-stream scheme coupled with the parameterization program for nongray gaseous absorption has been examined with respect to results computed from a line-by-line program. Shown in Fig. 4a is a comparison of IR cooling rates using the midlatitude summer profile when all the constituents are included in the calculations. A maximum heating rate difference of 0.08 K/day occurs in the troposphere. The errors in the calculated flux are within 0.3% . Figure 4b shows a comparison of solar heating rates due to water vapor for different solar zenith angles. The errors in heating rates are less than 0.05 K/day . The errors in total atmospheric absorption and downward surface fluxes are generally less than 0.5% .

c. Molecular Scattering

The average extinction coefficient due to molecular scattering for a given band may be expressed as (Slingo and Schrecker, 1982)

$$\beta = R p/T, \quad (3.2)$$

where p is pressure (mb), T is temperature (K), and β is in units of m^{-1} . The coefficients R for the six bands in the solar spectrum are 9.022×10^{-6} , 5.282×10^{-7} , 5.722×10^{-8} , 1.433×10^{-8} , 4.526×10^{-9} , and 1.529×10^{-9} .

For Rayleigh scattering, the single-scattering albedo is 1. The phase function $P(\cos \theta) = 3/4(1 + \cos^2 \theta)$, so that the expansion coefficients $\bar{\omega}_1 = 0$, $\bar{\omega}_2 = 1/2$, and $\bar{\omega}_l = 0$, where $l \geq 3$.

d. Single-Scattering Properties for Combined Cloud Particles and Gases

Consider a nonhomogeneous atmosphere which is divided into N homogeneous layers. For the case when both Rayleigh scattering and extinction by cloud particles are mixed with gaseous absorption, the total optical depth for each layer is

$$\Delta\tau(g) = \Delta\tau^R + \Delta\tau^M + \Delta\tau^G(g), \quad (3.3)$$

where $\Delta\tau^R$ and $\Delta\tau^M$ represent the optical depth due to Rayleigh molecules and cloud particles, respectively. $\Delta\tau^G(g)$ is the optical depth contributed by the gaseous absorption for a given g (the cumulative probability), which can be expressed by

$$\Delta\tau^G(g) = k(g,p,T)\rho\Delta z, \quad (3.4)$$

where $k(g,p,T)$ is the equivalent k -function (Fu and Liou, 1992), ρ is the density of the absorber, and Δz is the geometric thickness of the layer. In this case, $\Delta\tau^M = \Delta\tau_s^M + \Delta\tau_a^M$, where $\Delta\tau_s^M$ and $\Delta\tau_a^M$ are cloud scattering and absorption optical depths, respectively. Thus, the combined single-scattering albedo and the expansion coefficients for the phase function can be obtained by

$$\bar{\omega}(g) = \frac{\Delta\tau^R + \Delta\tau_s^M}{\Delta\tau^R + \Delta\tau^M + \Delta\tau^G(g)}, \quad (3.5)$$

$$\bar{\omega}_l = \frac{\Delta\tau_s^{M-M} + \Delta\tau^R \bar{\omega}_l^R}{\Delta\tau_s^M + \Delta\tau^R}, \quad (3.6)$$

where $\bar{\omega}_l^M$ and $\bar{\omega}_l^R$ denote the expansion coefficients for the phase function for cloud particles and Rayleigh molecules, respectively. Since the phase function is independent of gaseous absorption, the combined $\bar{\omega}_l$ is constant over a given spectral absorption band. Once the single-scattering properties have been defined for a given g for each level, monochromatic radiative transfer calculations may be carried out, and the total flux over each spectral band can be obtained by integrating the flux solution in the g space. As described in Section 3(b), a number of intervals are used for the g -quadrature, which are sufficient to confine the integration errors within 1%.

4. Comparisons with Observations

Recently, the cirrus intensive field observation (IFO) was conducted in Wisconsin, from 13 October to 2 November 1986, as a major component of the First ISCCP Regional Experiment (FIRE) to improve our understanding of cirrus clouds and their influence on weather and climate processes (Starr, 1987). In cirrus IFO, the microphysical measurements were simultaneously obtained along with radiation measurements by using high altitude research aircraft. This allows comparisons to be made between model calculations and in-situ observations. In this section we present comparisons of model derived infrared emissivity and solar albedo with those obtained from the NCAR Sabreliner on 28 October 1986.

The Sabreliner was flown near the western shore of Lake Michigan in the vicinity of Green Bay, Wisconsin, in a thin banded cirrus layer, between 1530 and 1630 UTC (0930-1030 local time). The cloud top and base heights were about 11.1 and 8.9 km, respectively. A racetrack pattern was flown at six different levels

throughout the cirrus. The mean solar zenith angle during the flight was 61.3°. Since radiative and microphysical characteristics of the cloud sampled on the south side of the racetrack (referred to as cloud 1) are different from those sampled on the north side (referred to as cloud 2), the data from each side were analyzed separately. Furthermore, each side of the racetrack pattern was divided into thinner, mean, and thicker cases to minimize the sampling error. Details of the description of the observations and data analysis procedure have been given by Smith et al. (1990), and Heymsfield et al. (1990).

The effective upward emissivity ϵ^\uparrow and downward emissivity ϵ^\downarrow involving a nonblack cloud may be defined as (Paltridge and Platt, 1981)

$$\epsilon^\uparrow = \frac{F_L^\uparrow(z_t) - F_L^\uparrow(z_b)}{\sigma \bar{T}^4 - F_L^\uparrow(z_b)}, \quad (4.1)$$

and

$$\epsilon^\downarrow = \frac{F_L^\downarrow(z_b) - F_L^\downarrow(z_t)}{\sigma \bar{T}^4 - F_L^\downarrow(z_t)}, \quad (4.2)$$

where F_L^\uparrow and F_L^\downarrow are the infrared broadband upward and downward fluxes, z_t and z_b are the cloud top and base heights, and \bar{T} is the mean cloud temperature. $\sigma \bar{T}^4$ is the flux emitted by a blackbody at \bar{T} .

The solar albedo may be defined as (Paltridge and Platt, 1981)

$$\alpha = \frac{F_S^\downarrow(z_t)(1-a) - F_S^\downarrow(z_b)}{F_S^\uparrow(z_t) - F_S^\uparrow(z_b)}, \quad (4.3)$$

where

$$a = \frac{[F_S^\downarrow(z_t) - F_S^\uparrow(z_t)] - [F_S^\downarrow(z_b) - F_S^\uparrow(z_b)]}{F_S^\uparrow(z_t) + F_S^\uparrow(z_b)}. \quad (4.4)$$

In these equations, F_S is the solar broadband flux.

ϵ^\uparrow , ϵ^\downarrow , and α were derived from broadband flux observations by Stackhouse and Stephens (1991) for the 28 October 1986 FIRE case, which are shown in Figs. 5a-c as a function of the ice water path (IWP), defined as $IWC \cdot \Delta z$. The error

bars through these observation points denote the uncertainties of the observation. The theoretical results are displayed in these figures for comparisons. In the calculations, atmospheric temperature and moisture profiles were averaged over the two soundings from Green Bay at 1400 and 1730 UTC. For CO_2 , CH_4 , and N_2O , uniform mixings were assumed throughout the atmosphere with concentrations of 330, 1.6, and 0.28 ppmv, respectively. The ozone profile and the temperature and moisture profiles above sounding were assumed to be those of the US Standard Atmosphere. The cloud was positioned between 8.9 and 11.1 km and the IWP was varied by changing the assumed IWC but keeping the cloud position fixed. Ice saturation mixing ratio was assumed in the cloud. In the computations, the mean effective sizes of 25, 50, 75, 100, and 125 μm were used, corresponding to five solid lines for ϵ^{\uparrow} , ϵ^{\downarrow} , and α in Figs. 5a-c. For solar radiation, the solar zenith angle used was 61.3° and surface albedo was assumed to be 0.072 (Stackhouse and Stephens, 1991). Comparing the theoretical results to observed data, we find that the mean effective sizes of these cases lie in the range of $-50 - -100 \mu\text{m}$ for ϵ^{\uparrow} and ϵ^{\downarrow} , and $-50 - -75 \mu\text{m}$ for α . The mean effective size for ϵ^{\uparrow} and ϵ^{\downarrow} in each case appears to be consistent in view of the observational uncertainties. However, the mean effective size associated with solar albedo is smaller than that associated with effective emissivity. This difference can be explained by the fact that solar albedo is more sensitive to the size spectra at the cloud top. Based on observations (Heymsfield et al., 1990), ice crystals progressively range from smaller sizes near the cloud top to larger sizes at the base of the cloud. For the same cloud, e.g., cloud 1, Fig. 5 shows that D_0 increases as IWP increases. This is expected because larger IWC is usually correlated with larger particle size. As given by Eqs. (4.1) and (4.2), the effective emissivities are defined in terms of fluxes that contain components due to scattering of cloud particles and absorption of gases, principally water vapor. For this reason, the computed effective emissivities

may exceed 1 when IWP is large, and may deviate from 0 when $IWP \rightarrow 0$. Figure 5d illustrates the plot of solar albedo vs. effective downward emissivity for a number of mean effective sizes. The observed data derived from the 28 October 1986 FIRE case are also displayed. In the domain of albedo-emissivity, the effect of ice crystal size distribution is fairly small. Reasonable agreements are shown between the theoretical results and observations.

We also calculate the emissivity of cloud particles alone by using the δ -four-stream scheme with the parameterized single-scattering properties described in Section 2. The results are compared with those derived by Smith et al. (1990) for the 28 October 1986 FIRE case in Fig. 6, where each pair of observed points represents the emittance from the top layer of the cloud and the emittance of the entire cloud layer. Smith et al. utilized a broadband infrared radiative transfer model (Cox and Griffith, 1979) to isolate the emissivity of ice particles by using observed downward infrared fluxes. From this comparison (Fig. 6), we find that the average D_e of the entire cloud layer is in agreement with the value derived from Fig. 5a for each case. Figure 6 also shows that the averaged mean effective size in the upper layer of the cloud is generally smaller than that of the entire cloud layer. From Fig. 6, we note that the line for the D_e of 25 μm crosses the 50 μm line. This is because a smaller D_e produces larger reflectivity, r . When the optical depth $\tau \rightarrow \infty$, the emissivity $\epsilon = 1 - r$ would be smaller.

From Figs. 5 and 6, the estimated D_e ranges from ~50 to ~100 μm . Using aspect ratios of 2 for 50 μm and 3 for 100 μm , the effective maximum dimension (L_e) would be from ~100 to ~300 μm . Wielicki et al. (1990) estimated the median mass weighted maximum dimension (L_m) from Sabreliner observations to be ~75 to ~400 μm . The averaged L_m is ~238 μm . The averaged L_e from the present study is ~200 μm . Note that L_m and L_e represent volume and area weighted mean values.

Nevertheless, the computed L_e from the model appears to compare reasonably well with observed data.

In light of preceding discussion, the observed cloud emissivity and cloud albedo can be reasonably interpreted from the theoretical results, which used the scattering and absorption properties for hexagonal ice crystals (columns and plates). The actual ice crystals that were collected by the optical probe aboard the Sabreliner during the FIRE cirrus experiment were largely bullet rosettes, columns, plates, and compacted spatial particles (occasionally having extensions) (Heymsfield et al., 1990). Although the exact ice crystal shapes were not employed in the scattering and absorption calculations, the theoretical results account for the general hexagonal structure of ice particles and include accurate flux calculations. This, perhaps, explains some success of the present parameterization scheme in the interpretation of the observed data from aircraft. Past researchers frequently used area-equivalent spheres to interpret the observed radiative properties of cirrus (see, e.g., Stackhouse and Stephens, 1991). Since equivalent spheres scatter more light in forward directions and have smaller single-scattering albedo than nonspherical ice crystals, the assumption that ice particles are spheres would lead to an underestimation of the solar albedo of cirrus clouds (Kinne and Liou, 1989). Increasing the amount of small spherical ice crystals has not led to a better interpretation of the radiative properties of cirrus clouds. Finally, it should be pointed out that further verification of theoretical results would require narrowing the large experimental uncertainties that are related to radiation and microphysical measurements.

Finally, we examine the relationship for the emissivity of cirrus clouds as a function of the optical depth at $0.55 \mu\text{m}$. Using the present model, a number of emissivities were computed for the 11 observed cirrus cloud types (Table 1) with cloud thicknesses of 0.5, 1, 2 and 4 km. The results are plotted in Fig.

7 as a function of the optical depth. The solid line on the diagram is the least square curve using the function

$$\epsilon = 1 - \exp(-a\tau), \quad (4.5)$$

where τ is the visible optical depth. The fitted coefficient a is 0.79. Using a diffusivity factor of 1.66, the visible optical depth is related to the infrared optical depth (due to absorption) by a factor of 2.1. This result agrees with the observed result reported by Platt et al. (1987), who showed that the ratio of visible extinction to infrared absorption varies from -1.8 to 2.3 for the midlatitude cirrus clouds. Note that the 11 size distributions used in the present study cover a spectrum of ice crystal size spectra that occur in midlatitude cirrus clouds.

5. The Radiative Effects of Ice Crystal Size Distributions

The importance of cirrus clouds on the radiative budget of the earth and the atmosphere has been documented by Liou (1986). Ackerman et al. (1988) have further carried out an investigation regarding the interaction of infrared and solar radiation with tropical cirrus anvils. They find that the radiative effects of cirrus clouds are very sensitive to the assumed ice water content, the cloud thickness, and the environmental conditions in which the clouds form. However, their study was confined to cirrus clouds with a fixed size distribution. In this study, we examine the effects of ice crystal size distributions on the radiative heating and budget using the radiative transfer model developed in the preceding sections. In the present calculations, standard atmospheric temperature, water vapor and ozone profiles are used. The cirrus cloud layer is inserted in the atmosphere between 9 and 11 km. For water vapor within the cloud layer, the ice saturation mixing ratio is assumed. To compute solar fluxes, a solar constant of 1365 Wm^{-2} , a surface albedo of 0.1, a solar zenith angle of 60° , and a 12 h solar day are used. The computations are carried

out by using the mean effective sizes, D_e , of 25, 50, 75, 100, and 125 μm , which cover the range of D_e from observations.

a. Heating Rate

The effects of the ice crystal mean effective size on IR, solar and net (IR + solar) radiative heating rates in the cloud are illustrated in Figs. 8a, 8b, and 8c, respectively. The IWP used is 30 g m^{-2} , which corresponds to an IWC of 0.015 g m^{-3} . In the calculations, the vertical layer thickness is set to be 250 m and the heating rates are layer averages. For the smallest D_e (25 μm), IR heating/cooling rates of about 30 K/day take place close to the bottom and top of the cloud layer. Such large differential heating rates between cloud bottom and top ($\sim 60 \text{ K/day}$) would have a significant effect on both the entrainment and cloud microphysics (Ackerman et al., 1983). For the largest D_e of 125 μm , the IR heating/cooling rates at the cloud bottom and top reduce by as much as a factor of 10. A cloud consisting of smaller D_e emits more IR radiation at the cloud top, resulting in strong cooling. The cloud absorbs, at the same time, more IR radiation emitted from the warmer surface and atmosphere below, resulting in strong heating at the cloud base region. If IWC is fixed, a cloud containing smaller D_e would have larger emittance/absorptance because of larger cross sectional area. The solar heating rate peaks at the cloud top and reaches a value of $\sim 5 \text{ K/day}$ for D_e of 25 μm . The net heating rates due to both IR and solar radiation in the cloud are shown in Fig. 8c. It is evident that the cloud heating rate field is largely controlled by IR radiation and that smaller D_e can produce larger radiative heating gradients.

For a given ice crystal size distribution, larger IWC generates a stronger radiative heating gradient, as demonstrated by Ackerman et al. (1988). Based on the preceding discussion on the relation of D_e and heating rates, changes in the heating gradient due to the effects of D_e and IWC are thus in opposite directions. According to observations (e.g., Heymsfield et al., 1990), IWC

usually (if not always) increases with increasing ice crystal size. Therefore, the effects of IWC and D_0 on heating rates may partially be compensated for if both parameters are interactively included in the calculation.

b. Cloud Forcing

The ice crystal size distribution of cirrus clouds has a significant effect on the radiation budget of the earth and the atmosphere. To quantify this effect, we use the cloud radiative forcing concept (e.g., Hartmann et al., 1986) for the flux at the top of the atmosphere (TOA) and define the following:

$$C_{ir,s} = F_{ir,s}^{cl} - F_{ir,s}^{ov},$$

where *cl* and *ov* denote clear and overcast conditions, and F_{ir} and F_s are the upward IR and solar fluxes, respectively. The net cloud radiative forcing is

$$C = C_{ir} + C_s.$$

For partly cloudy conditions, if the cloud cover is denoted as η , the cloud radiative forcing is given by ηC .

Figures 9a-9c show the results of C_{ir} , C_s , and C as a function of IWP for different mean effective sizes. The IR cloud forcing C_{ir} (Fig. 9a) is always positive, corresponding to the heating of the earth-atmosphere system due to the greenhouse effect of clouds, while the solar cloud forcing C_s (Fig. 9b) is always negative, showing the cooling of the system by the cloud albedo effect. C_{ir} and C_s are strongly dependent on both IWP and D_0 . For an IWP of 30 g/m^2 , C_{ir} decreases from 131 to 54 W/m^2 as D_0 increases from 25 to $125 \text{ }\mu\text{m}$. The solar cloud forcing counterpart increases from -114 to -24 W/m^2 . The net cloud forcing (Fig. 9c) shows that cirrus clouds have a net heating effect on the system except for $\text{IWP} > 50 \text{ g m}^{-2}$ in the case when $D_0 = 25 \text{ }\mu\text{m}$. These results are similar to those derived from a climate model presented by Stephens et al. (1990).

Usually, small D_0 is associated with cold cirrus clouds that have small IWP. We may safely assume that midlatitude cirrus clouds would have positive

cloud forcing, i.e., the greenhouse effect produced by the presence of these clouds is more pronounced than the albedo effect. The net greenhouse effect is a function of both ice crystal size and IWP. The data points depicted in Fig. 9c are computed from the 10 observed ice crystal size distributions (except *Ci uncinus*, which has a IWP of -220 g/m^2) using a thickness of 2 km. The visible optical depths of these clouds range from about 0.15 to 1.5. Assuming a 20% cloud cover, the cloud forcing values generally range from about 4 to 8 W/m^2 . When coupled with positive radiative forcings, such as those due to the increase of greenhouse gases, feedbacks produced by the increase or decrease of cirrus clouds could be significant.

Finally, we investigate the cloud radiative forcing at the surface. Figures 10a and 10b show the IR and solar cloud forcing, respectively. In the latter case, the negative cloud forcing values produced by cloud reflection are substantially similar to those presented in Fig. 9b. This is because the atmosphere is largely transparent with respect to solar radiation when clouds are present. For the IR case, the insertion of cirrus clouds produces small effects at the surface ($0\text{-}30 \text{ W/m}^2$), because of the strong absorption of the atmosphere between the surface and the cloud in the infrared wavelengths. The cirrus cloud-induced IR heating within the atmosphere and solar cooling at the surface could have a significant impact on the atmospheric circulations and temperature distributions (Ramanathan, 1987; Slingo and Slingo, 1988).

6. Summary and Conclusions

In this paper, a new approach has been devised for the parameterization of radiative transfer in the atmosphere involving cirrus clouds. We use a mean effective size, representing ice crystal size distribution, in the development of parameterization for the single-scattering properties of ice crystals. The extinction coefficient, the single-scattering albedo, and the expansion

coefficients of the phase function for the 11 observed ice crystal size distributions have been computed from a geometric ray-tracing technique for hexagonal ice crystals (size parameter > 30) and Mie-type solution for spheroids (size parameter < 30). Using these results and basic physical reasonings, we develop simple polynomial relationships between the single-scattering properties and mean effective size that can achieve relative accuracies within $\sim 1\%$.

A δ -four-stream radiative transfer scheme has been developed for flux calculations in both solar and infrared spectra. With respect to the "exact" results computed from the adding method for radiative transfer, this scheme can yield relative accuracies within $\sim 5\%$ for all atmospheric conditions. For nongray gaseous absorptions due to H_2O , CO_2 , O_3 , CH_4 , and N_2O , we use the correlated k-distribution method to obtain a number of equivalent absorption coefficients. A total of 121 spectral calculations for each vertical profile in the entire spectrum is required. Compared with line-by-line calculations for clear midlatitude summer atmosphere, the δ -four-stream scheme coupled with the correlated k-distribution parameterization produces deviations less than 0.1 K/day in heating rates and within 0.5% in flux calculations. In the limit of no scattering, the δ -four-stream scheme can produce reliable results since the double Gauss quadrature provides a correct relation between the flux and intensity from an isotropic source. The computational time of the scheme is linear with respect to the number of vertical levels.

Comparisons have been carried out between theoretical calculations and aircraft measurements involving cloud emissivity and cloud albedo obtained during the cirrus FIRE IFO. The effect of ice crystal size distribution in terms of the mean effective size is important in the interpretation of the observed data. Further verification of the model results requires the reduction of large experimental uncertainties in both radiation and microphysical measurements.

We further investigate the effects of ice crystal size distributions on the radiative properties of the atmosphere involving cirrus clouds. For a given ice water path, cirrus clouds containing smaller mean effective sizes reflect more solar radiation, trap more thermal infrared, and produce strong cloud-top cooling and cloud-base heating. This pattern would enhance the in-cloud heating rate gradient, which could be significant in terms of cloud microphysical processes. For the observed midlatitude cirrus cases, the IR greenhouse effect outweighs the solar albedo effect. The degree of the greenhouse effect involving cirrus clouds is a function of cloud cover as well as the mean effective size and liquid water path. Assuming the presence within a sky field of 20% cirrus clouds, a gain of $-4-8 \text{ W/m}^2$ is obtained from the present calculation. With respect to the surface, the presence of cirrus clouds reduces the solar flux available to the surface. In this case, the solar albedo effect dominates the IR greenhouse effect, which is confined largely within the atmosphere.

There are a number of significant new features in the present radiative scheme. First, the ice crystal size distribution consisting of nonspherical particles is effectively accounted for in the parameterization of the single-scattering properties of cirrus clouds. This is especially important in the determination of the solar albedo of cirrus clouds. Second, the IR and solar radiation regions have been treated in a self-consistent fashion using the same parameterization scheme, which is essential to the investigation of the solar albedo versus IR greenhouse effects involving clouds. Third, the present model can efficiently compute the detailed vertical structure of the heating rate profile within clouds, which is critical to the understanding of the effects of radiation on cloud formation. The present parameterization for the radiative transfer in the atmosphere involving cirrus clouds is well suited for incorporation in numerical models to study the climatic effects of cirrus clouds,

as well as to investigate interactions and feedbacks between cloud microphysics and radiation.

Acknowledgments. The research work contained herein has been supported by AFOSR Grant 91-0039, NASA Grant NAG5-1050, and NSF Grant 90-24219. We thank Dr. Y. Takano for providing the single-scattering data that are used in the parameterization.

REFERENCES

- Ackerman, T.P., K.-N. Liou, F.P.J. Valero, and L. Pfister, 1988: Heating rates in tropical anvils. J. Atmos. Sci., 45, 1606-1623.
- Asano, S., and M. Sato, 1980: Light scattering by randomly oriented spheroidal particles. Appl. Opt., 19, 962-974.
- Auer, A.H., Jr., and D.L. Veal, 1970: The dimension of ice crystals in natural clouds. J. Atmos. Sci., 27, 919-926.
- Cox, S.K., and K.T. Griffith, 1979: Estimates of radiative divergence during phase III of the GARP Atlantic tropical experiment: Part I. Methodology. J. Atmos. Sci., 36, 576-585.
- Foot, J.S., 1988: Some observations of the optical properties of clouds. II: Cirrus. Quart. J. Roy. Meteor. Soc., 114, 145-164.
- Fu, Q., and K.N. Liou, 1992: On the correlated k-distribution method for radiative transfer in nonhomogeneous atmospheres. J. Atmos. Sci., 49, (November).
- Hansen, J.E., and L.D. Travis, 1974: Light scattering in planetary atmospheres. Space Sci. Rev., 16, 527-610.
- Hartmann, D.L., V. Ramanathan, A. Berroir, and G.E. Hunt, 1986: Earth radiation budget data and climate research. Rev. Geophys., 24, 439-468.
- Heymsfield, A.J., 1975: Cirrus uncinus generating cells and the evolution of cirriform clouds. J. Atmos. Sci., 32, 799-808.
- Heymsfield, A.J., and C.M.R. Platt, 1984: A parameterization of the particle size spectrum of ice clouds in terms of the ambient temperature and the ice water content. J. Atmos. Sci., 41, 846-855.
- Heymsfield, A.J., K.M. Miller, and J.D. Spinhirne, 1990: The 27-28 October 1986 FIRE IFO cirrus case study: Cloud microstructure. Mon. Wea. Rev., 118, 2313-2328.

- Kinne, S., and K.N. Liou, 1989: The effects of the nonsphericity and size distribution of ice crystals on the radiative properties of cirrus clouds. Atmos. Res., 24, 273-284.
- Liou, K.N., 1975: Applications of the discrete-ordinate method for radiative transfer to inhomogeneous aerosol atmospheres. J. Geophys. Res., 80, 3434-3440.
- Liou, K.N., 1986: Influence of cirrus clouds on weather and climate processes: A global perspective. Mon. Wea. Rev., 114, 1167-1199.
- Liou, K.N., 1992: Radiation and Cloud Processes in the Atmosphere: Theory, Observation, and Modeling. Oxford University Press, 487 pp.
- Liou, K.N., and G.D. Wittman, 1979: Parameterization of the radiative properties of clouds. J. Atmos. Sci., 36, 1261-1273.
- Liou, K.N., Q. Fu, and T.P. Ackerman, 1988: A simple formulation of the δ -four-stream approximation for radiative transfer parameterizations. J. Atmos. Sci., 45, 1940-1947.
- Ono, A., 1969: The shape and riming properties of ice crystals in natural clouds. J. Atmos. Sci., 26, 138-147.
- Paltridge, G.W., and C.M.R. Platt, 1981: Aircraft measurements of solar and infrared radiation and the microphysics of cirrus cloud. Quart. J. Roy. Meteor. Soc., 107, 367-380.
- Platt, C.M.R., and Harshvardhan, 1988: Temperature dependence of cirrus extinction: Implications for climate feedback. J. Geophys. Res., 93, 11051-11058.
- Platt, C.M.R., J.C. Scott, and A.C. Dilley, 1987: Remote sounding of high clouds. Part VI: Optical properties of midlatitude and tropical cirrus. J. Atmos. Sci., 44, 729-747.
- Ramanathan, V., 1987: The role of earth radiation budget studies in climate and general circulation research. J. Geophys. Res., 92, 4075-4095.

- Slingo, A., and H.M. Schrecker, 1982: On the shortwave radiative properties of stratiform water clouds. Quart. J. Roy. Meteor. Soc., 108, 407-426.
- Slingo, A., and J.M. Slingo, 1988: The response of a general circulation model to cloud longwave radiative forcing. I: Introduction and initial experiments. Quart. J. Roy. Meteor. Soc., 114, 1027-1062.
- Smith, Jr., W.L., P.F. Hein, and S.K. Cox, 1990: The 27-28 October 1986 FIRE IFO cirrus case study: In situ observations of radiation and dynamic properties of a cirrus cloud layer. Mon. Wea. Rev., 118, 2389-2401.
- Stackhouse, Jr., P.W., and G.L. Stephens, 1991: A theoretical and observational study of the radiative properties of cirrus: Results from FIRE 1986. J. Atmos. Sci., 48, 2044-2059.
- Stamnes, K., and P. Conklin, 1984: A new multi-layer discrete ordinate approach to radiative transfer in vertically inhomogeneous atmospheres. J. Quant. Spectrosc. Radiat. Transfer, 31, 273-282.
- Starr, D.O., 1987: A cirrus cloud experiment: Intensive field observations planned for FIRE. Bull. Amer. Meteor. Soc., 68, 119-124.
- Stephens, G.L., S.C. Tsay, P.W. Stackhouse, Jr., and P.J. Flatau, 1990: The relevance of the microphysical and radiative properties of cirrus clouds to climate and climate feedback. J. Atmos. Sci., 47, 1742-1753.
- Sykes, J.B., 1951: Approximate integration of the equation of transfer. Mon. Not. Roy. Astron. Soc., 111, 377-386.
- Takano, Y., and K.N. Liou, 1989: Solar radiative transfer in cirrus clouds. Part I: Single-scattering and optical properties of hexagonal ice crystals. J. Atmos. Sci., 46, 3-19.
- Takano, Y., K.N. Liou, and P. Minnis, 1992: The effects of small ice crystals on cirrus infrared radiative properties. J. Atmos. Sci., 49, 1487-1493.
- Thekaekara, M.P., 1973: Solar energy outside the earth's atmosphere. Solar Energy, 14, 109-127.

Warren, S.G., 1984: Optical constants of ice from ultraviolet to the microwave.

Appl. Opt., 23, 1206-1225.

Wielicki, B.A., J.T. Suttles, A.J. Heymsfield, R.M. Welch, J.D. Spinhirne, M.-

L.C. Wu, D. O'C. Starr, L. Parker, and R.F. Arduini, 1990: The 27-28

October 1986 FIRE IFO cirrus case study: Comparison of radiative transfer

theory with observations by satellite and aircraft. Mon. Wea. Rev., 118,

2356-2376.

Wiscombe, W.J., 1976: Extension of the doubling method to inhomogeneous

sources. J. Quant. Spectrosc. Radiat. Transfer, 16, 477-489.

Table 1. Characteristics of the 11 ice crystal size distributions employed in the present study.

Particle Size Distribution	Number of Particles (cm^{-3})	Ice Water Content (g m^{-3})	Mean Effective Size (μm)
Cs	0.187	4.765 e-3	41.5
Ci Uncinus	0.213	1.116 e-1	123.6
Ci (Cold)	0.176	1.110 e-3	23.9
Ci (Warm)	0.442	9.240 e-3	47.6
Ci (T=-20°C)	0.247	8.613 e-3	57.9
Ci (T=-40°C)	0.187	9.177 e-3	64.1
Ci (T=-60°C)	0.065	6.598 e-4	30.4
Ci (Oct. 22)	0.052	1.609 e-2	104.1
Ci (Oct. 25)	0.072	2.923 e-2	110.4
Ci (Nov. 1)	0.032	4.968 e-3	75.1
Ci (Nov. 2)	0.038	1.406 e-2	93.0

Table 2. Spectral division used in the parameterization.

Solar Spectrum			Infrared Spectrum		
Band i	Central λ (μm)	Band Limits (μm)	Band i	Central λ (μm)	Band Limits (cm^{-1})
1	0.55	0.2-0.7	7	4.9	2200-1900
2	1.0	0.7-1.3	8	5.6	1900-1700
3	1.6	1.3-1.9	9	6.5	1700-1400
4	2.2	1.9-2.5	10	7.6	1400-1250
5	3.0	2.5-3.5	11	8.5	1250-1100
6	3.7	3.5-4.0	12	9.6	1100-980
			13	11.3	980-800
			14	13.7	800-670
			15	16.6	670-540
			16	21.5	540-400
			17	30.0	400-280
			18	70.0	280-10

Table 3. Values of empirical coefficients in Eq. (2.9)* for the parameterization of the extinction coefficient $\beta(\text{m}^{-1})$. Note that the coefficients are determined by using an ice density ρ_i of 0.9167 g cm^{-3} . For other ice densities ρ_i^* , they should be adjusted by a factor ρ_i/ρ_i^* .

Band i	a_0	a_1	a_2
1 - 6	-6.656e-3	3.686	0.0
7	-7.770e-3	3.734	11.85
8	-8.088e-3	3.717	17.17
9	-8.441e-3	3.715	19.48
10	-9.061e-3	3.741	26.48
11	-9.609e-3	3.768	34.11
12	-1.153e-2	4.109	17.32
13	-8.294e-3	3.925	1.315
14	-1.026e-2	4.105	16.36
15	-1.151e-2	4.182	31.13
16	-1.704e-2	4.830	16.27
17	-1.741e-2	5.541	-58.42
18	-7.752e-3	4.624	-42.01

*The units for D_0 and IWC are in μm and g m^{-3} , respectively.

Table 4. Values of empirical coefficients in Eq. (2.10)* for the parameterization of the single-scattering albedo ω .

Band i	b_0	b_1	b_2	b_3
1	.10998E-05	-.26101E-07	.10896E-08	-.47387E-11
2	.20208E-04	.96483E-05	.83009E-07	-.32217E-09
3	.13590E-03	.73453E-03	.28281E-05	-.18272E-07
4	-.16598E-02	.20933E-02	-.13977E-05	-.18703E-07
5	.46180E+00	.24471E-03	-.27839E-05	.10379E-07
6	.42362E-01	.86425E-02	-.75519E-04	.24056E-06
7	.19960	.37800E-02	-.14910E-04	.0
8	.30140	.26390E-02	-.11160E-04	.0
9	.39080	.12720E-02	-.55640E-05	.0
10	.31050	.26030E-02	-.11390E-04	.0
11	.20370	.42470E-02	-.18100E-04	.0
12	.23070	.38300E-02	-.16160E-04	.0
13	.56310	-.14340E-02	.62980E-05	.0
14	.52070	-.97780E-03	.37250E-05	.0
15	.32540	.34340E-02	-.30810E-04	.91430E-07
16	.10280	.50190E-02	-.20240E-04	.0
17	.39640	-.31550E-02	.64170E-04	-.29790E-06
18	.80790	-.70040E-02	.52090E-04	-.14250E-06

*The units for D_0 are in μm .

Table 5a. Values of empirical coefficients in Eq. (2.13)* for parameterization of the expansion coefficients for the phase function in the solar wavelengths.

Band i	ℓ	$c_{0,\ell}$	$c_{1,\ell}$	$c_{2,\ell}$	$c_{3,\ell}$
1	1	.22110E+01	-.10398E-02	.65199E-04	-.34498E-06
	2	.32201E+01	.94227E-03	.80947E-04	-.47428E-06
	3	.41610E+01	.74396E-03	.82690E-04	-.45251E-06
	4	.51379E+01	.51545E-02	.11881E-04	-.15556E-06
2	1	.22151E+01	-.77982E-03	.63750E-04	-.34466E-06
	2	.31727E+01	.15597E-02	.82021E-04	-.49665E-06
	3	.40672E+01	.25800E-02	.71550E-04	-.43051E-06
	4	.49882E+01	.86489E-02	-.18318E-04	-.59275E-07
3	1	.22376E+01	.10293E-02	.50842E-04	-.30135E-06
	2	.31549E+01	.47115E-02	.70684E-04	-.47622E-06
	3	.39917E+01	.82830E-02	.53927E-04	-.41778E-06
	4	.48496E+01	.15998E-01	-.39320E-04	-.43862E-07
4	1	.23012E+01	.33854E-02	.23528E-04	-.20068E-06
	2	.31730E+01	.93439E-02	.36367E-04	-.38390E-06
	3	.39298E+01	.16424E-01	.10502E-04	-.35086E-06
	4	.47226E+01	.25872E-01	-.77542E-04	-.21999E-07
5	1	.27975E+01	.29741E-02	-.32344E-04	.11636E-06
	2	.43532E+01	.11234E-01	-.12081E-03	.43435E-06
	3	.56835E+01	.24681E-01	-.26480E-03	.95314E-06
	4	.68271E+01	.42788E-01	-.45615E-03	.16368E-05
6	1	.19655E+01	.20094E-01	-.17067E-03	.50806E-06
	2	.28803E+01	.36091E-01	-.28365E-03	.79656E-06
	3	.34613E+01	.58525E-01	-.46455E-03	.13444E-05
	4	.39568E+01	.81480E-01	-.64777E-03	.19022E-05
Band i		d_0	d_1	d_2	d_3
1		.12495E+00	-.43582E-03	.14092E-04	-.69565E-07
2		.12363E+00	-.44419E-03	.14038E-04	-.68851E-07
3		.12117E+00	-.48474E-03	.12495E-04	-.62411E-07
4		.11581E+00	-.55031E-03	.98776E-05	-.50193E-07
5		-.15968E-03	.10115E-04	-.12472E-06	.48667E-09
6		.13830E+00	-.18921E-02	.12030E-04	-.31698E-07

*The units for D_0 are in μm .

Table 5b. Values of empirical coefficients in Eq. (2.15)* for parameterization of the asymmetry factor in the infrared wavelengths.

Band i	c'_0	c'_1	c'_2	c'_3
7	.79550	2.524e-3	-1.022e-5	0.0
8	.86010	1.599e-3	-6.465e-6	0.0
9	.89150	1.060e-3	-4.171e-6	0.0
10	.87650	1.198e-3	-4.485e-6	0.0
11	.88150	9.858e-4	-3.116e-6	0.0
12	.91670	5.499e-4	-1.507e-6	0.0
13	.90920	9.295e-4	-3.877e-6	0.0
14	.84540	1.429e-3	-5.859e-6	0.0
15	.76780	2.571e-3	-1.041e-5	0.0
16	.72900	2.132e-3	-5.584e-6	0.0
17	.70240	4.581e-3	-3.054e-5	6.684e-8
18	.22920	1.724e-2	-1.573e-4	4.995e-7

*The units for D_0 are in μm .

Appendix

The δ -Four-Stream Approximation for a Homogeneous Layer

In the following, we present the necessary equations for the flux calculation using the δ -four-stream approximation. The notations used in Liou et al. (1988) are followed. Let the total optical depth of a layer be τ_1 . The upward and downward fluxes at a given optical depth τ ($0 \leq \tau \leq \tau_1$) are given by

$$F^+(\tau) = 2\pi(a_1\mu_1 I_1 + a_2\mu_2 I_2), \quad (\text{A.1})$$

$$F^-(\tau) = 2\pi(a_1\mu_1 I_{-1} + a_2\mu_2 I_{-2}) + \mu_0 \pi F_0 e^{-\tau/\mu_0}, \quad (\text{A.2})$$

where the double Gauss quadratures and weights in the four-stream approximation are $\mu_1 = -\mu_{-1} = 0.2113248$, $\mu_2 = -\mu_{-2} = 0.7886752$, and $a_1 = a_{-1} = a_2 = a_{-2} = 0.5$; μ_0 is the cosine of the solar zenith angle; and πF_0 denotes the direct solar flux at the top of the atmosphere ($\pi F_0 = 0$ in the thermal infrared). The intensity solutions can be written in the form

$$\begin{bmatrix} I_2 \\ I_1 \\ I_{-1} \\ I_{-2} \end{bmatrix} = \begin{bmatrix} \phi_2^+ e_2 & \phi_1^+ e_1 & \phi_1^- e_3 & \phi_2^- e_4 \\ \Phi_2^+ e_2 & \Phi_1^+ e_1 & \Phi_1^- e_3 & \Phi_2^- e_4 \\ \Phi_2^- e_2 & \Phi_1^- e_1 & \Phi_1^+ e_3 & \Phi_2^+ e_4 \\ \phi_2^- e_2 & \phi_1^- e_1 & \phi_1^+ e_3 & \phi_2^+ e_4 \end{bmatrix} \begin{bmatrix} G_2 \\ G_1 \\ G_{-1} \\ G_{-2} \end{bmatrix} + \begin{bmatrix} z_2^+ \\ z_1^+ \\ z_1^- \\ z_2^- \end{bmatrix} e^{-f_0 \tau}, \quad (\text{A.3})$$

where $f_0(\text{solar}) = 1/\mu_0$, $f_0(\text{thermal}) = -1/\tau_1 \ln(B_1/B_0)$, B_0 and B_1 are Planck functions evaluated at the top and bottom of the layer, respectively, and the other terms except $G_{\pm 1,2}$ are defined as follows:

$$\begin{aligned} e_1 &= e^{-k_1 \tau}, \quad e_2 = e^{-k_2 \tau}, \quad e_3 = e^{-k_1(\tau_1 - \tau)}, \quad e_4 = e^{-k_2(\tau_1 - \tau)}, \\ z_{1,2}^{\pm} &= \frac{1}{2}(\eta_{1,2} \pm \eta'_{1,2}), \\ \phi_{1,2}^{\pm} &= \frac{1}{2} \left(1 \pm \frac{b_{11}^- - A_{1,2} b_{21}^-}{a^-} k_{1,2} \right), \\ \Phi_{1,2}^{\pm} &= \frac{1}{2} \left(A_{1,2} \pm \frac{A_{1,2} b_{22}^- - b_{12}^-}{a^-} k_{1,2} \right), \end{aligned}$$

where $k_{1,2}$, $A_{1,2}$, $\eta_{1,2}$, $\eta'_{1,2}$, b_{11}^- , b_{21}^- , b_{22}^- , b_{12}^- and a^- are calculated from the following equations, which are in the order of calculation. The single-

scattering albedo is denoted by $\bar{\omega}$, and $\bar{\omega}_l (l=0,1,2,3)$ is the expansion coefficient of the scattering phase function:

$$b_1(\text{solar}) = \frac{\bar{\omega}}{4\pi} \pi F_0 \sum_{l=0}^3 \bar{\omega}_l P_l(\mu_1) P_l(-\mu_0) / \mu_1$$

$$b_1(\text{thermal}) = (1 - \bar{\omega}) B_0 / \mu_1, \quad i = -2, -1, 1, 2,$$

$$c_{ij} = \frac{\bar{\omega}}{2} a_j \sum_{l=0}^3 \bar{\omega}_l P_l(\mu_1) P_l(\mu_j), \quad i, j = -2, -1, 1, 2$$

$$b_{ij} = \begin{cases} c_{ij} / \mu_1, & i \neq j \\ (c_{ij} - 1) / \mu_1, & i = j, \end{cases}$$

$$b_{22}^{\pm} = b_{22} \pm b_{2-2} \quad b_{21}^{\pm} = b_{21} \pm b_{2-1}$$

$$b_{12}^{\pm} = b_{12} \pm b_{1-2} \quad b_{11}^{\pm} = b_{11} \pm b_{1-1}$$

$$b_2^{\pm} = b_2 \pm b_{-2} \quad b_1^{\pm} = b_1 \pm b_{-1},$$

$$a_{22} = b_{22}^{\dagger} b_{22}^{\bar{}} + b_{12}^{\dagger} b_{21}^{\bar{}} \quad a_{21} = b_{22}^{\bar{}} b_{21}^{\dagger} + b_{21}^{\bar{}} b_{11}^{\dagger}$$

$$a_{12} = b_{12}^{\bar{}} b_{22}^{\dagger} + b_{11}^{\bar{}} b_{12}^{\dagger} \quad a_{11} = b_{12}^{\bar{}} b_{21}^{\dagger} + b_{11}^{\bar{}} b_{11}^{\dagger}$$

$$d_2 = b_{22}^{\bar{}} b_2^{\dagger} + b_{21}^{\bar{}} b_1^{\dagger} + b_2^{\bar{}} f_0$$

$$d_1 = b_{12}^{\bar{}} b_2^{\dagger} + b_{11}^{\bar{}} b_1^{\dagger} + b_1^{\bar{}} f_0,$$

$$a'_{22} = b_{22}^{\dagger} b_{22}^{\bar{}} + b_{12}^{\dagger} b_{21}^{\bar{}} \quad a'_{21} = b_{22}^{\dagger} b_{21}^{\bar{}} + b_{21}^{\dagger} b_{11}^{\bar{}}$$

$$a'_{12} = b_{12}^{\dagger} b_{22}^{\bar{}} + b_{11}^{\dagger} b_{12}^{\bar{}} \quad a'_{11} = b_{12}^{\dagger} b_{21}^{\bar{}} + b_{11}^{\dagger} b_{11}^{\bar{}}$$

$$d'_2 = b_{22}^{\dagger} b_2^{\bar{}} + b_{21}^{\dagger} b_1^{\bar{}} + b_2^{\dagger} f_0$$

$$d'_1 = b_{12}^{\dagger} b_2^{\bar{}} + b_{11}^{\dagger} b_1^{\bar{}} + b_1^{\dagger} f_0,$$

$$b = a_{22} + a_{11} \quad c = a_{21} a_{12} - a_{11} a_{22} \quad a^- = b_{22}^{\bar{}} b_{11}^{\bar{}} - b_{12}^{\bar{}} b_{21}^{\bar{}},$$

$$k_1 = [(b + \sqrt{b^2 + 4c}) / 2]^{1/2} \quad k_2 = [(b - \sqrt{b^2 + 4c}) / 2]^{1/2},$$

$$A_{1,2} = (k_{1,2}^2 - a_{22}) / a_{21},$$

$$\begin{aligned} \eta_1 &= (d_1 f_0^2 + a_{12} d_2 - a_{22} d_1) / f' & \eta_2 &= (d_2 f_0^2 + a_{21} d_1 - a_{11} d_2) / f' \\ \eta'_1 &= (d'_1 f_0^2 + a'_{12} d'_2 - a'_{22} d'_1) / f' & \eta'_2 &= (d'_2 f_0^2 + a'_{21} d'_1 - a'_{11} d'_2) / f' \\ f' &= f_0^4 - b f_0^2 - c. \end{aligned}$$

The coefficients $G_i (i = \pm 1, 2)$ are to be determined from radiation boundary conditions. Consider a homogeneous cloud layer characterized by an optical depth τ_1 , and assume that there is no diffuse radiation from the top and bottom of this layer, then the boundary conditions are

$$\left. \begin{aligned} I_{-1,-2}(\tau = 0) &= 0 \\ I_{1,2}(\tau = \tau_1) &= 0 \end{aligned} \right\} \quad (\text{A.4})$$

The boundary conditions can be modified to include the nonzero diffuse radiation. G_i can be obtained by an inversion of a four-by-four matrix in Eq. (A.3). We note that the only difference in the four-stream formulation between infrared and solar wavelengths is the definition of f_0 and $b_i (i = \pm 1, 2)$.

It is possible to incorporate a δ -function adjustment to account for the forward diffraction peak in the context of the four-stream approximation. We may use the similarity principle for radiative transfer to adjust the optical depth, single-scattering albedo and expansion coefficients of the phase function in the forms (Liou et al., 1988)

$$\begin{aligned} \tau' &= \tau(1 - f\bar{\omega}) \\ \bar{\omega}' &= (1 - f)\bar{\omega} / (1 - f\bar{\omega}) \\ \bar{\omega}'_l &= [\bar{\omega}_l - f(2l + 1)] / (1 - f), \quad l = 1, 2, 3, \end{aligned} \quad (\text{A.5})$$

where the fraction of scattered energy residing in the forward peak, $f = \bar{\omega}_4 / 9$.

Figure Captions

- Fig. 1 (a) Extinction coefficient/IWC, (b) single-scattering albedo and (c) asymmetry factor as functions of the mean effective size for the spectral interval 1.9-2.5 μm . The "0" points represent exact results from the light-scattering program, and the curves are from the parameterizations.
- Fig. 2 Same as Fig. 1, except for the spectral interval 800-980 cm^{-1} .
- Fig. 3 (a) Solar reflectance and (b) solar transmittance calculated by the adding method using "exact" phase function for Ci (Nov. 1). The corresponding percentage errors in solar reflectance and transmittance produced by the δ -four-stream scheme with parameterizations of the single-scattering properties are displayed in (c) and (d).
- Fig. 4 Comparisons between the present model and line-by-line calculations for (a) infrared cooling rates due to H_2O (with continuum) + CO_2 + O_3 + CH_4 + N_2O in the spectral region 10-2200 cm^{-1} , and (b) solar heating rates due to H_2O in the spectral region 2500-14500 cm^{-1} , in the midlatitude summer atmosphere.
- Fig. 5 (a) Effective upward emissivity, (b) effective downward emissivity, and (c) solar albedo as functions of the ice water path (IWP). Model results representing the mean effective sizes of 25, 50, 75, 100 and 125 μm are compared with the observed values obtained from the cirrus FIRE IFO.
- Fig. 5(d) Solar albedo as a function of effective downward emissivity. Model results for the mean effective sizes of 25, 50, 75, 100, and 125 μm are compared with the observed values obtained from the cirrus FIRE IFO.

- Fig. 6 The emissivity of cloud particles alone as a function of the ice water path (IWP). Model results for the mean effective sizes of 25, 50, 75, 100 and 125 μm are compared with the observed values obtained from the cirrus FIRE IFO.
- Fig. 7 The emissivity of cirrus clouds as a function of the visible optical depth. The "x" points are obtained from the present model for the 11 cloud types (Table 1) with thicknesses of 0.5, 1, 2 and 4 km. The solid line is from least-square fits.
- Fig. 8 Heating rates in a cirrus cloud with an ice water content of 0.015 g/m^3 for five mean effective sizes of 25 (- -), 50 (- -), 75 (---), 100 (----), and 125 μm (—). (a) Infrared, (b) solar, and (c) net. For solar radiation, the solar zenith angle is 60° , the surface albedo is 0.1, and a 12 h solar day is used.
- Fig. 9 Cloud radiative forcing at the top of the atmosphere as a function of the ice water path for five mean effective sizes of 25 (- -), 50 (- -), 75 (---), 100 (----), and 125 μm (—). (a) Infrared, (b) solar, and (c) net. For solar radiation, the solar zenith angle is 60° , the surface albedo is 0.1, and a 12 h solar day is used.
- Fig. 10 Same as Fig. 9, except for the cloud radiative forcing at the surface. (a) Infrared and (b) solar.

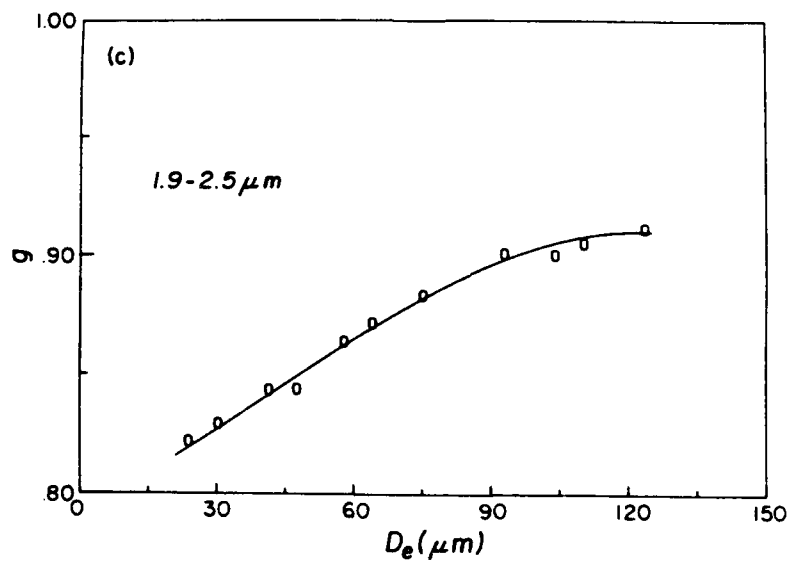
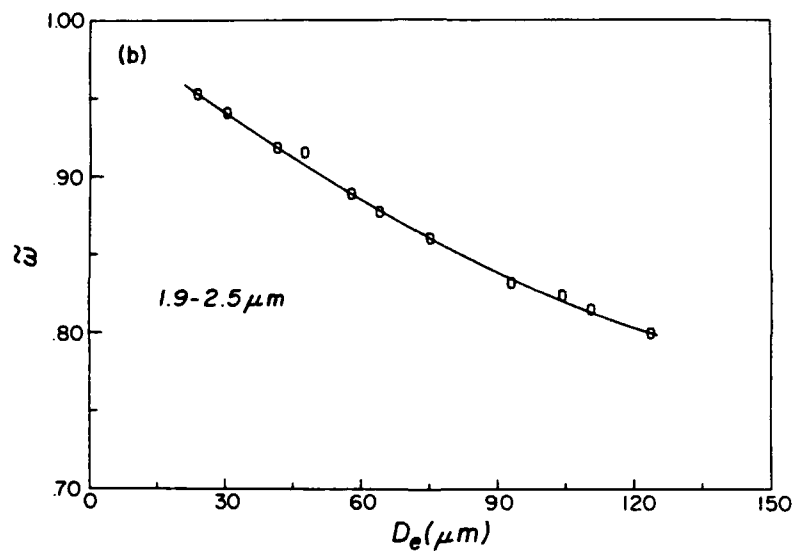
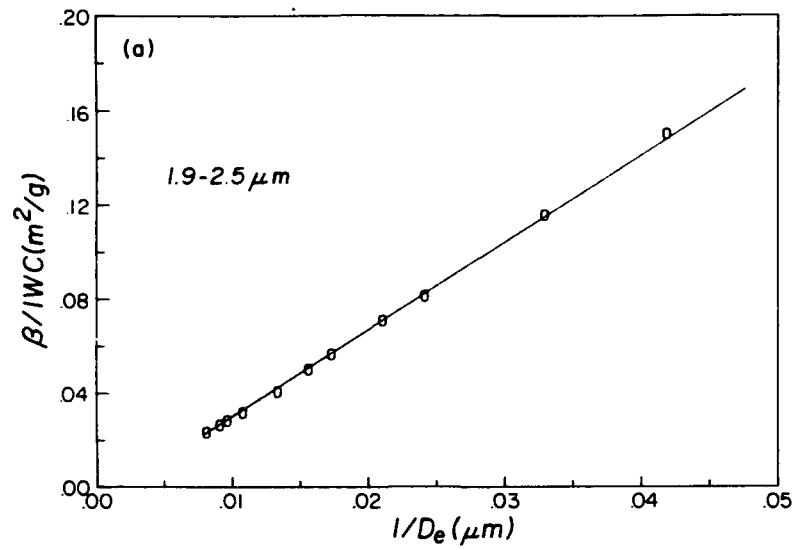


Fig. 1

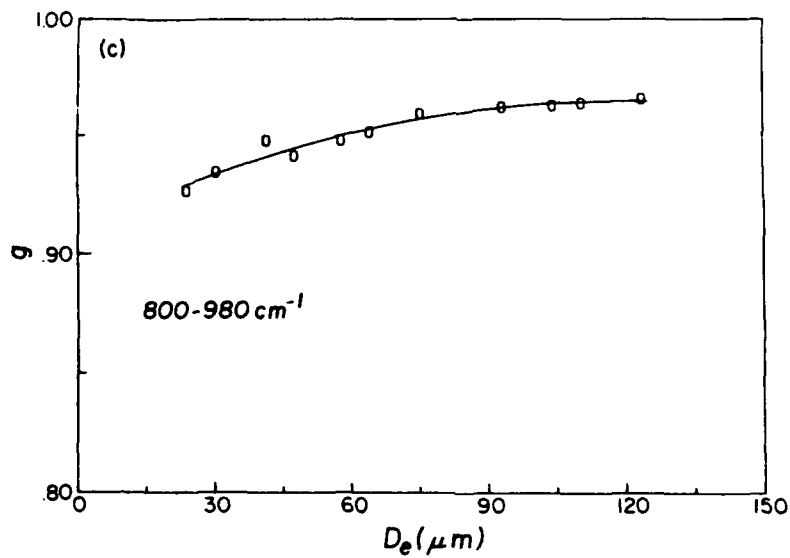
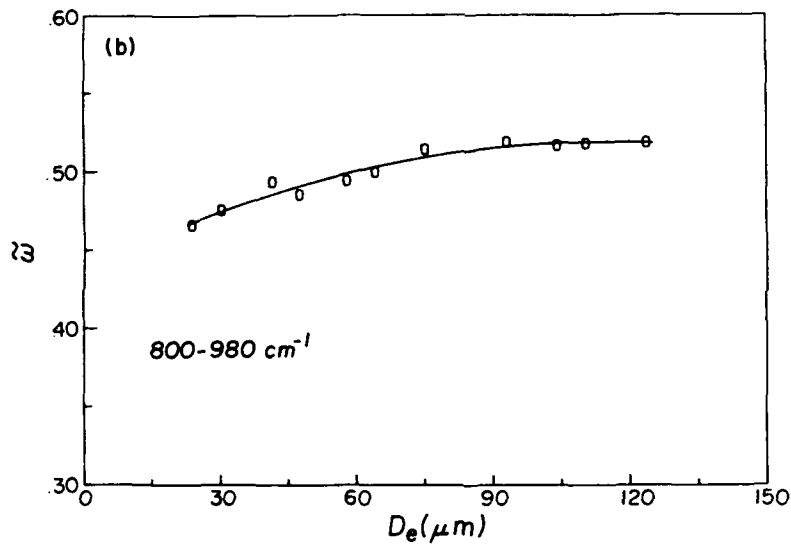
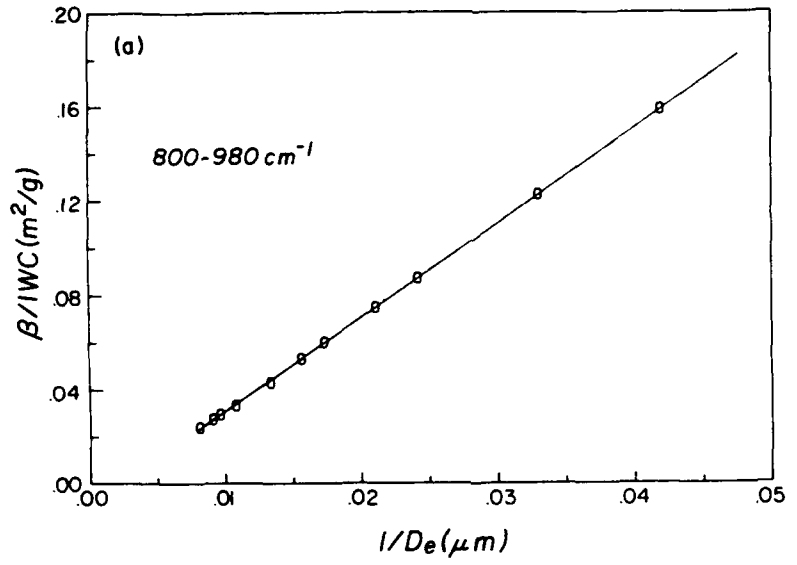


Fig. 2

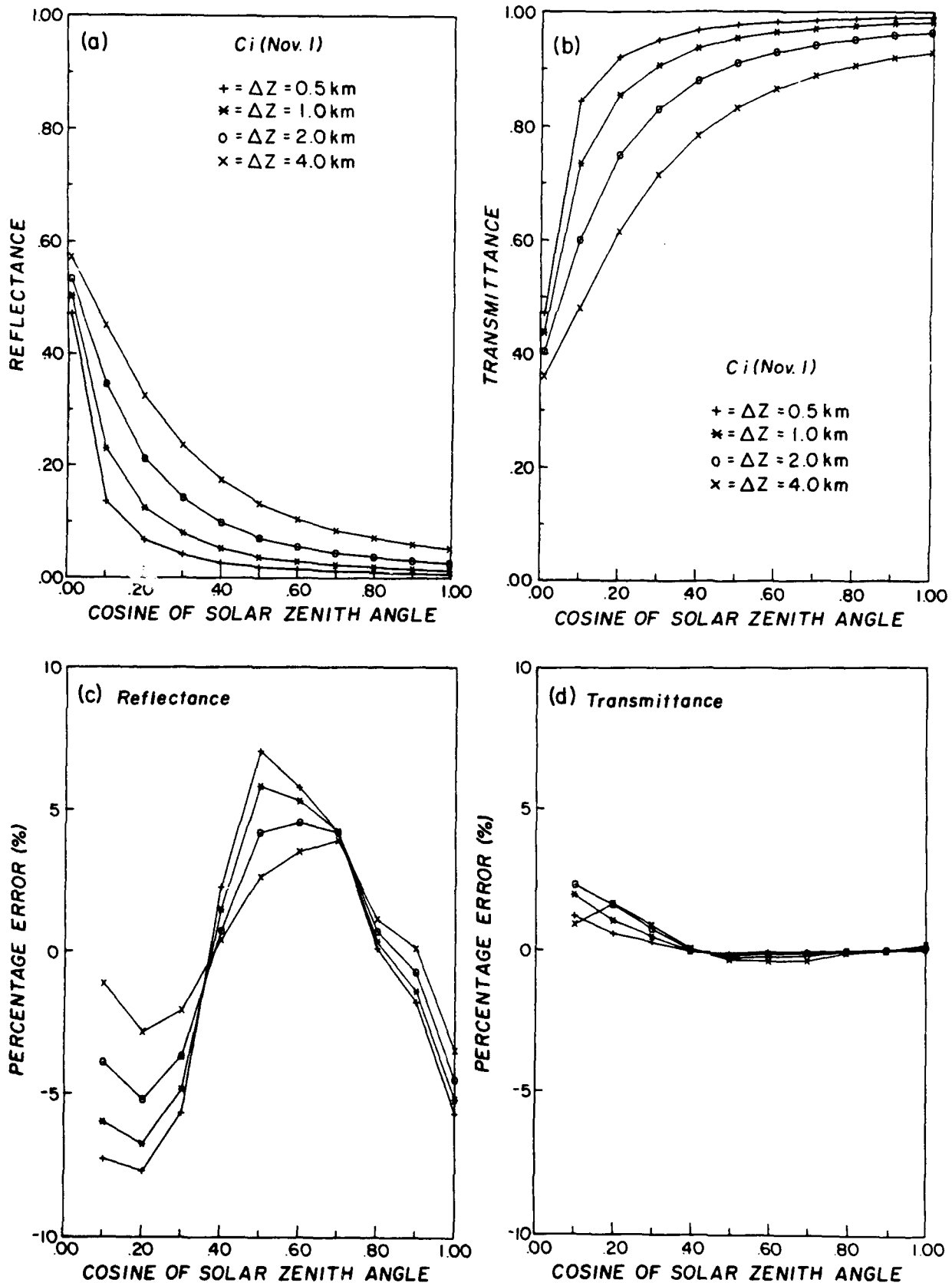


Fig. 3

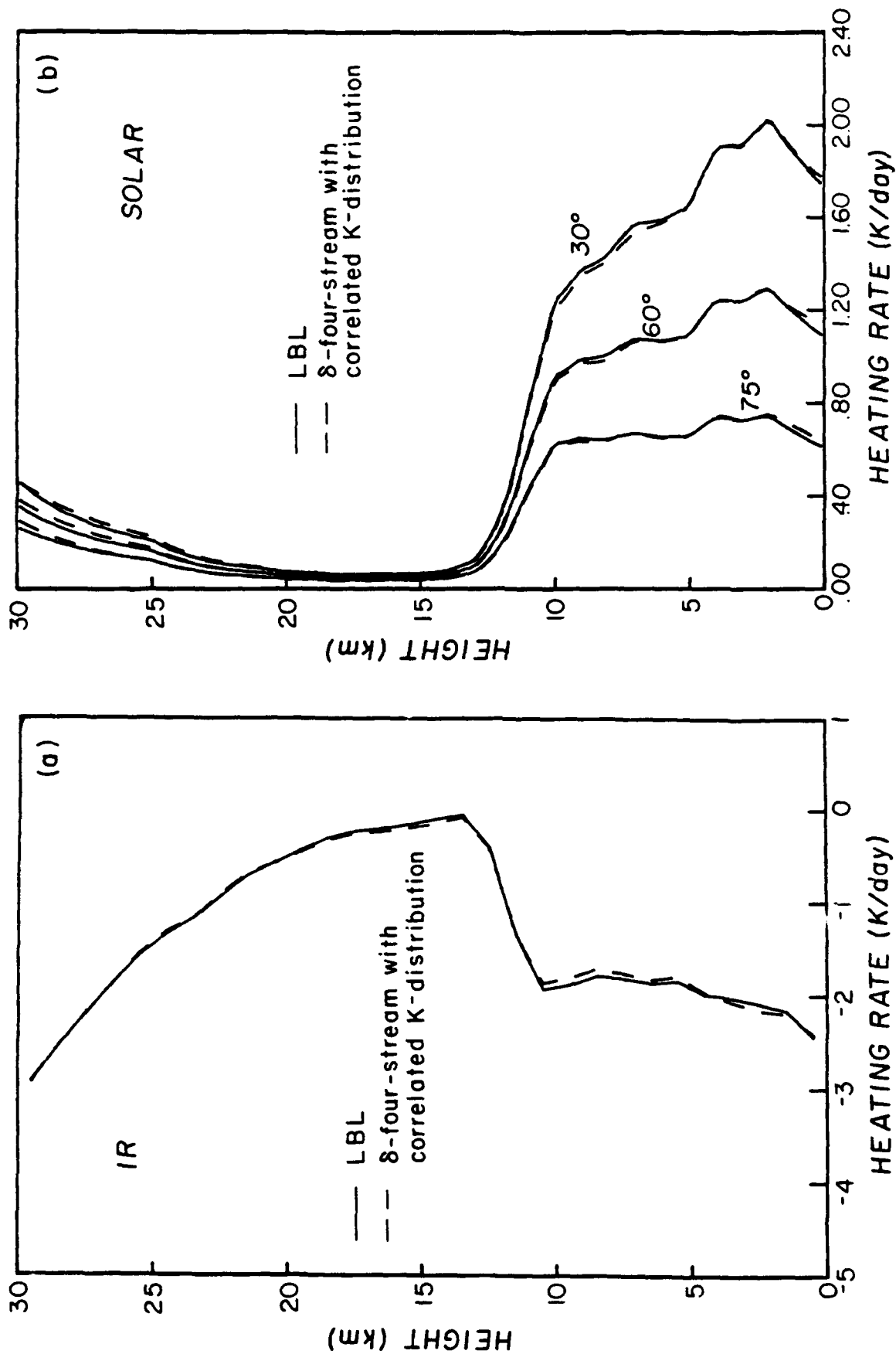


Fig. 4

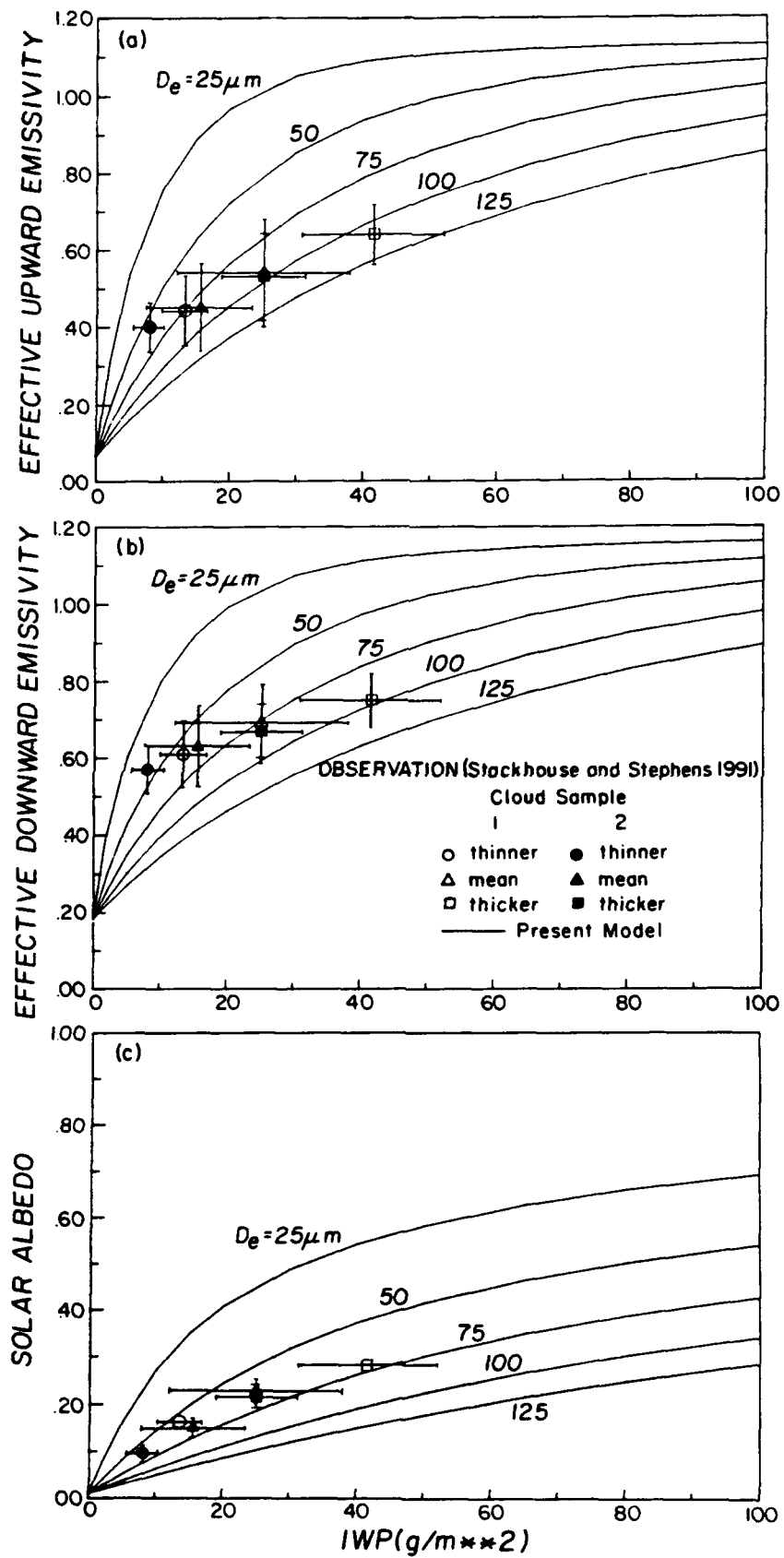


Fig. 5

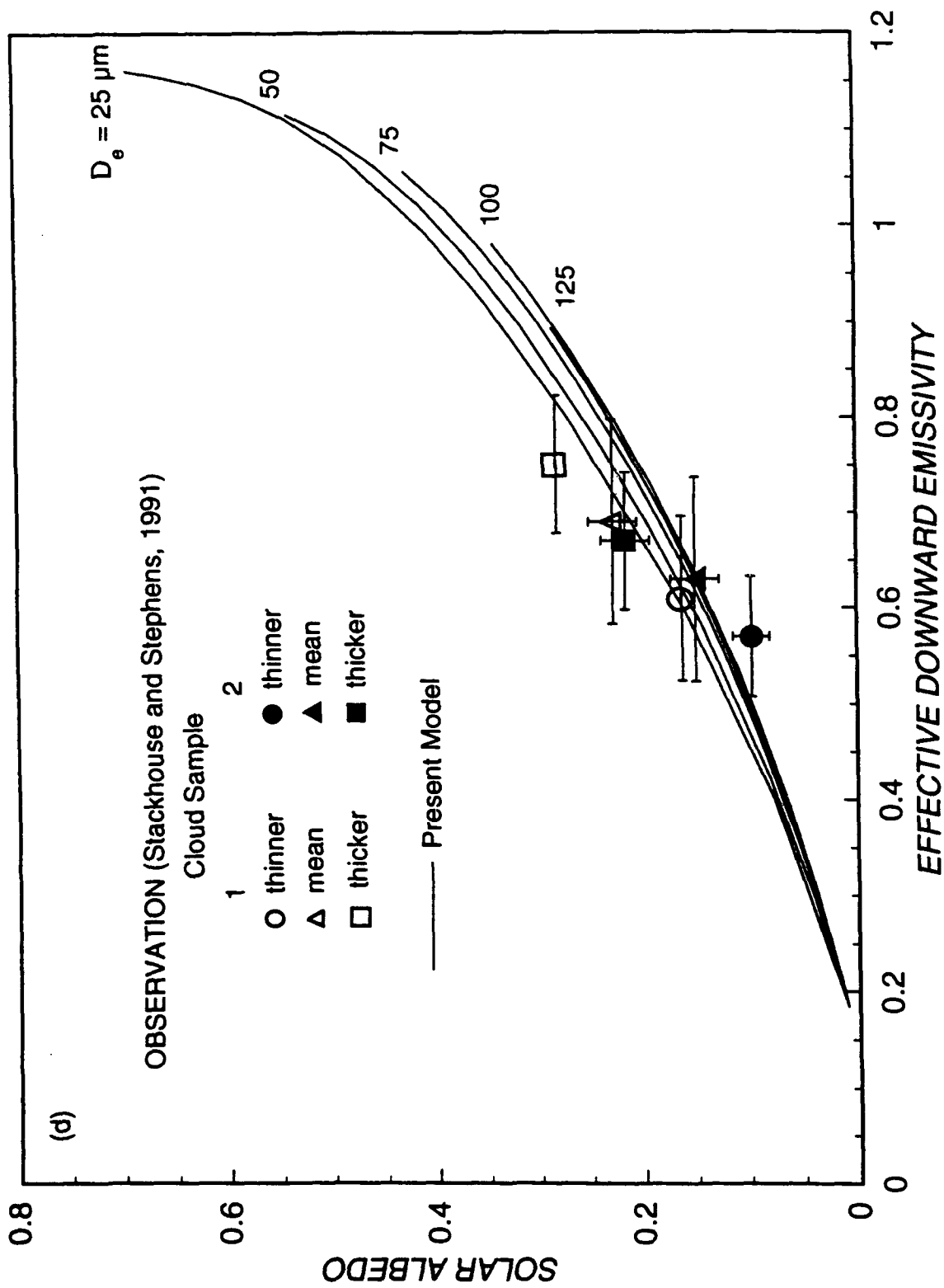


Fig. 5D

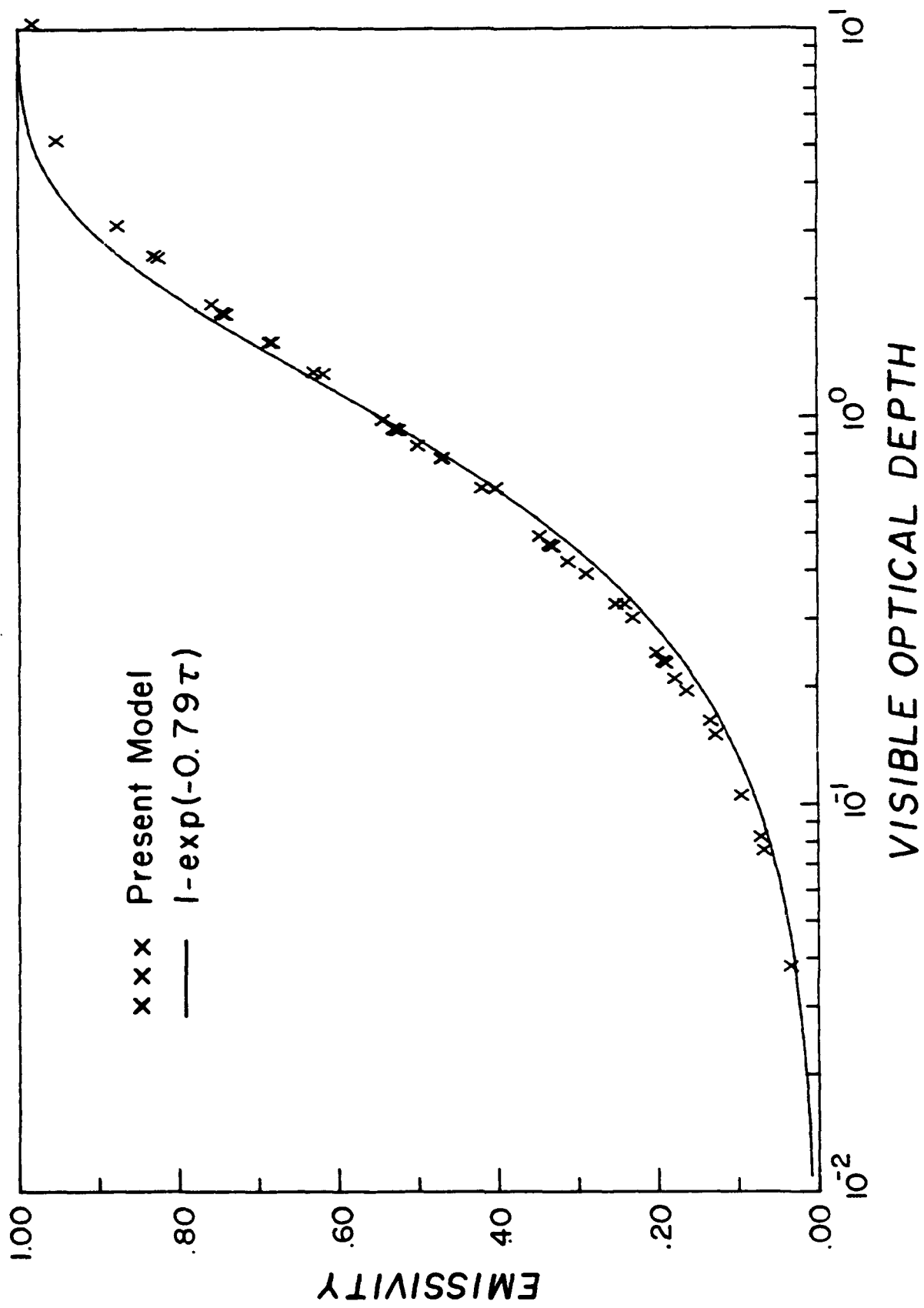


Fig. 7

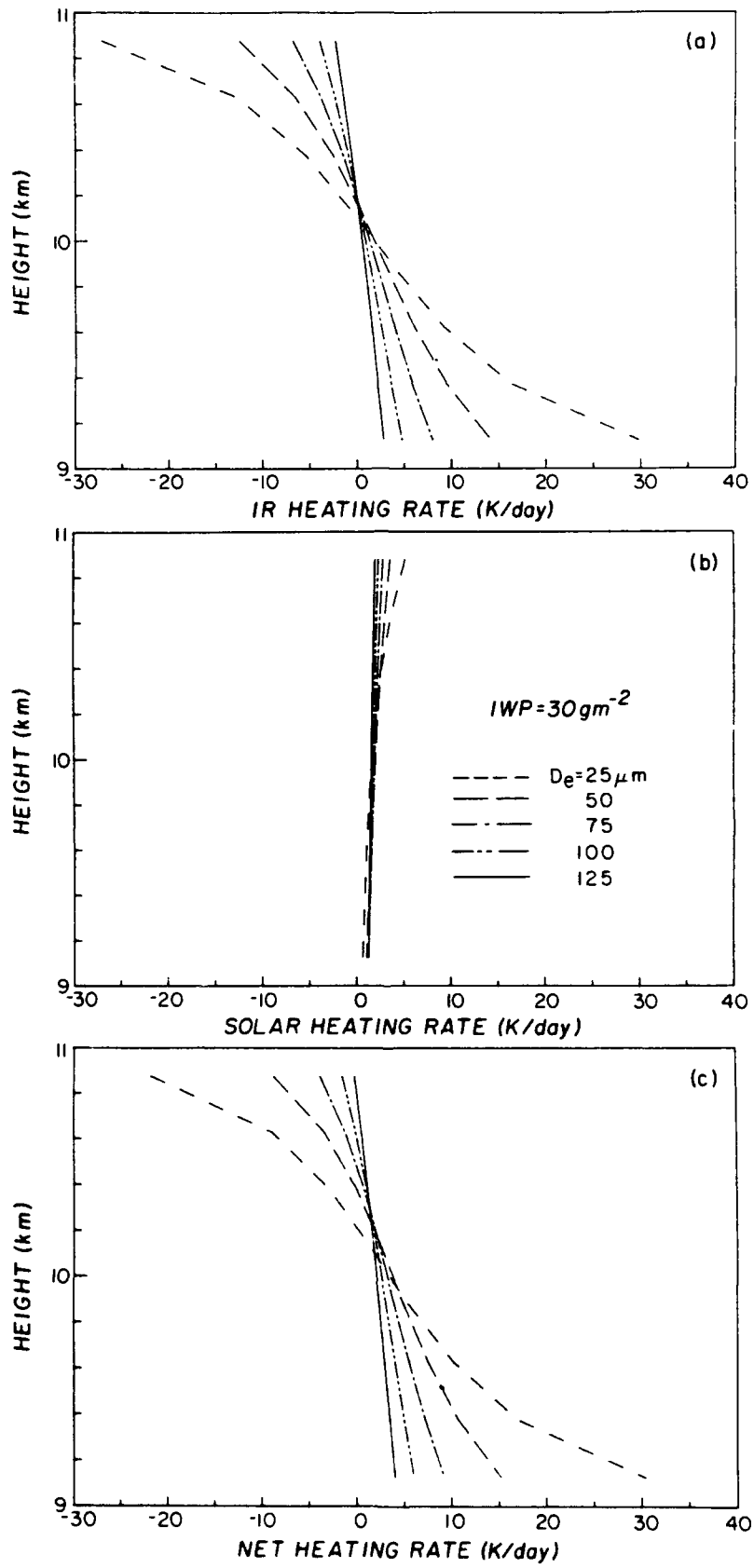


Fig. 8

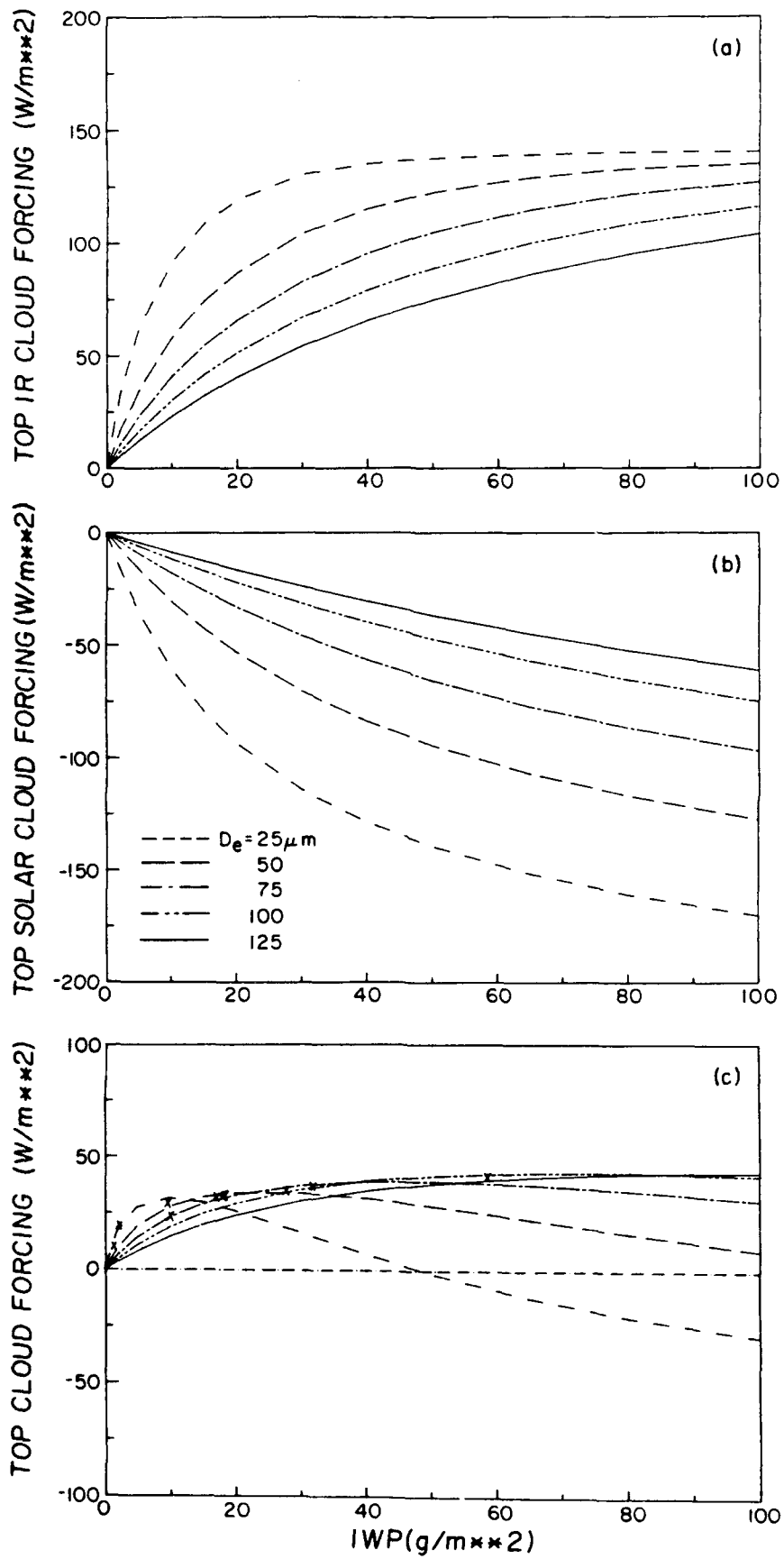


Fig. 9

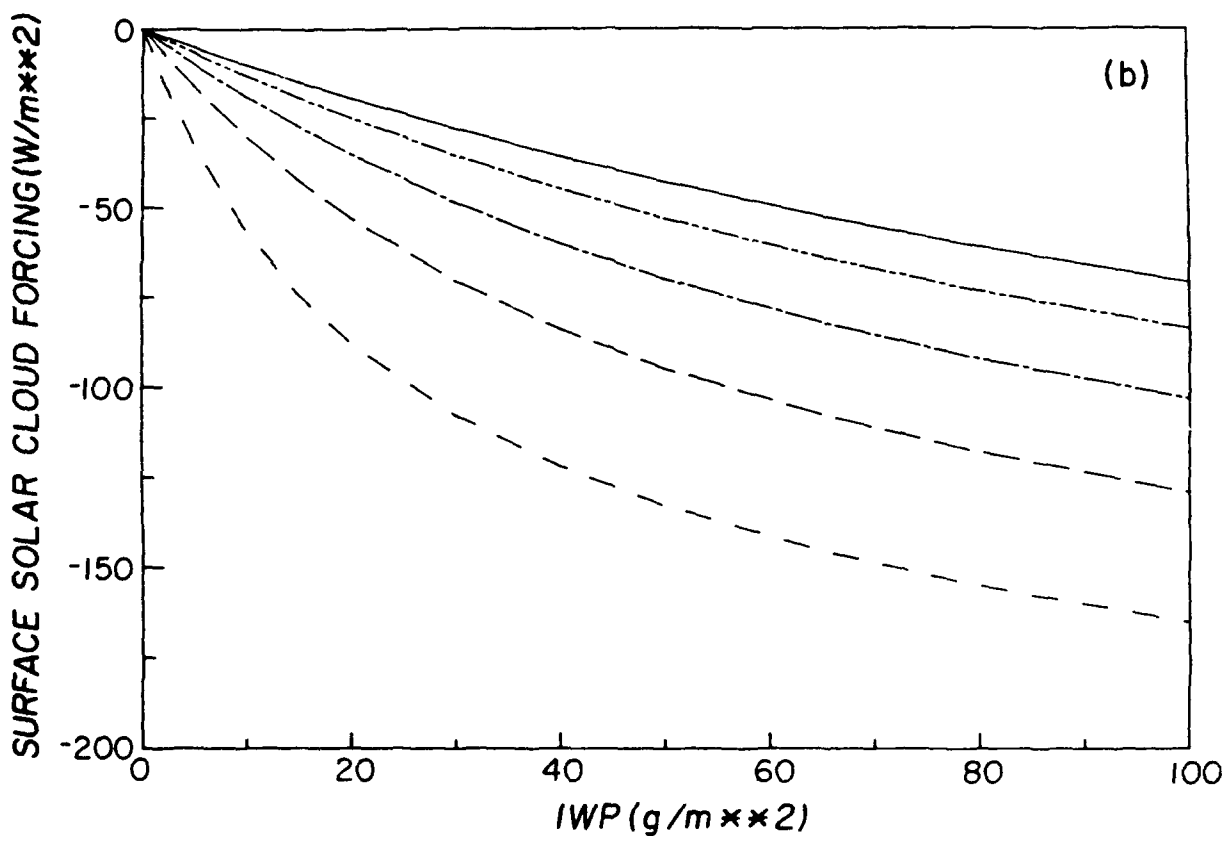
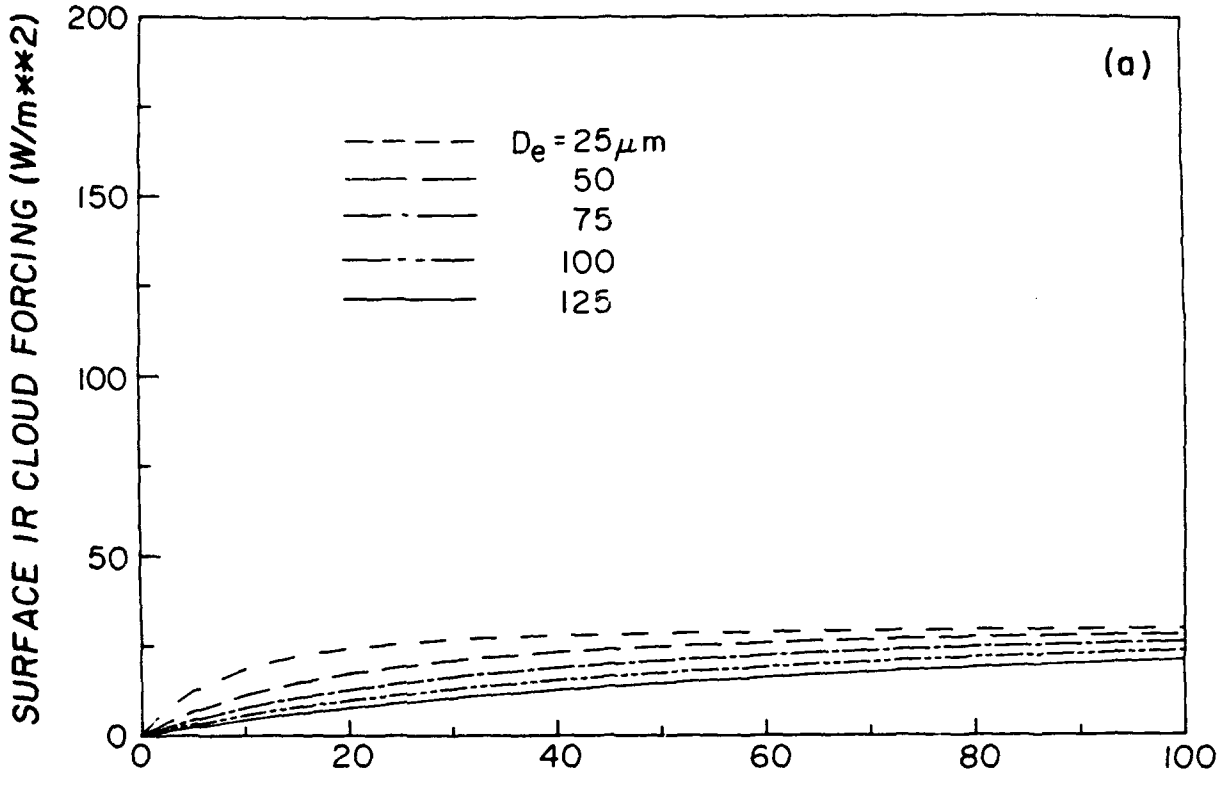


Fig. 10